Search for rare decays of the Higgs boson into a photon and a ρ, ϕ or K^{*0} meson with the CMS experiment

a PhD thesis by

Giulio Umoret

Supervisors: Roberto Covarelli, Mario Pelliccioni

May 20, 2024

CERN-THESIS-2024-263
17/05/2024

"... piccole mosse Ellie, piccole mosse."

Contact, 1997

Abstract

Higgs-boson decays into a photon and a $\rho(770)$, $\phi(1020)$, or K^{*0} (892) meson are searched for using proton-proton collision data collected by the CMS experiment at the LHC at $\sqrt{s}$ = 13 TeV. Events are selected in which the mesons decay into pairs of charged pions, pairs of charged kaons, and charged kaon-pion pairs respectively. Depending on the Higgs-boson production mode, different signal triggering and reconstruction techniques are adopted. The analysed data sets correspond to an integrated luminosity varying between 40 and 137 fb^{-1}, depending on the detailed final state. By combining these production modes, no significant excess above the background expectations is observed in any search channel. Upper limits at the 95 % confidence level on the Higgs boson branching fractions into $\rho\gamma$, $\phi\gamma$, and $K^{*0}\gamma$ are determined to be $3.74 \cdot 10^{-4}$, $2.97 \cdot 10^{-4}$, and $1.71 \cdot 10^{-4}$, respectively. These results constitute the most stringent experimental limits to date on the aforementioned decay channels.

Ringraziamenti

I dottorandi. I mozzi degli atenei.
"Ah ma tanto era solo un dottorando!" è infatti una papabile reazione a un'eventuale notizia di un PhD student investito mentre era diretto in ufficio in bicicletta. Si scherza ovviamente, ma vero è che il percorso da dottorando è un percorso ostico, in quel limbo tra lavoratore e studente in cui si soffre degli svantaggi di entrambi e ci si sente un po' come l'ultima ruota del carro accademico. Alla fine, però, è un percorso di crescita. Si impara a lottare. Si impara ad approfondire, a rispondere a tono, e a scrollarsi di dosso qualche ansia del passato. E in merito a ciò, sono quasi riuscito a sconfiggere quella sindrome dell'impostore tipica di noi torinesi, a tal punto che oggi posso dire di sentirmi finalmente un fisico. In un mondo che viaggia veloce ed esige risultati immediati, la ricerca ci insegna a muoverci a piccole mosse per poter andare lontano. Sono grato di questa lezione e di questi tre anni che ricorderò come uno dei periodi più belli della mia vita, e per questo vorrei ringraziare qualcuno.
Grazie infinite a Roberto e Mario per avermi mostrato il percorso.
Grazie infinite a Silvia per aver sempre lottato per me, anche nei momenti di difficoltà.
Grazie infinite a Riccardo, Bilal e Lisa per aver guidato i miei primi passi a Meyrin e P5.
Grazie infinite a Maria e Kevin, al gruppo MIT, con cui ho condiviso gioie e dolori della fase di revisione dell'analisi.
Grazie infinite a Ettore e Alberto con cui ho condiviso i patemi da dottorando, così come a tutto il gruppo di dottorandi di Torino.
Grazie infinite a nonno Franco, per avermi trasmesso la curiosità.
Grazie infinite ai miei per aver sempre, e dico sempre, creduto in me. Quel pizzico di logica e fantasia lo devo a loro. Grazie.
E grazie infinite a Ivana per il suo esempio di determinazione e combattività, per avermi donato il suo amore e un suo surrogato dal pelo arancione, che mi ricordava lei, anche quando lei non c'era.

Contents

Contents **7**

1 Introduction **11**

2 Theoretical framework **15**
2.1 The Standard Model 15
2.2 The strong interaction 16
2.3 The electroweak interaction 18
2.4 Spontaneous electroweak symmetry breaking 21
2.5 The Higgs boson at the LHC 25
2.6 Higgs couplings to light mesons 32
2.7 Modifications of Higgs couplings in BSM scenarios 36

3 The Compact Muon Solenoid Experiment **39**
3.1 The Large Hadron Collider 39
3.2 A CMS Overview 41
3.3 The coordinate system 42
3.4 The magnet 44
3.5 The silicon tracker 45
3.6 ECAL 47
3.7 HCAL 49
3.8 Muon system 50
3.9 The Trigger System 51
3.10 Particle identification and reconstruction 53
3.11 Particle-flow techniques 53
3.12 Track and vertex reconstruction 54
3.13 Electron reconstruction 55

3.14 Muon reconstruction . . . 57
3.15 Photon reconstruction . . . 57
3.16 Jet reconstruction . . . 59

4 Analysis Strategy **61**
4.1 Analysis overview . . . 62
4.2 Data sample . . . 63
4.3 Monte Carlo simulation . . . 63

5 Selection Procedure **67**
5.1 Trigger selection . . . 67
5.2 Preselection . . . 69

6 Background estimation **77**
6.1 Preselection distributions . . . 78

7 Multivariate analysis **83**
7.1 Gluon fusion MVA . . . 84
7.2 VBF MVA . . . 88

8 Data/MC corrections **91**
8.1 HLT efficiencies . . . 91
8.2 Isolation efficiency . . . 94
8.3 Spin-alignment reweighting . . . 97
8.4 Pile-up reweighting . . . 99

9 Invariant mass fit **103**
9.1 Maximum likelihood method . . . 104
9.2 Signal model . . . 104
9.3 Background Model . . . 105
9.4 Fit Validation . . . 110

10 Systematic Uncertainties **115**
10.1 Nuisance parameters . . . 115
10.2 Source of systematic uncertainties . . . 116
10.3 Impact of systematic uncertainties . . . 120

11 Results **125**

11.1 The unblinding procedure 125
11.2 Hypothesis testing and CL_s method 127
11.3 Upper limits 130

12 Conclusions **137**

Bibliography **141**

Introduction 1

The ATLAS and CMS experiments at the CERN Large Hadron Collider (LHC) discovered a new scalar boson in 2012, and performed numerous studies in order to assess its compatibility with the standard model (SM) Higgs boson. In the SM, the Higgs boson interacts with fermion fields via Yukawa-type couplings, which are proportional to the fermion masses. Experimentally, the top-Higgs coupling strength is indirectly confirmed by the large gluon-gluon fusion production cross section, as well as by direct measurements in the $t\bar{t}H$ production mode. Couplings to the τ lepton and b quark are well established thanks to detailed cross-section measurements in the respective Higgs-boson decay channels. Interactions with c quarks can be searched for via direct identification of c-flavoured jets or final states involving charmonium. Evidences of Higgs bosons coupling with muons have also been found.

However, no direct measurements of the Higgs interaction with u, d, and s quarks have been performed to date, since light quark couplings with the Higgs boson (H) are suppressed by the small masses and the overwhelming QCD-induced backgrounds with respect to related signals hamper direct searches. A class of decays suggested for probing these couplings is that of the Higgs boson into a light meson and a photon or Z boson: within this class, the CMS Collaboration searched for the decays $H \to Z\phi$ and $H \to Z\rho$, while the ATLAS Collaboration reported upper limits for the decays $H \to \rho\gamma, H \to \phi\gamma, H \to K^{*0}\gamma$, and $H \to \omega\gamma$. The topic of this analysis is the search for rare exclusive decays of the Higgs boson in a ρ, ϕ or K^{*0} meson and a photon and its main purpose is to measure the value of the branching ratio of the related channels.

In the $H \to \rho\gamma$ and $H \to \phi\gamma$ modes, whose branching ratio SM predictions are $\mathcal{B}(H \to \rho\gamma) = (1.68 \pm 0.08) \cdot 10^{-5}$ and $\mathcal{B}(H \to \phi\gamma) = (2.31 \pm 0.11) \cdot 10^{-6}$, respectively, the final-state meson is composed of same-flavour quarks. On the

other hand, the $K^{*0}\gamma$ mode (here and in the following collectively denoting both $H \to K^{*0}\gamma$ and $H \to \overline{K}^{*0}\gamma$ decays, which must have the same branching ratio by CPT symmetry) features a flavor-changing neutral current and is therefore very suppressed in the SM by higher electroweak orders.

The analysis is performed by combining candidate events from different production modes of the Higgs boson: gluon-gluon fusion (ggH), vector-boson-fusion (VBF), and associated production with W and Z bosons, followed by the decays $W \to \ell\nu$ and $Z \to \ell^+\ell^-$ respectively, where $\ell = e, \mu$. Proton-proton collision data used in the analysis were collected at $\sqrt{s} = 13$ TeV with the CMS detector at the LHC. Final states without a leptonic component in the decay (ggH and VBF productions) were selected online using triggers which search for isolated photons and mesons in the event, but were only activated for part of the data taking. Henceforth the related data set corresponds to an amount of integrated luminosity between 40 and 96 fb^{-1}. The selection of remaining final states is based on leptonic online selections instead, therefore it is applied to the entire 13 TeV CMS dataset, i.e. 138 fb^{-1}.

The strategy to reconstruct Higgs-boson candidates consists in identifying and characterizing a photon from clusters of energy in the electromagnetic calorimeter and identifying mesons via their decays into charged tracks $\rho \to \pi^+\pi^-$, $\phi \to K^+K^-$ and $K^{*0} \to K^\pm\pi^\mp$. After a selection procedure composed of several steps, aimed at selecting the topological properties of signal-like events and reject the background, the extraction of the number of signal events is performed with a fit to the invariant mass spectrum of the two tracks and the photon.

Chapter 2 lays the groundwork by introducing the basis of the Standard Model (SM) of particle physics, with a particular emphasis on the Brout-Englert-Higgs mechanism. It delves into the motivations behind the analysis, concentrating on the Higgs boson couplings to light quarks and the exploration of theories that extend beyond the SM.

Chapter 3 offers a detailed introduction to the LHC and the CMS detector, including an overview of the methodologies implemented by CMS for the reconstruction of physics objects.

Chapter 4 presents the overall approach of the analysis and provides a comprehensive description of the dataset and Monte Carlo (MC) simulations employed in the analysis.

Chapter 5 outlines the selection procedures tailored for each Higgs production

mode. It begins with the trigger selection and proceeds to detail the physics objects for the reconstruction of the final state candidates.

Chapter 6 illustrates the background modeling used in this analysis, showing the distributions of key variables that significantly characterize the measurement.

Chapter 7 delves into the multivariate analysis techniques employed in this research to execute a more stringent selection, enhancing the precision of the study.

Chapter 8 discusses the application of weights to the signal MC simulations to align the conditions simulated in MC with those observed during data-taking, thereby addressing any inconsistencies between data and simulations.

Chapter 9 details the construction and application of the signal and background models that are essential for performing the fit to the invariant mass spectrum.

Chapter 10 explores the systematic uncertainties, offering a thorough evaluation and quantification of their impact on the analysis.

Chapter 11 expounds on the statistical methodology utilized in the analysis, which includes signal-background fitting and the calculation of upper limits of the branching ratios of the decay channels under investigation.

Chapter 12 provides a cohesive summary of the entire analysis and compares the findings with those from recent ATLAS publications.

Theoretical framework 2

2.1 The Standard Model

The Standard Model of particle physics is the prevailing theory for describing particles and their interactions. As a Quantum Field Theory (QFT) the SM combines principles of quantum mechanics with special relativity. In the context of a QFT, particles are described as excitations of quantum fields, and their interactions are a consequence of adhering to the internal symmetries intrinsic to the system. The dynamics of these fields are expressed in terms of a specific Lagrangian density $\mathcal{L}$, which must be invariant under the local gauge transformations that correspond to each of the present symmetries. Notably, the SM encompasses the internal symmetries of the group SU(3) $\otimes$ SU(2) $\otimes$ SU(1). The strong force, described by Quantum Chromodynamics (QCD), is associated with the SU(3) gauge group. This group defines the interactions among quarks and gluons, which are the fundamental constituents of hadrons, such as protons and neutrons. On the other hand, the electromagnetic and weak interactions are unified under the Electroweak (EWK) force, described by the gauge group SU(2) $\otimes$ SU(1). By integrating these symmetry groups along with their associated gauge theories, the SM successfully encapsulates thee of the four fundamental forces and their interactions within the field of particle physics. In general, a particle in the SM may interact with other particles through one or more of these forces, but it is not compelled to interact through all of them. The types of interactions a particle can engage in are determined by the specific forces it is susceptible to. This criterion forms the basis for classifying particles within the SM.

The SM encompasses all known elementary particles. Based on their intrin-

sic property of spin, these particles are categorized into two distinct groups: fermions and bosons. Fermions, possessing a half-integer spin, are further classified into quarks and leptons, which constitute matter. Bosons, with integer spins of 0 or 1, act as mediators of the interactions between quarks and leptons. The SM includes a total of 12 elementary fermions and their corresponding antiparticles. Of these, six are quarks and six are leptons. Fermions are organized into pairs, forming three generations with increasing particle masses, as illustrated in Fig. 2.1. Each generation of quark consists of an up-type and down-type quark, with fractional electric charge of $+\frac{2}{3}e$ and $-\frac{1}{3}e$ (where e is the elementary charge), respectively. All quarks possess a color charge and combine to form color-neutral composite hadrons, such as protons and neutrons. Each generation of fermions also consists of a massive lepton and an extremely light neutrino. Leptons carry a charge of $-1e$, while neutrinos are electrically neutral. Leptons interact via electromagnetism and the weak force, whereas neutrinos interact only via the weak force due to their lack of electric charge. Each fundamental force is mediated by gauge bosons, also known as force carriers. The electromagnetic interaction is mediated by a chargeless photon (γ), the strong force by eight varieties of massless and electrically neutral gluons (g), and the weak interaction by two charged W bosons and a neutral Z boson. The Higgs boson, a spin-0 particle, represents excitations of the Higgs field, imparting mass to the fundamental particles. In the following sections, the strong and electroweak interactions will be further explored. Their fundamental implications in particle physics will be examined, with particular emphasis on the phenomenon of spontaneous electroweak symmetry breaking, that underpins the theoretical foundation of the Higgs boson.

2.2 The strong interaction

The theory that governs strong interactions is referred to as Quantum Chromodynamics (QCD), which encompasses quarks, gluons, and their interactions. The corresponding QCD Lagrangian is constructed by requiring a certain physical symmetry. Specifically, for QCD, this symmetry is the invariance under a local SU(3) gauge transformation, which can be expressed in the form

$$\psi(x) \rightarrow e^{ig_s \frac{\lambda_a}{2} \theta_a(x)} \psi(x), \tag{2.1}$$

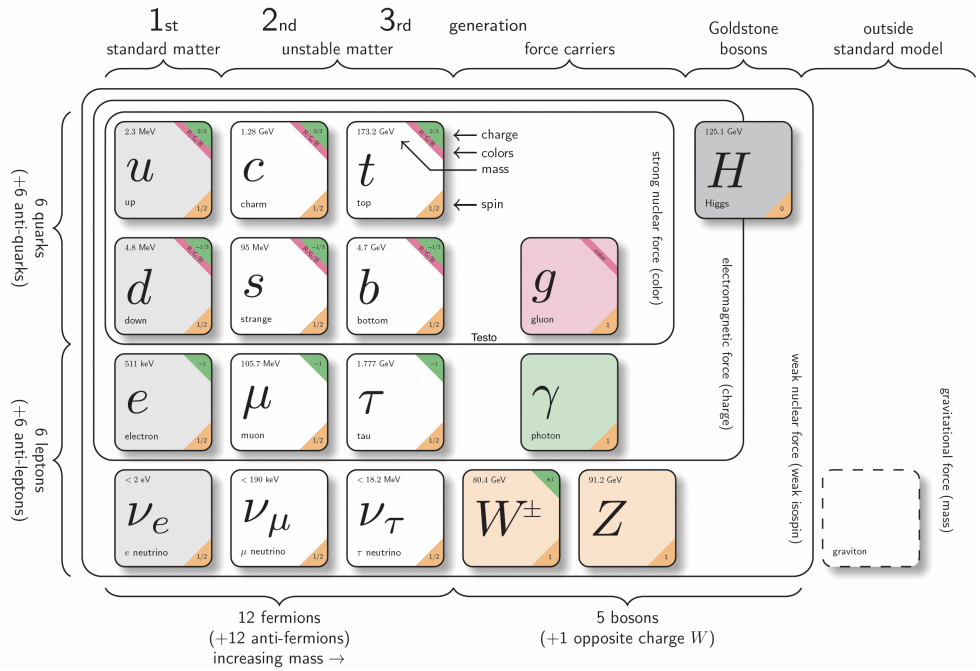

Figure 2.1: SM elementary particle scheme. The three generations of fermions are shown in the first three columns. The gauge bosons that mediate the fundamental interactions are shown in the fourth and fifth columns. The sixth column shows the recently discovered Higgs boson. The hypothetical graviton that mediates gravitational force is also shown.

where λ_a are the eight Gell-Mann matrices generating SU(3), g_s is the QCD coupling strength and $\theta_a(x)$ are eight functions of the spacetime coordinate x. The SU(3) symmetry inherent in the QCD interaction results in a conserved quantity, namely, the colour charge, relevant to quark and gluon fields. Particles (and their corresponding anti-particles) that possess this colour charge can exist in one of three states: red (anti-red), blue (anti-blue), or green (anti-green). Due to the non-commutative nature of SU(3), fields do not carry a unique charge; instead, they are categorized as either charged under $SU(3)_C$ or not. To maintain gauge invariance in this framework, it is necessary to introduce the covariant derivative

$$D_\mu = \partial_\mu - i g_s G^a_\mu(x) \frac{\lambda_a}{2}, \tag{2.2}$$

where $G^a_\mu(x)$ are the eight gauge fields corresponding to the eight massless gluons, the mediators of the strong interaction.

The QCD Lagrangian is

$$\mathcal{L}_{\text{QCD}} = \bar{\psi}(x) i\gamma^\mu \partial_\mu \psi(x) - g_s \bar{\psi}(x) \gamma^\mu \frac{\lambda_a}{2} \psi(x) G^a_\mu - \frac{1}{4} G^{\mu\nu}_a G^a_{\mu\nu}, \tag{2.3}$$

with $G^a_{\mu\nu} = \partial_\mu G^a_\nu - \partial_\nu G^a_\mu + g_s f^{abc} G^b_\mu G^c_\nu$, where f^{abc} are the completely antisimmetric structure constants, defined by the commutation relation $[\lambda^a, \lambda^b] = i f^{abc} \lambda^c$, due to the non-abelian nature of the SU(3) group. In $\mathcal{L}_{\text{QCD}}$, the final term is the free kinetic term for the eight gluon gauge fields.

It is notable that incorporating a mass term for quarks does not violate the local gauge symmetry under the $\text{SU}(3)_C$ transformation in QCD. This inclusion could, in theory, be implemented in QCD to account for the empirically observed quark masses. However, the introduction of any quark mass term would break local gauge invariance under the SU(2) transformation when integrated with the electroweak theory.

2.3 The electroweak interaction

The unification of electromagnetic and weak interactions is described by a gauge theory characterized by the invariance under transformations of the $\text{SU}(2)_L \otimes \text{U}(1)_Y$ symmetry group. In the representation of the $\text{SU}(2)_L \otimes \text{U}(1)_Y$ symmetry group, fermions are categorized as left-handed (L) doublets and right-handed (R) singlets. This arrangement leads to different coupling strengths within the Electroweak (EWK) interaction. The projection of matter fields into their respective chiral components, which is crucial for the representation, is written as follows:

$$\psi_L = \frac{1}{2}(1 - \gamma^5)\psi, \qquad \psi_R = \frac{1}{2}(1 + \gamma^5)\psi. \tag{2.4}$$

The left-handed components of the fermion fields are paired in SU(2) complex doublets while the right-handed components are represented by U(1) singlets. However, their distinction arises in their representation within the SU(2) group. In the model, neutrinos lack right-handed components. Conversely, antineutrinos, which possess quantum numbers opposite to those of neutrinos, are characterized in the SM as having solely right-handed components. The representation of fermions within these groups is reported in Tab.2.1.

Given the fields ψ_j reported in Tab. 2.1, the electroweak free massless Lagrangian can be written as

$$\mathcal{L}^0_{\text{EW}} = \sum_{j=1}^{3} i\bar{\psi}_j(x)\gamma^\mu \partial \psi_j(x) \tag{2.5}$$

Fields	ψ_1	ψ_2	ψ_3
Quarks	$\begin{pmatrix} u_L \\ d_L \end{pmatrix}$	u_R	d_R
Leptons	$\begin{pmatrix} \nu_L \\ \ell_L \end{pmatrix}$	ℓ_R	

Table 2.1: The groupings of the fermion fields in the electroweak theory.

which describes a theory of free massless fermions which do not interact. $\mathcal{L}^0_{EW}$ exhibits a clear global symmetry under rotations in either the $SU(2)_L$ or $U(1)_Y$ groups. The subscript L in $SU(2)_L$ is indicative of the fact that only the left-handed components of fermions are represented by SU(2) doublets. In a similar vein, the subscript Y in $U(1)_Y$ corresponds to a conserved quantity known as the weak hypercharge. The global rotations in these symmetry groups can be generally expressed in the form given by

$$\psi(x) \rightarrow e^{iy_1\beta}\psi(x), \qquad \psi(x) \rightarrow e^{iy_2\beta}e^{\frac{i}{2}\vec{\sigma}\cdot\vec{\alpha}}\psi(x) \tag{2.6}$$

where β, y_1, y_2 are arbitrary constants, $\vec{\sigma}$ are the Pauli matrices which generate the SU(2) group and $\vec{\alpha}$ is an arbitrary three-vector specifying the rotation. In 2.6, the first transformation represents the global symmetry under $U(1)_Y$, while the second one is representative of the global symmetry under $SU(2)_L$. A crucial component of the electroweak formalism, and fundamentally in the SM, is the extension of these global symmetries to local symmetries. This approach ensures the preservation of gauge symmetries in the generalized framework. However, $\mathcal{L}^0_{\text{EW}}$ fails to maintain local gauge invariance due to the presence of derivative terms. To maintain local gauge invariance, the introduction of the covariant derivative is necessary, particularly for the right-handed $U(1)_Y$ singlets and for the left-handed SU(2) doublets, which are respectively

$$\begin{aligned} D_\mu\psi(x) &\equiv [\partial_\mu + ig'y_2B_\mu(x)]\psi(x), \\ D_\mu\psi(x) &\equiv [\partial_\mu + ig'y_1B_\mu(x) + ig\frac{\vec{\sigma}}{2}\vec{W}_\mu]\psi(x), \end{aligned} \tag{2.7}$$

where g' is an arbitrary constant, $B_\mu(x)$ is the U(1) gauge field, and each component of $\vec{W}_\mu$ is a gauge field of SU(2). As shown in eq. 2.7, it is not possible to introduce an arbitrary constant y_k for $SU(2)_L$ transformations, similarly to

what is done in $U(1)_Y$ transformations. This restriction stems from the inherent non-commutative nature of the SU(2) group. Consequently, this implies that unlike the $U(1)_Y$ transformations where individual fermions can possess distinct charges, in $SU(2)_L$ transformations fermions are simply characterized as being either charged or not. To maintain the local $SU(2)_L \otimes U(1)_Y$ gauge symmetry, it becomes necessary to introduce four massless gauge fields. It is crucial to note that incorporating a mass term for any of these fields would violate the local gauge symmetry, necessitating that these fields remain massless. As a result, the electroweak Lagrangian, encompassing these considerations, can be expressed as

$$\mathcal{L}_{\mathrm{EW}} = -\frac{1}{4}B_{\mu\nu}B^{\mu\nu} - \frac{1}{2}\mathrm{Tr}[\tilde{W}_{\mu\nu}\tilde{W}^{\mu\nu}] + \sum_{k=1}^{3} i\bar{\psi}_k\gamma_\mu D_\mu\psi_k, \tag{2.8}$$

where $B_{\mu\nu} = \partial_\mu B_\nu - \partial_\nu B_\mu$ and $\tilde{W}_{\mu\nu} = (\vec{\sigma}/2)\vec{W}_{\mu\nu}$. The electroweak Lagrangian is characterized by an inherent global $SU(2)_L \times U(1)_Y$ symmetry. This symmetry, combined with the fact that the $SU(2)_L$ generators commute with those of $U(1)_Y$, leads to the conservation of two quantum numbers: the weak isospin T and the hypercharge Y. It is important to note, due to the non-abelian nature of $SU(2)_L$, that an arbitrary constant for each fermion field in the covariant derivative is not permissible. Consequently, all left-handed fermions are assigned a quantum number $T = \frac{1}{2}$, while right-handed fermions, being singlets in $SU(2)_L$, have $T = 0$. This scenario can be analogized to the quantum mechanics of a particle with a total spin $S = \frac{1}{2}$. Just as the spin projection operators $S_i = \frac{1}{2}\sigma_i$ are non-commutative, preventing the simultaneous measurement of all three spin components, particles are instead characterized by their total spin S and the third component S_3. Similarly, left-handed fermions are distinguished by their weak isospin third component $T_3 = \pm\frac{1}{2}$, conserved in all weak interactions. Neutrinos and up-type quarks have $T_3 = +\frac{1}{2}$, while electrons, muons, taus, and down-type quarks have $T_3 = -\frac{1}{2}$.

The electroweak theory introduces four gauge fields, corresponding to the four gauge boson mediators: the electrically neutral photon and Z boson, and the charged $W^\pm$ bosons. Among these, two gauge fields, W_μ^3 and B_μ, are electrically neutral and hence couple particles with their antiparticles. A transformation of W_μ^3 and B_μ fields is required to represent the neutral currents in terms of the

physical currents associated with the photon and Z boson:

$$\begin{pmatrix} W_\mu^3 \\ B_\mu \end{pmatrix} = \begin{pmatrix} c_W & s_W \\ -s_W & c_W \end{pmatrix} \begin{pmatrix} Z_\mu \\ A_\mu \end{pmatrix}, \tag{2.9}$$

with $s_W \equiv \sin\theta_W$ and $c_W \equiv \cos\theta_W$, where θ_W is the weak mixing angle. It is important to recognize that under the $\mathrm{SU}(2)_L \otimes \mathrm{U}(1)_Y$ symmetry, the transformation involving W_μ^3 and B_μ is originally prohibited, as these fields originate from the distinct $\mathrm{SU}(2)_L$ and $\mathrm{U}(1)_Y$ gauge symmetries. However, the experimental observation of the nonzero mass of the Z boson indicates that this symmetry is broken. Through this transformation, the field A_μ is identified as the photon field from electromagnetism, with the condition $gs_W = g'c_W = e$. The relationship between weak hypercharge (Y), electric charge (Q), and weak isospin (T_3) is defined as $Y = Q - T_3$. Given that the weak hypercharge Y can vary for each fermion, it can be assigned in a manner that satisfies this relationship for all fermions, thereby accurately reflecting their known electric charges. With these assignments, the complete set of electroweak interactions among fermions, the electroweak gauge bosons Z, $W^\pm$, and the photon can be quantitatively predicted. However, there remains the issue that introducing a mass term for either the fermions or gauge fields would break local gauge invariance, a topic that will be further explored in the next section.

2.4 Spontaneous electroweak symmetry breaking

The Brout-Englert-Higgs (BEH) mechanism, initially proposed in 1964 [1], provides a theoretical framework for the spontaneous symmetry breaking (SSB) of the electroweak interaction. This mechanism is crucial in enabling the generation of masses for both fermions and bosons. The SSB mechanism distinguishes between the electromagnetic and weak forces, laying the groundwork for their unification by Weinberg and Salam in 1967, a development that built upon Glashow's earlier contributions in 1961. In formulating the SM Lagrangian, this unification theory presumes the existence of electroweak symmetry in nature. This symmetry is spontaneously broken by introducing a doublet of complex scalar fields under $\mathrm{SU}(2)_L$, represented as

$$\phi = \frac{1}{\sqrt{2}} \begin{pmatrix} \phi^+ \\ \phi^0 \end{pmatrix} \tag{2.10}$$

The associated boson, known as the Higgs boson, stands out as the sole fundamental spin-0 particle in the SM. This particle is electrically neutral and carries a weak hypercharge of $\frac{1}{2}$. The potential associated with the Higgs field is:

$$V(\phi) = -\mu^2\phi^\dagger\phi + \lambda(\phi^\dagger\phi)^2, \tag{2.11}$$

where $\lambda > 0$ in order to avoid an unphysical behavior of the potential and $\mu^2 > 0$ to induce the spontaneous symmetry breaking. In this case, the potential assumes the shape shown in figure 2.2, known as "Mexican hat". For this specific shape, there's an infinite number of states that minimize the potential. These minimal states are defined by the condition that satisfies $\phi^\dagger\phi = \frac{\mu^2}{2\lambda} = \frac{v^2}{2}$, where the parameter v is referred to as the vacuum expectation value (vev). The local gauge symmetry of the electroweak interaction is broken by assuming a specific minimum value. The field $H(x)$ is described in terms of its excitations around

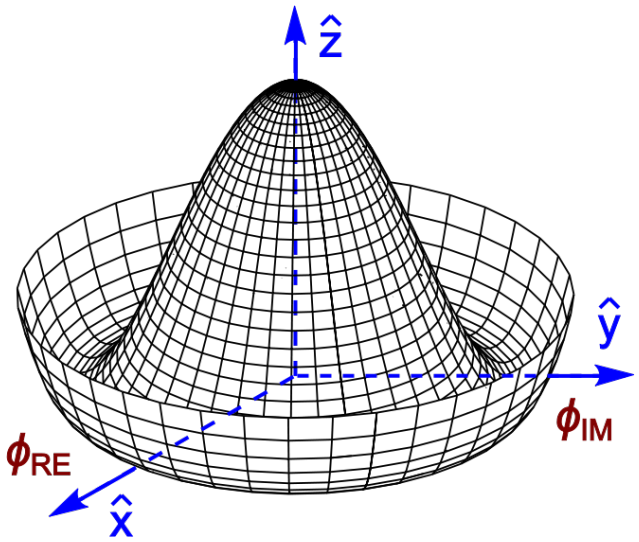

Figure 2.2: "Mexican hat" shape of the potential $V(\phi)$.

this minimum as

$$\phi = \frac{1}{\sqrt{2}}\begin{pmatrix}\phi^+\\ \phi^0\end{pmatrix} \rightarrow \frac{1}{\sqrt{2}}e^{i\frac{\sigma_i}{2}\theta_i(x)}\begin{pmatrix}0\\ v + H(x)\end{pmatrix}, \tag{2.12}$$

where the three arbitrary rotational degrees of freedom, denoted as $\theta_i(x)$, correspond to the three massless Goldstone bosons [2]. These bosons are a direct consequence of the spontaneous symmetry breaking. The $SU(2)_L$ symmetry allows for a rotation that effectively eliminates any dependence on $\theta_i(x)$. These

three degrees of freedom are absorbed by the transverse polarizations of the W and Z bosons. Consequently, the field $\phi(x)$ can be expressed as

$$\phi(x) = \frac{1}{\sqrt{2}} \begin{pmatrix} 0 \\ v + H(x) \end{pmatrix}, \tag{2.13}$$

The presence of a non-zero vev is a distinctive attribute of the Higgs field, a feature not exhibited by other fields in the SM. In its lowest energy state, the Higgs field settles into one of an infinite number of possible minima. Consequently, the resulting Lagrangian violates the requirement of gauge invariance, specifically for the $\mathrm{SU}(2)_L \otimes \mathrm{U}(1)_Y$ group. This process, known as spontaneous electroweak symmetry breaking, initiates the mechanism by which bosons associated with the broken symmetries acquire mass. Despite these changes, the vacuum state still maintains invariance with respect to U(1), ensuring the conservation of electric charge and preventing the photon from acquiring mass. Additionally, the $\mathrm{SU}(3)_C$ symmetry is unaffected, leaving the gluons massless as well.

Defining the gauge fields as

$$\begin{aligned} W_\mu^\pm &= \frac{1}{\sqrt{2}}(W_\mu^1 \mp W_\mu^2), \\ Z_\mu &= \frac{1}{\sqrt{g^2 + g'^2}}(gW_{3\mu} - g'B_\mu), \\ A_\mu &= \frac{1}{\sqrt{g^2 + g'^2}}(g'W_{3\mu} + gB_\mu), \end{aligned} \tag{2.14}$$

the BEH Lagrangian becomes

$$\begin{aligned} \mathcal{L}_{\mathrm{BEH}} =& \frac{1}{2}\partial_\mu H \partial^\mu H - \frac{1}{2}(2\lambda v^2)H^2 \\ &+ \left(\frac{g^2 v^2}{4}\right) W_\mu^- W^{\mu+} + \frac{1}{2}\left(\frac{g^2 + g'^2}{4} v^2\right) Z_\mu Z^\mu \\ &+ \left(\frac{g^2 v^2}{4}\right) \frac{2}{v} H W_\mu^- W^{\mu+} + \left(\frac{g^2 + g'^2}{4} v^2\right) \frac{1}{v} H Z_\mu Z^\mu \\ &+ \left(\frac{g^2 v^2}{4}\right) \frac{1}{v^2} H^2 W_\mu^- W^{\mu+} + \frac{1}{2}\left(\frac{g^2 + g'^2}{4} v^2\right) \frac{1}{v^2} H^2 Z_\mu Z^\mu \\ &- \lambda v H^3 - \frac{\lambda}{4} H^4 + \frac{\lambda}{4} v^4. \end{aligned} \tag{2.15}$$

The first line represent the evolution of the scalar Higgs field, which possesses a mass term given by:

$$m_H^2 = 2\lambda v^2 = -2\mu^2, \tag{2.16}$$

where m_H is the mass of the Higgs boson. This parameter is not predicted by the theory and must be measured experimentally within the SM. The mass terms for the weak gauge bosons, contained in the second line, are expressed as:

$$m_W^2 = \frac{g^2 v^2}{4}, \qquad m_Z^2 = \frac{(g^2 + g'^2)v^2}{4}. \tag{2.17}$$

The Goldstone bosons, which were absorbed via the BEH mechanism, endow the longitudinal components of the $W^{\pm}$ and Z^0 vector bosons with nonzero masses m_W and m_Z. It is noteworthy that the photon field A_μ, remaining massless, reflects the unbroken U(1) symmetry of electromagnetism. The third and fourth lines delineate the interactions of the weak bosons with the Higgs field, incorporating both triple and quartic vertices (HWW, HZZ, $HHWW$, and $HHZZ$). The last line of the equation predicts Higgs boson self couplings through cubic and quartic vertices.

Spontaneous symmetry breaking also permits fermions to gain mass through interactions with the Higgs field, known as Yukawa interactions. The mass terms for fermions introduced in the SM Lagrangian are gauge-invariant:

$$\mathcal{L}_{\text{Yukawa}} = - g_{f'} \left[\bar{\psi}'_R \phi^\dagger \begin{pmatrix} \psi_L \\ \psi'_L \end{pmatrix} + \left(\bar{\psi}_L \bar{\psi}'_L \right) \phi \psi'_R \right] \tag{2.18}$$

$$- g_f \left[\bar{\psi}_R \tilde{\phi}^\dagger \begin{pmatrix} \psi_L \\ \psi'_L \end{pmatrix} + \left(\bar{\psi}_L \bar{\psi}'_L \right) \tilde{\phi} \psi_R \right], \tag{2.19}$$

where $\tilde{\phi}$ is the charge conjugate of the ϕ field, ψ and ψ' represent the up-type and down-type fermions, and g_f and $g_{f'}$ are the coupling strengths of the interactions. Following electroweak symmetry breaking, the Yukawa Lagrangian becomes:

$$\mathcal{L}_{\text{Yukawa}} = -\frac{v}{\sqrt{2}} \left(1 + \frac{H}{v} \right) \left[g_{f'} (\bar{\psi}'_R \psi_L + \bar{\psi}'_L \psi_R) + g_f (\bar{\psi}_R \psi'_L + \bar{\psi}_L \psi'_R) \right], \tag{2.20}$$

The masses of the fermions are defined as:

$$m_{f^{(\prime)}} = \frac{g_{f^{(\prime)}} v}{\sqrt{2}}. \tag{2.21}$$

This procedure implies also that the Higgs field interacts with fermions, with couplings proportional to fermion masses.

2.5 The Higgs boson at the LHC

On July 4th 2012 the discovery of a new boson with a mass around 125 GeV was announced by the ATLAS [3] and CMS [4] Collaborations, after having analysed data collected at $\sqrt{s}$ = 7 and 8 TeV and a total integrated luminosity of about 10 fb^{-1}. The discovery was performed with studies on different decay channels. The combination of two decay modes, $H \rightarrow \gamma\gamma$ and $H \rightarrow ZZ$, despite their low branching fractions, provided an excess of events of 5 standard deviations with respect to the background. The clean signature of these two channels was the crucial feature of the measurement of the mass. In Fig. 2.3, the invariant mass spectrum of decay products is presented. The left plot depicts the invariant mass distribution of *diphoton* events, with each event weighted according to the signal-to-background ratio (S/(S+B)). The right plot shows the distribution of the four-lepton decay products from Z vector boson decays, specifically the $ZZ \rightarrow 4l$ process. The theoretical prediction was confirmed

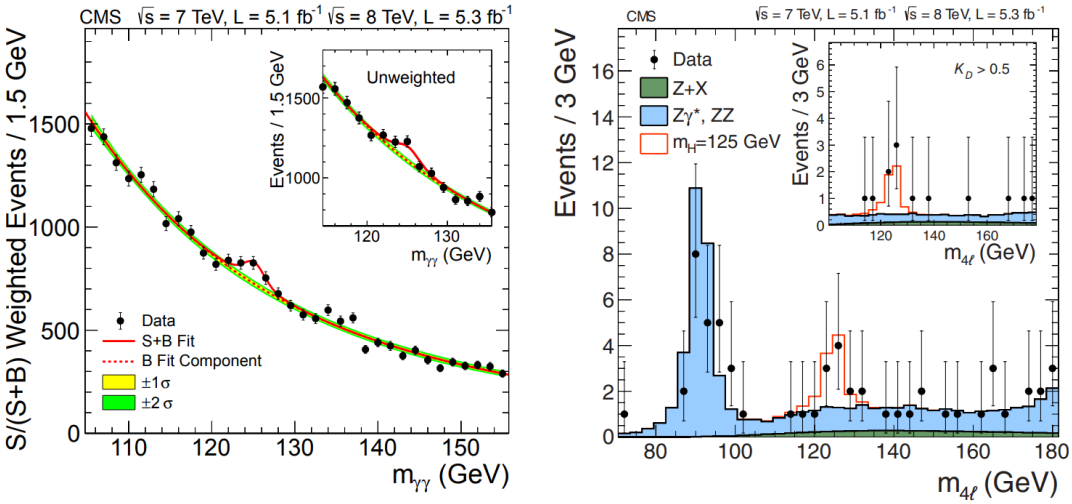

Figure 2.3: Invariant mass distributions by the CMS Collaboration, for the $\gamma\gamma$ final state (left plot) and the four-lepton final state (right plot), at the moment of the Higgs boson discovery.

with the measurement of the spin parity $J^P = 0^+$. Combining data samples by ATLAS with data collected at 4.9 fb^{-1} at 7 TeV and 20.2 fb^{-1} at 8 TeV and CMS with 5.1 fb^{-1} at 7 TeV and 19.7 fb^{-1} at 8 TeV, the Higgs boson mass was measured at $m_H = 125.09 \pm 0.21(\text{stat.}) \pm 0.11(\text{syst.})$ GeV [5]. Currently, the most precise measurement of the Higgs boson mass is $m_H = 125.38 \pm 0.11(\text{stat.}) \pm 0.08(\text{syst.})$ GeV [6].

This section presents an overview of the production mechanisms of the Higgs boson, as well as a discussion of the various decay modes, highlighting their contribution to our understanding of the particle physics as observed in LHC experiments.

2.5.1 Higgs-boson production modes

At the LHC, where protons are brought into collision at a centre-of-mass energy of 13 TeV, the Higgs boson is produced through a variety of different mechanisms, each of which has a different cross section. The Feynman diagrams of the dominating production modes for $m_H = 125$ GeV are reported in Fig. 2.4. Each production mechanism has distinct characteristics that influence the final state topology:

- **Gluon-gluon Fusion (ggH):** the Higgs boson is produced by the interaction of two gluons through a quark loop, primarily involving heavy top and bottom quarks. The final state typically contains only the decay products of the Higgs boson. As shown in Fig. 2.5, among the various Higgs boson production modes at the LHC, the gluon fusion mechanism has the largest cross section.

- **Vector Boson Fusion (VBF):** in this mode, the Higgs boson is created through the interaction of two vector bosons (Z or W), emitted by initial-state quarks. The final state is characterized by the decay products of the Higgs boson and a pair of quarks, observed as hadron jets with large invariant mass and angular separation, aiding in the identification of VBF events.

- **Associated production with a vector boson (VH):** in the VH production mode, also known as *higgsstrahlung*, the Higgs boson is emitted alongside a vector boson, Z or W. The final state includes the decay products of the vector boson, such as a pair of charged leptons, a charged lepton and a neutrino, or a pair of quarks.

- **Production in Association with a Top Quark-antiquark Pair (ttH):** the ttH production mode involves the decay of top quarks into a bottom quark and a W boson, followed by the decay of W bosons into quark pairs or a

lepton and a neutrino. The ttH events have several final state topologies, all including at least two hadron jets from bottom quarks (b-jets).

The contribution of each production mechanism, or production channel, to the total cross-section of the Higgs boson at the LHC is quantitatively significant. The ggH production channel dominates with an occurrence rate of 87%, followed by VBF contributing 7%, VH at 4%, ttH at 1%. However, the experimental sensitivity to each production mode is influenced not only by the cross section but also by the presence of competing processes, commonly referred to as background events. Some production modes are distinguished by characteristic objects in their final state, which are crucial for identifying the processes more efficiently. The strategic utilization of these distinctive features leads to a substantial reduction in background events, enhancing the sensitivity of the measurements and permitting more precise and reliable experimental observations.

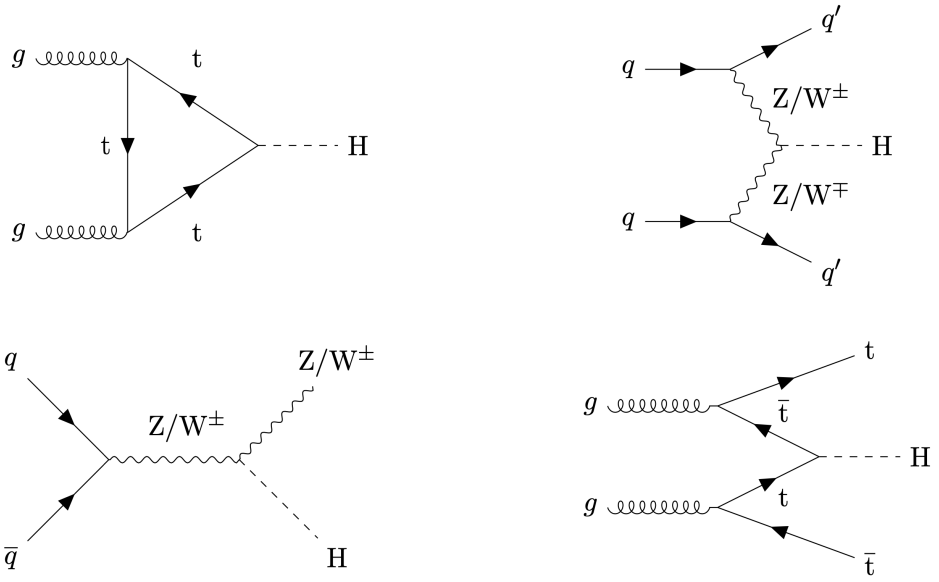

Figure 2.4: Main Higgs boson production processes at the LHC: Gluon fusion (top-left) Vector-boson fusion (top-right) Associated production of a Higgs boson and a vector boson (bottom-left) Associated production with a top-quark pair (bottom-right).

2.5.2 Higgs boson decay channels

The Higgs boson, with a lifetime of approximately 10^{-22} s, decays almost instantaneously after its production. The decay channels of the Higgs boson and their corresponding branching ratios are established by the strength of the

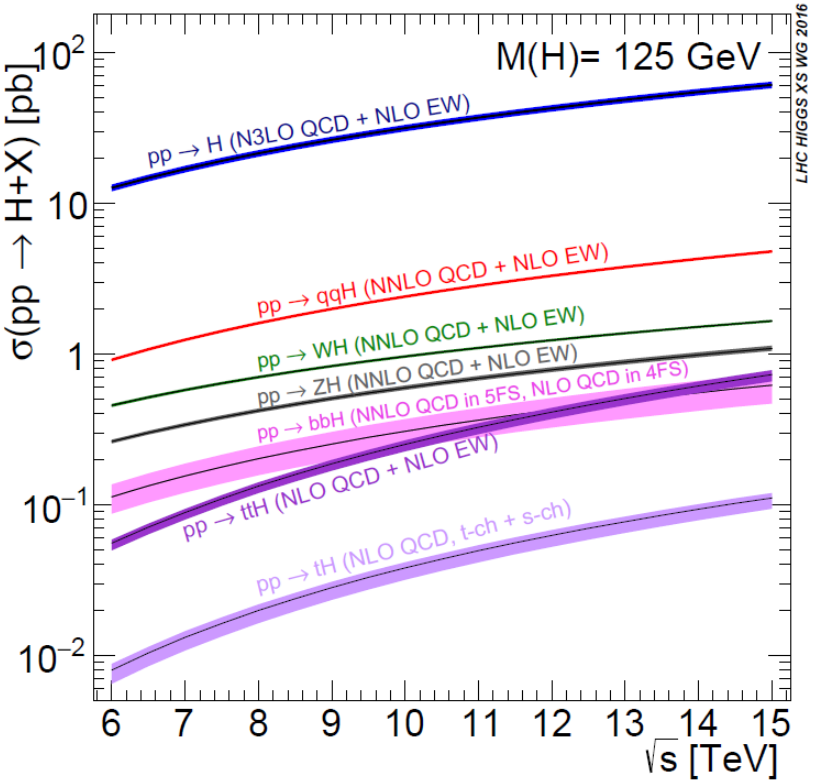

Figure 2.5: Production mechanisms cross sections and their uncertainties for a SM Higgs boson of mass $m_H = 125$ GeV, as function of $\sqrt{s}$ for p-p collisions [7].

Higgs field interaction with the particles involved in the final state. Branching ratios for the decay modes that exhibit the largest values are reported in Fig. 2.6 as a function of the Higgs mass, whereas Tab. 2.2 presents the branching ratio values for a Higgs boson with $m_H = 125$ GeV. Since its discovery, the majority

Decay channel	Branching ratio (%)
$H \to b\bar{b}$	58.24
$H \to W^+W^-$	21.37
$H \to gg$	8.187
$H \to \tau^+\tau^-$	6.272
$H \to c\bar{c}$	2.891
$H \to ZZ$	2.619
$H \to \gamma\gamma$	0.227
$H \to Z\gamma$	0.153
$H \to \mu^+\mu^-$	0.022

Table 2.2: Branching ratios of Higgs boson decay channels.

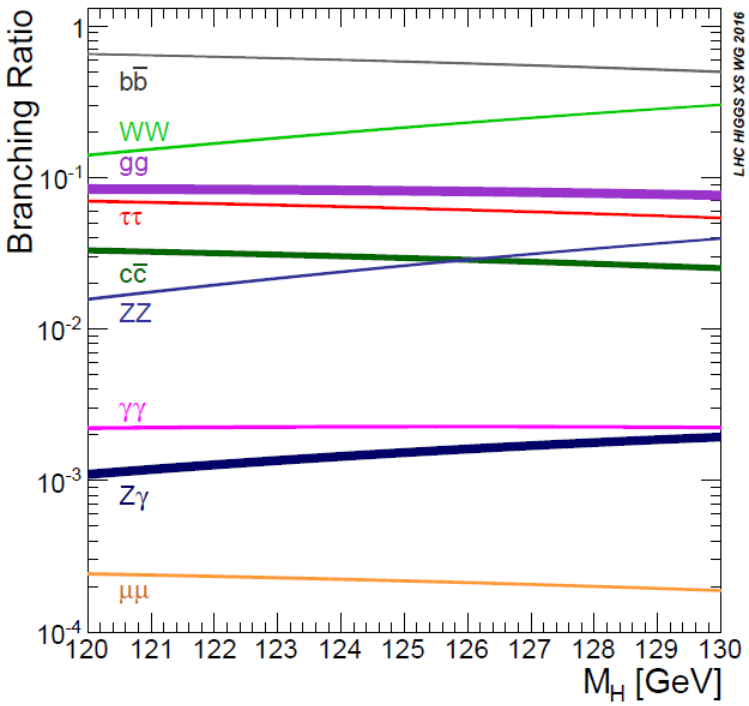

Figure 2.6: Higgs-boson branching fractions and their uncertainties as function of the Higgs mass. [7].

of the Higgs boson production modes and several decay channels predicted by the SM have been measured. Notably, the Higgs boson's decays into the $\gamma\gamma$, $ZZ \rightarrow 4l$, $WW \rightarrow l\nu_l l\nu_l$ and $Z\gamma$ bosonic channels have been observed [8, 9, 10, 11]. Couplings to fermions are generally more challenging to measure at the LHC than the bosonic ones. The presence of neutrinos in τ leptons introduces unique complexities, particularly in their hadronic decays which involve jets in the final state. For muons and electrons, their comparatively lower masses result in significantly smaller branching ratios. In the case of quarks, they hadronize into jets, making their identification challenging against the substantial QCD multijet background at the LHC. Since 2012, various analyses have led to results that include an observation in the fermionic sector of Higgs decays. The large gluon-gluon fusion production cross section production indirectly confirms the top-Higgs coupling strength. It is also directly measured in the $t\bar{t}H$ production mode [12, 13]. Couplings to the τ lepton and b quark are well established thanks to detailed cross-section measurements in the respective Higgs-boson decay channels [14, 15, 16, 17]. Interactions with c quarks can be searched for via direct identification of c-flavoured jets [18, 19]. Evidences of Higgs bosons coupling

with muons have also been found [20, 21].

In summary, CMS and ATLAS experiments has discerned several distinct categories for Higgs production and decay and combined them to measure the Higgs coupling modifiers: $\kappa_Z, \kappa_W, \kappa_\gamma, \kappa_g, \kappa_\tau, \kappa_t, \kappa_b, \kappa_\mu$, and $\kappa_{Z\gamma}$. Measurement on κ_c is still not precise enough to contribute to the global fit reported in Fig. 2.7. CMS has set a 95% confidence level that κ_c falls within the interval

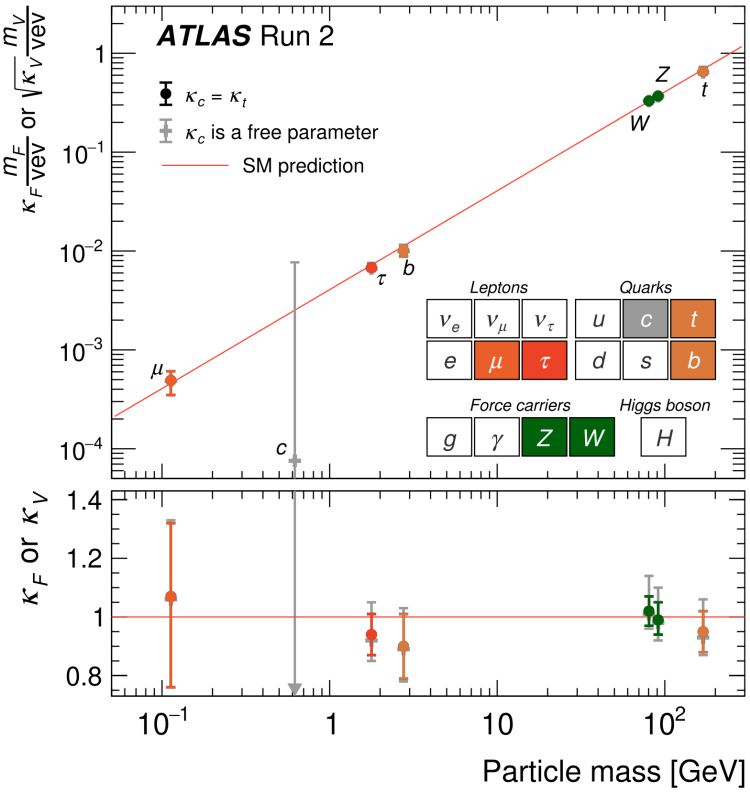

Figure 2.7: Scaling of the reduced Higgs boson coupling modifiers and their uncertainties to fermions and vector bosons as a function of their masses, as measured by the ATLAS collaboration using the full Run 2 dataset. Colored circle markers: fit scenario with $\kappa_c = \kappa_\tau$. Gray cross markers: fit scenario with κ_c floating freely. The vertical bar on each point denotes the 68% confidence interval.

$1.1 < |\kappa_c| < 5.5$ [19], while ATLAS within $|\kappa_c| < 8.5$ [18]. Experiments at the LHC are currently starting to be sensitive to second generation of fermions. While the amount of data collected so far is insufficient for definitive observations, investigations are underway to explore couplings of the Higgs boson to lighter fermions. These studies aim to probe potential physics beyond the SM that might enhance the Higgs couplings with these particles. Constraints have been established on the Higgs boson decaying into an electron-positron pair

($H \to ee$) [22, 23]. Additionally, limits on the couplings $\kappa_u, \kappa_d, \kappa_s$ have been set to $|\kappa_u| < 16000$, $|\kappa_d| < 17000$, $|\kappa_s| < 1700$ [24].

Decays of the Higgs into a light meson and a photon or a Z boson are another class of decays suggested for probing the Higgs boson couplings to u, d, s quarks. The CMS Collaboration explored the decays $H \to Z\phi$ and $H \to Z\rho$ [25], while the ATLAS Collaboration has reported upper limits for the decays $H \to \rho\gamma$, $H \to \phi\gamma$ [26], as well as for $H \to K^*\gamma$, and $H \to \omega\gamma$ [27]. The focus of this analysis is on the search for rare, exclusive decays of the Higgs boson into a $\rho\gamma$, $\phi\gamma$, or $K^{*0}\gamma$ meson and a photon, determining the branching ratio values for these specific channels.

A list of Higgs boson rare few-body decays including the most recent limit on branching ratios is reported in Tab. 2.3. This table includes decays into a gauge boson plus a single hadronic bound system in the form of a quarkonium state and exclusive decays into two quarkonium bound states.

Decay Channel	Branching fraction	Limits
$H \to Z\rho^0$	$(7.19 \pm 0.29) \times 10^{-6}$	$< 1.2 \times 10^{-2}$ [25]
$H \to Z\phi$	$(2.42 \pm 0.10) \times 10^{-6}$	$< 3.6 \times 10^{-3}$ [25]
$H \to ZJ/\psi$	$(2.3 \pm 0.1) \times 10^{-6}$	$< 1.9 \times 10^{-3}$ [28]
$H \to Z\psi(2S)$	1.7×10^{-6}	$< 6.6 \times 10^{-3}$ [28]
$H \to \gamma\rho^0$	$(1.68 \pm 0.08) \times 10^{-5}$	$< 10 \times 10^{-4}$ [26]
$H \to \gamma\omega$	$(1.48 \pm 0.08) \times 10^{-6}$	$< 1.5 \times 10^{-4}$ [27]
$H \to \gamma\phi$	$(2.31 \pm 0.11) \times 10^{-6}$	$< 4.8 \times 10^{-4}$ [26]
$H \to \gamma J/\psi$	$(3.01 \pm 0.15) \times 10^{-6}$	$< 2.6 \times 10^{-4}$ [29]
$H \to \gamma\psi(2S)$	$(1.3 \pm 0.0) \times 10^{-6}$	$< 9.9 \times 10^{-5}$ [29]
$H \to \gamma\Upsilon(1S)$	$(5.22^{+2.02}_{-1.70}) \times 10^{-9}$	$< 4.9 \times 10^{-5}$ [30]
$H \to \gamma\Upsilon(2S)$	$(1.42^{+0.72}_{-0.57}) \times 10^{-9}$	$< 5.9 \times 10^{-5}$ [30]
$H \to \gamma\Upsilon(3S)$	$(9.1^{+4.8}_{-3.8}) \times 10^{-10}$	$< 5.7 \times 10^{-5}$ [30]
$H \to \phi J/\psi$	$(5.8 - 6.0) \times 10^{-9}$	$< 3.8 \times 10^{-4}$ [28]
$H \to J/\psi J/\psi$	$(5.9 \pm 2.3) \times 10^{-10}$	$< 3.8 \times 10^{-4}$ [28]
$H \to \Upsilon(1S)\Upsilon(1S)$	2.3×10^{-9}	$< 1.7 \times 10^{-3}$ [28]

Table 2.3: Predicted branching fractions for Higgs decays into a boson and various mesons or a pair of mesons, with corresponding upper limits.

2.6 Higgs couplings to light mesons

The purpose of this PhD thesis is the study of the rare exclusive decay $H \to \rho/\phi/K^{*0}\gamma$ as a way for probing the Higgs boson coupling with first- and second-generation quarks. This section delves into the details about the theoretical

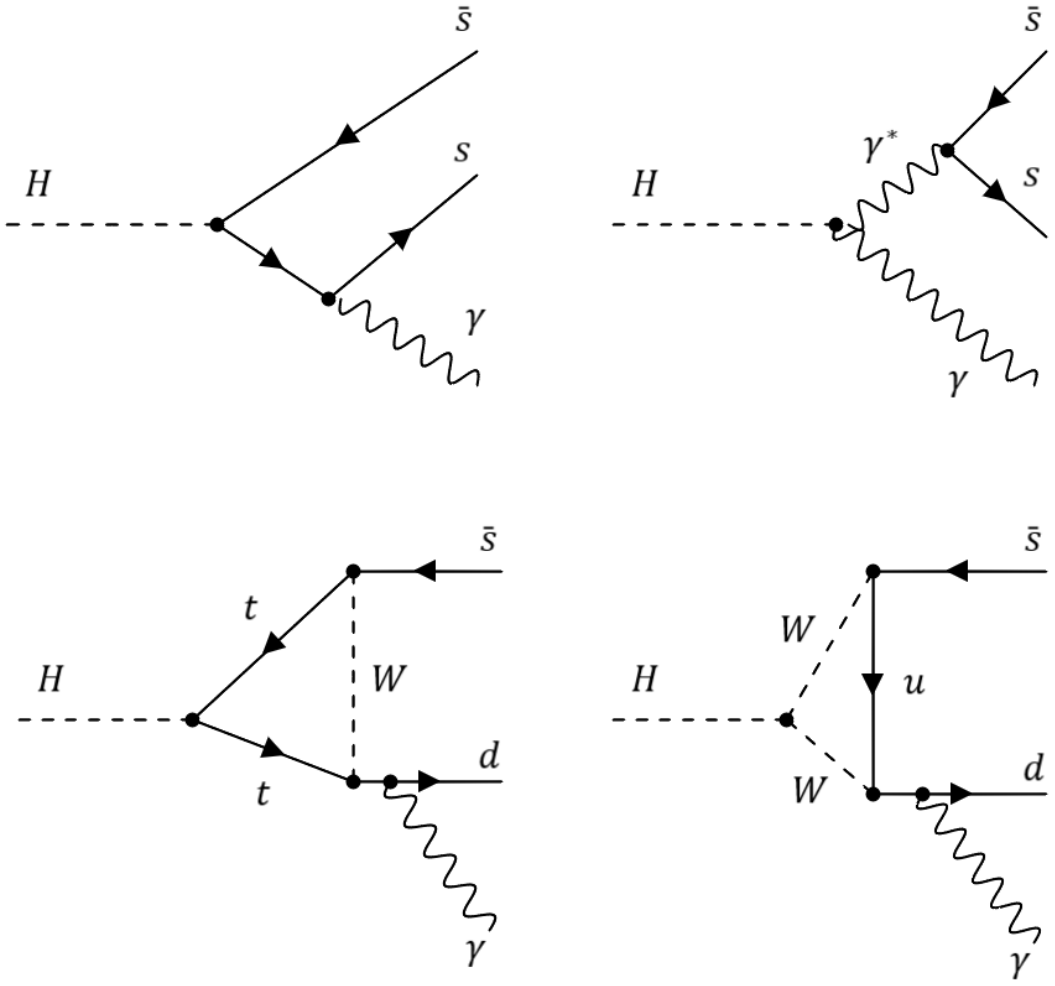

Figure 2.8: Feynman diagrams showing the different Higgs boson decay mechanisms into a photon and a light meson (top: ϕ meson; bottom: K^{*0} meson).

approach used to compute the branching ratios of the rare decays channels considered in this thesis. In [31], M. Koenig and M. Neubert propose to access the Higgs couplings to light quarks via the exclusive rare decays of a Higgs decaying in a photon along with a vector meson. In the $H \to \rho\gamma$ and $H \to \phi\gamma$ modes the final-state meson is composed of same-flavour quarks. In such

calculations, it is shown that the top right diagram of Fig. 2.8 contributes the most to the total branching ratios. This means that decays of the Higgs boson into a photon and a vector meson contain a dominant component which comes from a Higgs diphoton decay, with one off-shell photon. The direct process, shown on the top left of Fig. 2.8, contains a direct coupling between the Higgs boson and light quarks and is the only diagram contributing to the decay that gives direct access to the light quark Yukawa couplings. It can be calculated from first principles using the QCD factorization approach, which is a method that separates high-energy scattering processes into perturbative (calculable) and non-perturbative (model or data-based) components. While the contribution from this diagram is negligible in the SM, in beyond-the-standard-model (BSM) scenarios with enhanced couplings between the Higgs boson and light quarks this contribution could be significantly enhanced and deviations from the SM branching ratios could be observed because of the interference with the dominant diagram [32, 33].

The theoretical description of rare exclusive decays employs the formalism of QCD factorization, developed by Brodsky and Lepage [34], Efremov and Radyushkin [35] and others [36]. This approach provides a theoretical basis for controlling strong-interaction effects in exclusive processes with hadrons in the final state and provides an expansion of amplitudes in powers of $\Lambda_{\rm QCD}/E$, where E is the large energy of the final state hadrons. Bound-state effects are accounted for in terms of light-cone distribution amplitudes (LCDAs) of these hadrons. The LCDA of a meson can be viewed as the probability amplitude to find the valence $q\bar{q}$ Fock state in which the quark and the anti-quark carry respectively the momentum fraction x and $1-x$ of the highly boosted meson.

According to [31], the direct contribution to the decay amplitude, in which the Higgs boson couples to the quarks contained inside the vector meson (first diagram in Fig. 2.8), can be calculated using the QCD factorization approach because the energy released to the final-state meson is much larger than the scale of long-distance hadronic physics. From the most general parametrization of the decay amplitude of $H \to V\gamma$, where V is a vector meson with momentum k and a photon with momentum q, the decay rate can be written as

$$\Gamma(H \to V\gamma) = \frac{\alpha f_V^2}{8 m_H}(|F_1^V|^2 + |F_2^V|^2), \tag{2.22}$$

where α is the fine-structure constant. The decay constant f_V is an important ingredient in applying QCD to hard exclusive processes via this approach. It

provides information on the QCD interaction between the valence quark and anti-quark of the involved mesons. The decay constant is factorized out since it can be determined experimentally without adopting any specific model for flavor mixing, which complicates the definition of the decay constant. F_i^V are the form factors, momentum-dependent functions which reflect the distribution of charge Q and current, and hence the internal structure of the particle. The determination of the direct contribution to the decay rate thus relies on the evaluation of form factors F_i^V defined in Eq. 2.22. In order to do this, the corresponding partonic amplitudes can be calculated with on-shell quark and anti-quark states and then projected onto the leading-twist LCDA of a transversely polarized vector meson. The leading-twist LCDA $\phi_V^\perp$ can be viewed as the amplitude for finding a quark with longitudinal momentum fraction x inside the meson. In the calculation, it is essential to reduce hadronic uncertainties from the decay constants and those from possible new-physics effects in the dominant $\gamma\gamma$ amplitude. The main dependence of the indirect contributions on new-physics parameters can be effectively eliminated by considering the following ratio of decay rates:

$$\frac{\mathcal{B}(H \to V\gamma)}{\mathcal{B}(H \to \gamma\gamma)} = \frac{\Gamma(H \to V\gamma)}{\Gamma(H \to \gamma\gamma)} \tag{2.23}$$

One key advantage of this ratio is the insensitivity to the unknown total width of the Higgs boson. This approach allows for the direct computation of the ratio of branching fractions. Further, the sensitivity to the decay constant f_V can be eliminated considering the following ratio:

$$\frac{m_V}{\Gamma(V \to e^+e^-)} \frac{\mathcal{B}(H \to V\gamma)}{\mathcal{B}(H \to \gamma\gamma)} \tag{2.24}$$

where, as said, f_V can be directly obtained from the experimental measurements of the vector meson leptonic partial decay width

$$\Gamma(V \to e^+e^-) = \frac{4\pi Q_V^2 f_V^2}{3m_V} \alpha^2(m_V). \tag{2.25}$$

The remaining hadronic uncertainties are now confined to the calculation of the reduced form factors F_V.

For the Higgs boson mass $m_H = (125.09 \pm 0.024)$ GeV, the SM branching ratio for $H \to \gamma\gamma$ is $(2.28 \pm 0.11) \times 10^{-3}$. Utilizing this value, the branching fractions for decays into light vector mesons are derived and reported in Tab. 2.4. In this table, the uncertainties arising from the vector-meson decay constant f_V

and the $H \to \gamma\gamma$ branching ratio are distinctly reported, with the latter being the predominant source of uncertainty. On the other hand, the $K^{*0}\gamma$ mode

Branching ratio	Value
$\mathcal{B}(H \to \rho^0\gamma)$	$(1.68 \pm 0.02_{f_\rho} \pm 0.08_{H\to\gamma\gamma}) \times 10^{-5}$
$\mathcal{B}(H \to \phi\gamma)$	$(2.31 \pm 0.03_{f_\phi} \pm 0.11_{H\to\gamma\gamma}) \times 10^{-6}$

Table 2.4: Branching ratios for Higgs boson decay into meson and photon. The uncertainties arising from the vector-meson decay constant f_V and the $H \to \gamma\gamma$ branching ratio are distinctly reported.

(here and in the following collectively denoting both $H \to K^{*0}\gamma$ and $H \to \overline{K}^{*0}\gamma$ decays, which must have the same branching ratio by CPT symmetry) features a flavor-changing neutral current and is therefore very suppressed in the SM by higher electroweak orders. Example diagrams are shown in Fig. 2.8 bottom left and right. For the $K^{*0}\gamma$ decay, which arises from loop contributions, the expected branching fraction of $H \to d\bar{s} + \bar{d}s$ has a value of $\mathcal{B}(H \to d\bar{s} + \bar{d}s) = 1.19 \times 10^{-11}$ [37]. The branching fraction for $H \to K^{*0}\gamma$ is expected to be much smaller. Third and fourth diagrams of Fig. 2.8 show the radiative decay into a photon plus a flavoured meson. In the SM, this flavour changing neutral currents (FCNC) process can only proceed through a double W loop. In [38], branching fractions for $H \to \gamma + V$ with $V = K^{*0}, D^{*0}, B_s^{*0}, B_d^{*0}$, which are all excited vector states, are estimated. The authors, combining the results of [37, 32], determine the branching ratios of Higgs radiatively decaying into flavored neutral mesons through the following Effective Field Theory (EFT) + LCDA-based expression

$$\mathcal{B}(H \to \gamma + V(qq')) = \frac{1}{8\pi}\left(\frac{f_V m_V m_b}{2\lambda_V(\mu)v}\right)^2 \frac{\mathcal{B}(H \to qq')}{2m_H\Gamma_H}, \tag{2.26}$$

where $v \approx 246$ GeV is the Higgs vacuum expectation value, and all other quantities have been already defined. $\lambda_V(\mu)$ is the HQET (Heavy-Quark Effective Theory) meson first inverse moment and it plays an important role when working out rates for exclusive decays involving charm and bottom mesons. For the K^{*0} decay, a value of $O(10^{-8}) \times \mathcal{B}(H \to ds)$ has been taken for the predicted rate. The theoretical branching fractions for such exclusive FCNC radiative decays are extremely suppressed, in the range of $O(10^{-14} - 10^{-26})$. The branching fraction predicted using Eq. 2.26 is reported in Tab. 2.5. Therefore, flavored meson decays of the Higgs boson are exceedingly rare and are not expected to be observable with current or future collider technology, and therefore an effective probe of

BSM physics. Any observable enhancement in FCNC decays could potentially provide significant insights into BSM phenomena.

Branching ratio	Value	Framework
$\mathcal{B}(H \to K^{*0}\gamma)$	1.0×10^{-19}	EFT+LCDA

Table 2.5: Branching ratios prediction for exclusive Higgs decays to a photon plus a meson.

2.7 Modifications of Higgs couplings in BSM scenarios

Despite its success in the description of the strong and electroweak interactions and of the Higgs mechanism and properties, the SM theory presents unsolved issues and seems to be valid only at the energies explored by the present hadron colliders. The most notable SM theory problems are, for instance, the non-inclusion of the gravitational force, the assumed massless neutrinos, which have been measured massive by several experiments by observing the so-called neutrino oscillation (e.g. at the Superkamiokande experiment), the unexplained baryogenesis, dark matter and dark energy.

In high-energy physics, there are currently no direct experimental measurements for the Yukawa couplings of the Higgs boson to the first-generation quarks. Consequently, it is plausible to consider theoretical models that predict significant deviations in these couplings from the SM expectations. For example, in [39], whose approach drastically modifies the Higgs branching ratios with respect to the SM predictions, it was proposed that the Yukawa couplings may depend in a non-trivial way on the Higgs field, and that this might explain the hierarchies seen in the spectrum of fermion masses. More precisely, in the context of an effective field theory valid beneath the new-physics scale M, the Yukawa couplings are postulated to be functions of the Higgs field H. Thus, the Yukawa couplings can be expanded as

$$Y_{ij}(H) = \sum_{n=0}^{\infty} c_{ij}^{(n)} \left(\frac{H^\dagger H}{M^2} \right)^n , \tag{2.27}$$

where i, j are indices representing the generations of fermions. The exploration focuses on the hypothesis that the hierarchical structure of fermion masses arises

from specific powers of $\langle H \rangle / M$. It is assumed that the coefficients $c_{ij}^{(n)}$ become significant only at a particular order correlated with the generational indices. In scenarios where the Higgs field acquires a *vev* $\langle H \rangle \equiv v \ll M$, the resulting fermion masses are hierarchically small, dependent on the parameters $n_{ij}^{u,d}$. Concurrently, the Higgs boson coupling to fermions of flavors i, j is enhanced by a factor $2n_{ij} + 1$ compared to SM predictions. A noteworthy feature of this framework is the substantial alteration of the Higgs branching ratios relative to SM expectations. While the Higgs couplings to weak gauge bosons and to the top quark remain consistent with SM (thus maintaining the same couplings to gluons and photons), significant deviations are predicted in the Higgs interactions with other fermions:

$$\frac{\Gamma(H \to b\bar{b})}{\Gamma(H \to b\bar{b})_{\text{SM}}} = \frac{\Gamma(H \to c\bar{c})}{\Gamma(H \to c\bar{c})_{\text{SM}}} = \frac{\Gamma(H \to \tau^+\tau^-)}{\Gamma(H \to \tau^+\tau^-)_{\text{SM}}} = 9, \quad \frac{\Gamma(H \to \mu^+\mu^-)}{\Gamma(H \to \mu^+\mu^-)_{\text{SM}}} = 25. \tag{2.28}$$

Although the authors do not explicitely show the results, the Higgs couplings to light quarks are enhanced even further. The enhancement of the coupling to μ can be very important in view of a possible muon collider, since the Higgs production rate is predicted to be a factor of 25 larger than that in the SM.

Other proposed models that postulate enhancements in the Higgs couplings to light fermions encompass the minimal flavor violation framework [40], the Froggatt-Nielsen mechanism [41] for a hierarchical structure of Yukawa couplings, the Randall-Sundrum model family [42], and the hypothesis of the Higgs boson as a composite pseudo-Goldstone boson [43].

The Compact Muon Solenoid Experiment 3

This PhD thesis project has been realized with a data samples collected using the CMS detector at the Large Hadron Collider (LHC), located at CERN (European Organization for Nuclear Research) in Geneva. LHC was conceived to investigate the physics of the Standard Model and answer the fundamental open questions about the laws governing particle physics and its interactions.

The CERN laboratory was created in 1954 as an organization involving 12 European countries. After the Higgs boson discovery in 2012, several areas of high energy physics are currently explored, such as the supersymmetry theory, SM extensions, searches for rare decays and other particle properties.

3.1 The Large Hadron Collider

The LHC is the world largest and most powerful particle accelerator, starting its operation at CERN in 2009. LHC is a superconducting accelerator designed to collide proton and heavy-ion beams, consisting in two rings of 27 kilometers circumference. The center of mass energy and instantaneous luminosity have been increasing since its activation, being now $\sqrt{s} = 13.6$ TeV for p-p collisions and luminosity around $2 \cdot 10^{34}$ cm^{-2}s^{-1}. The protons are produced from hydrogen ionization and speeded up by a chain of preaccelerators, which increase their energy each step before being injected into the large collider. Figure 3.1 shows the CERN accelerator complex. The first step for the protons consists in an acceleration to an energy of 50 MeV in the Linear Accelerator (LINAC2). Then the beam is boosted in the Proton Synchrotron Booster (PBS) where the protons

are speeded up to 1.4 GeV. Next step is the Proton Synchrotron (PS) where protons run until they reach an energy of 26 GeV, and then are injected in the Super Proton Synchrotron (SPS), in which are accelerated up to 450 GeV. The latter is the last step before the final injection in the two beam pipes of the LHC. Protons are divided in two beams running in opposite directions. After about 5 minutes each LHC ring is filled, and in about 20 minutes the protons gain the maximum energy of 6.8 TeV. The beam pipes are two tubes kept at ultrahigh

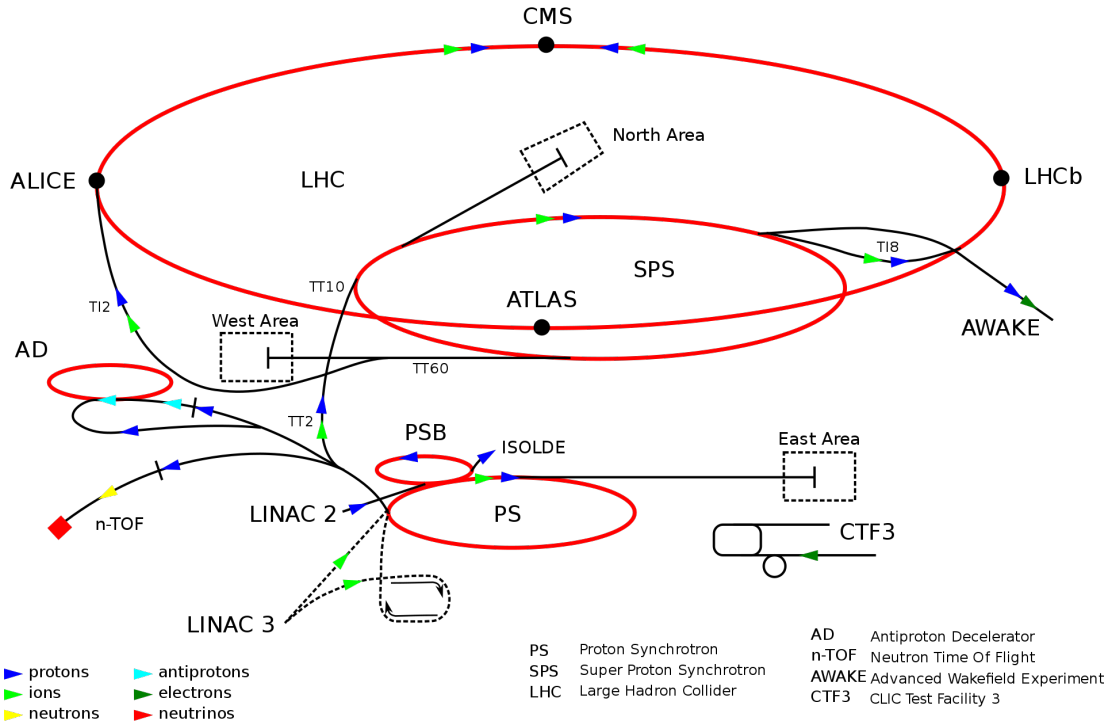

Figure 3.1: A schematic representation of the CERN accelerator complex.

vacuum. Several superconducting electromagnets generate a magnetic field which guides the beams around the accelerator rings, with a maximum magnetic field of about 8 T. Several magnets of different sizes are implemented: 1232 dipole magnets are used to keep the beams at high energy around the accelerator, quadrupole magnets to collimate the beams and sextupole magnets to pinch the beams to the intersection points, in order to increase the probability of collision. The protons are collected in $n_b = 2808$ bunches composed of $N_b = 10^{11}$ protons each. Each bunch is separated by about 25 ns, therefore the bunch crossing rate is 40 MHz. When fully operational, the inelastic collision rate is of the order of 10^9 Hz, with ~ 40 collisions per bunch crossing. Considering a revolution frequency $f_{\text{rev}} = 11$ kHz, the beta function at the collision point $\beta^* = 0.55$ m

(β^* indicates the beam focalization, corrected by a factor of γ_r), the transverse beam emittance ϵ_n, the geometric luminosity reduction factor F (an index of the crossing angle at the interaction point), the instantaneous luminosity is given by

$$L = \frac{f_{\text{rev}} N_b^2 n_b \gamma_r}{4\pi\epsilon_n \beta^*} F.$$

Along the LHC tunnel four detectors are located: CMS (Compact Muon Solenoid) and ATLAS (A Toroidal LHC ApparatuS), multi-purpose experiments with a wide physics program. ALICE (A Large Ion Collider Experiment) is devoted to heavy ions physics for quark-gluon-plasma studies and LHCb (LHC beauty) aimed at studying rare decays and CP violation in the b-sector.

3.2 A CMS Overview

As mentioned before, the Compact Muon Solenoid has been designed to study the p-p collisions at the LHC in order to test the SM theory.
The CMS detector is installed at the interaction point n.5 in the LHC tunnel. The overall layout of CMS is shown in Fig. 3.2 and a photography of the CMS section in Fig. 3.3 .
CMS is equipped with a superconducting solenoid magnet and has a cylindrical symmetry coaxial to the beam axis, composed of a central part, called *barrel*, which is enclosed by two disks, called *endcaps*. The entire structure is 21 m long, with a section of 7.5 m radius for a total weight of 7500 tons. A subdetector list with generical descriptions, starting from the inner part closest to the collision region, is reported below:

- *inner tracking system*: silicon detectors organized in pixels and strips, designed to reach a very high resolution in vertex reconstruction and in particle momentum meausurement.

- *electromagnetic calorimeter* (ECAL): a scintillating crystal calorimeter for high performance in photon and electron energy resolution, with wide coverage and granularity

- *hadronic calorimeter* (HCAL): calorimeter for precise measurements of jets and missing transverse energy.

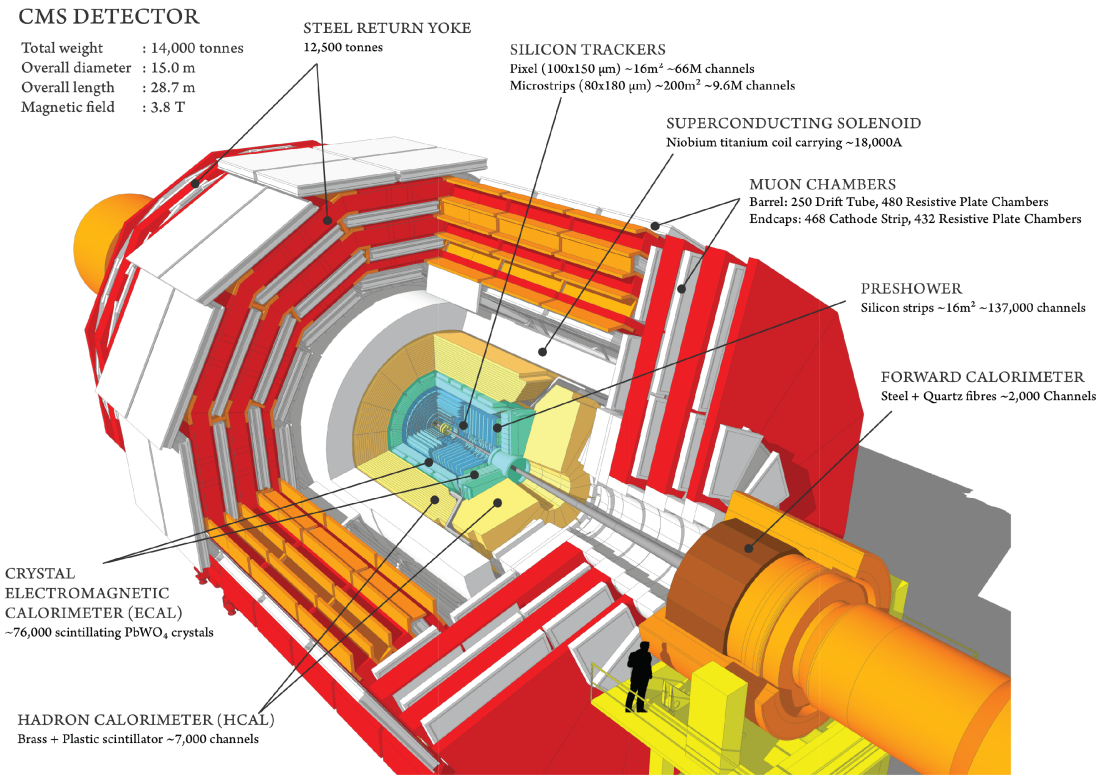

Figure 3.2: A schematic c view of CMS detector and its subdetectors.

- *superconducting magnet*: a solenoidal magnet 13m-long with a radius of 3m, providing a magnet field of about 3.8T, which allows to measure particle momenta in the inner tracking system

- *muon detecting system*: a high performance system to identify muons and measure their momenta up to several TeVs.

A more detailed description of the detector components follows.

3.3 The coordinate system

The CMS coordinate system has its origin in the nominal interaction point and exploits the cylindrical symmetry of the apparatus. The x axis points to the centre of the LHC, the y axis points upwards, perpendicularly to the LHC plane. The z axis towards the anti-clockwise beam direction, pointing toward the Jura mountains from the LHC Point 5 where the CMS experiment is located.

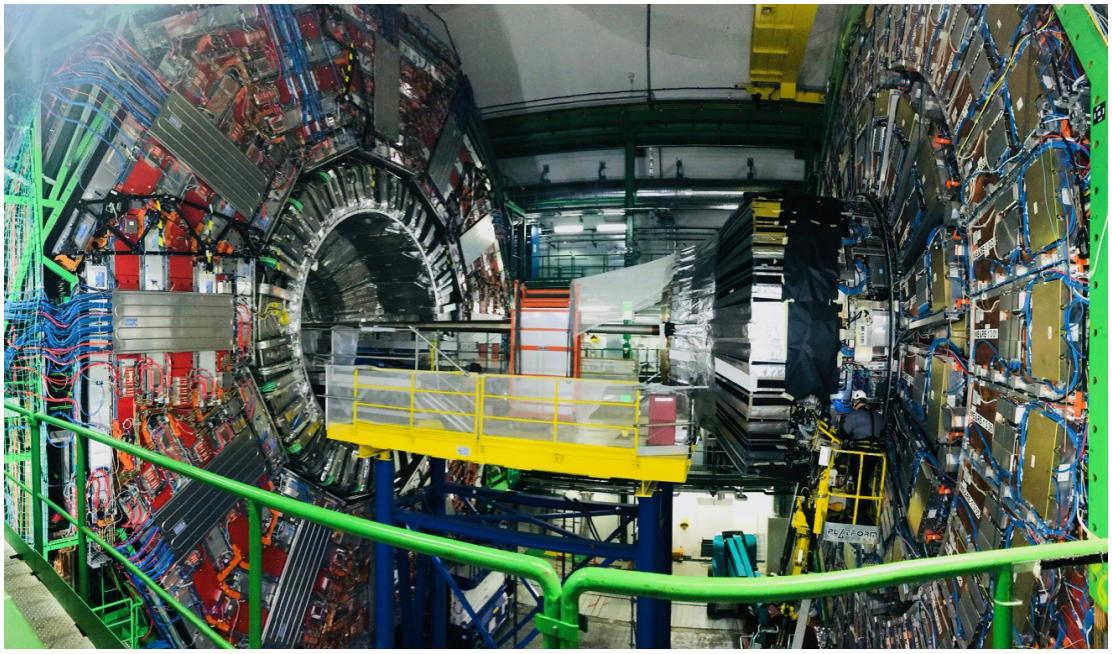

Figure 3.3: A CMS section photo.

An angular reference system is used through this thesis, from which many variables are derived:

- *polar angle* θ measured from the positive z axis
- *azimuthal angle* ϕ measured in the xy plane
- *transverse momentum*, $p_T = p \sin\theta$, is the particle momentum component that lies in the xy plane. The convenience in using p_T instead of p is based on the Lorentz-invariance property of the transverse momentum and the fact that its initial value in the collision is zero;
- *transverse energy*, $E_T = E \sin\theta$, is a Lorentz-invariant quantity and it is equivalent to the transverse momentum (times c) if the particle is massless;
- *pseudorapidity*, $\eta = -\log(\tan\frac{\theta}{2})$: in the limit where the particle is travelling close to the speed of light, the *rapidity* defined as

$$y = \frac{1}{2}\ln\left(\frac{E + p_z}{E - p_z}\right) \tag{3.1}$$

converges to the pseudorapidity. The crucial property of this quantity, that leads acceleratorists to favor pseudorapidity instead of the θ angle, is

that the difference of rapidity of two particles is Lorentz-invariant under a boost along the z axis. Furthermore, the number of particles produced during a collision in a $d\eta$ interval $dN/d\eta$ is invariant along the z axis. In Fig. 3.4 some examples are reported of pseudorapidity values to give an idea of its relation with the polar angle.

- $\Delta R = \sqrt{\Delta\phi^2 + \Delta\eta^2}$ is used to quantify the distance in the $\phi - \eta$ plane between two particles. ΔR has been used in this thesis to define a z–boost invariant cone opened around a single particle direction or detector position, in order to study nearby detector activity.

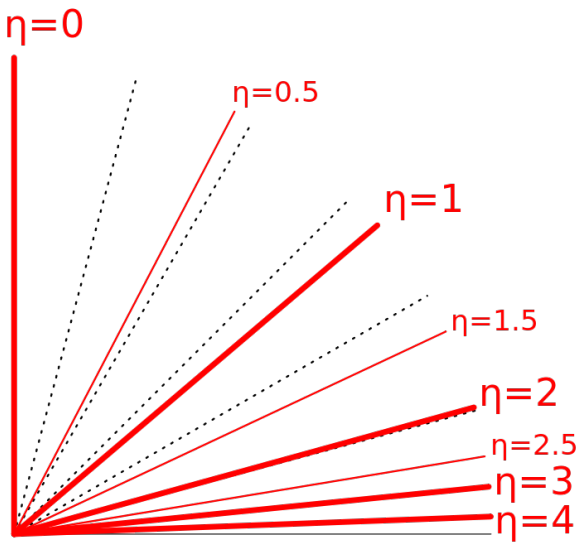

Figure 3.4: Pseudorapidity values shown on a polar plot.

3.4 The magnet

The magnetic field has been designed to have a strong bending power, in order to achieve the best resolution possible on the calculation of the transverse momentum of charged particles. CMS chose a single superconducting solenoid producing an intense field. The magnet is a 13m-long and 5.9m-diameter cylinder of Niobium-Titanium wired coils, providing a uniform magnetic field of 3.8 T [44]. Furthermore, this high magnetic field offers a momentum resolution better than 10% at 1 TeV.

The magnets are made by coils of copper-clad Nb-Ti at operating temperature of 1.9 K (-271.25°C). A nominal current of 19 kA circulates in the cables and a total energy of 2.6 GJ is stored in the magnetic system. The lines of the field are closed in the iron–yoke, where the muon system is located, reaching a magnetic field of about 2 T and pointing in two opposite directions in the tracking and in the muon systems. The iron-yoke is 1.55 m-thick in the barrel and 1.45 m in the endcap.

An example of muon track is shown in Fig. 3.5.

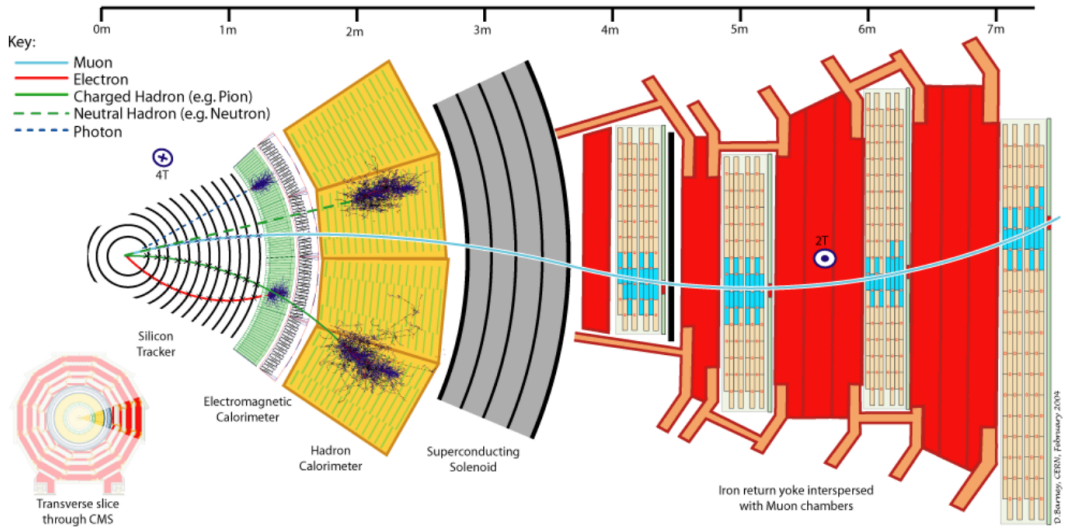

Figure 3.5: A section view of the barrel region with some examples of particle-tracks.

3.5 The silicon tracker

The silicon tracker is the innermost detector, the closer component to the collision point. It is designed to reconstruct with the highest precision possible the tracks of charged particles coming from the interaction point. It has a length of 5.8 m, a diameter of 2.5 m and is fully immersed in the magnetic field described in the previous Sec. 3.1. The silicon tracker is also conceived to work in a highly-radioactive and high-particle-flux environment. To achieve a good precision and fast response in such environment, the tracking system is composed by high-granularity silicon detectors.

A charged particle traversing the silicon tracker detector produces signals on nearby pixels, which are combined in a hit. A three–dimensional measurement

of the hit position is obtained thanks to the high granularity, by calculating weighted average through the charge collected within a hit. The resulting hit position resolution is approximately 10 μm in the transverse direction and 20-40 μm in the longitudinal direction, depending on η. The granularity decreases moving outwards from the collision point, distinguishing three regions. The first, the inner one, where the particle flux is reaches its maximum ($\approx 10^7$ s^{-1} at $r \approx 10$ cm), consists in five layers of pixel detectors sized $\approx 100 \times 150$ μm^2. The intermediate region from 20 to 55 cm from the interaction point the particle flux decreases enough to allow the use of silicon microstrip detectors with strip sized 10 cm $\times$ 80 μm. The further region from the center is located in the minimum value of the particle-flux above these three regions, low enough to adopt larger strips detectors, sized 25 cm $\times$ 80 μm. In total, up to 10 layers of strip detectors are present, depending on the pseudorapidity region.

During the technical break at the end of 2016, the pixel tracking system underwent an upgrade in anticipation of higher particle fluence for the remaining portion of Run 2. This upgrade was designed to address radiation damage due to the enhanced luminosity environment, which can impair the charge collection efficiency of modules, leading to diminished spatial resolution, especially for components nearest the beamline. The resultant increase in the number of pileup interactions negatively affects the physics performance by lowering tracking efficiencies. The upgrade enhanced the granularity of the readout components and added an additional cylindrical layer, increasing the total to one more. This adjustment enables four spatial measurements along the charged particle's trajectory in the barrel region, at radii of 2.9, 6.8, 10.1, and 10.6 cm. Additionally, a new silicon disk was inserted into each endcap section, providing measurements at longitudinal distances of ±29.1, ±39.6, and ±51.6 cm. These enhancements have achieved an impressive spatial resolution of approximately 13 and 20 μm in the transverse and longitudinal directions, respectively. The newly incorporated components are designed to be lower in mass to keep the material budget reasonable while being more resistant to radiation than their predecessors. A diagram of the updated tracker layout is presented in Fig. 3.6.

The tracker detector covers a pseudorapidity range of $|\eta| < 2.5$ allowing the measurement of all the charged particles within this range. In order to reduce the amount of processes such as multiple scattering, bremsstrahlung and photon conversion, the material budget has been kept to a minimum. Figure 3.7 reports the material budget of the silicon tracker, as a function of η. The material budget

is equivalent to ≈ 0.4 - 2 radiation lengths, X_0 or ≈ 0.14 - 0.56 nuclear interaction lengths, λ_I [45].

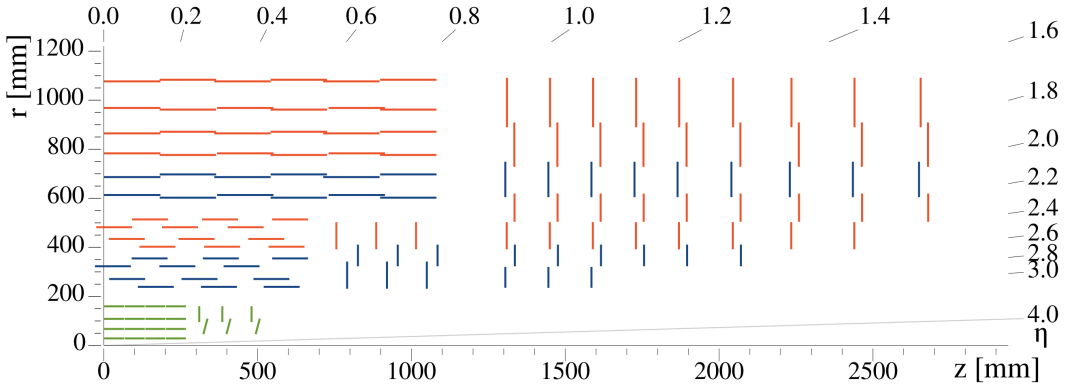

Figure 3.6: Illustration of a quarter section of the Phase-1 CMS tracking system, viewed in the r-z plane. The pixel detector is represented in green, and the single-sided and double-sided strip modules are shown in red and blue, respectively.

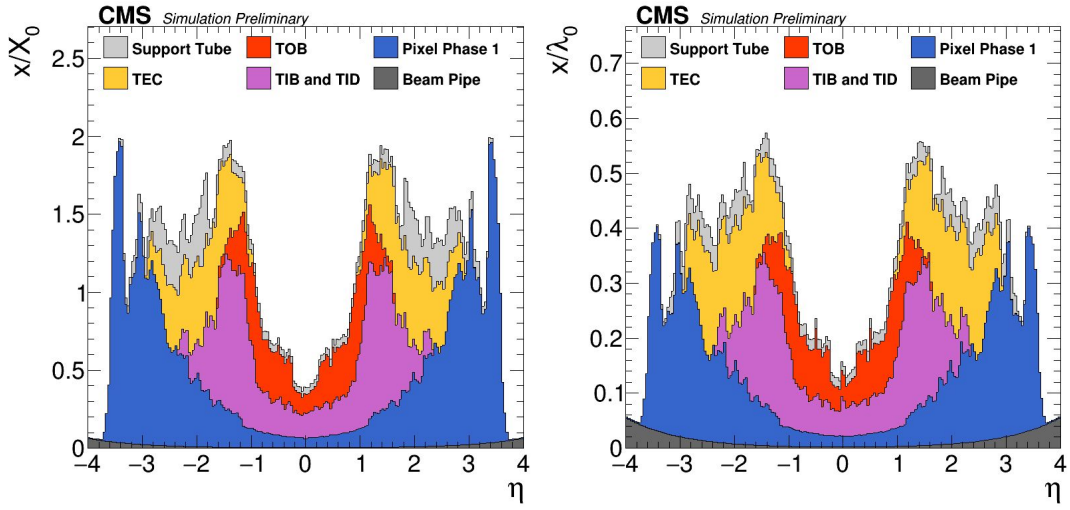

Figure 3.7: Total material budget of the inner tracking system as a function of pseudorapidity, expressed in units of radiation length (on the left) and in units of interaction length (on the right).

3.6 ECAL

The electromagnetic calorimeter (ECAL) [46] has been designed to measure with high precision the energy of electrons and photons. Its design was guided by the search for the Higgs boson, exploiting the clean signature of its $H \to \gamma\gamma$

channel, which was considered one of the "golden" channels for the Higgs boson discovery.

ECAL, located after the inner tracker, is a hermetic homogeneous calorimeter made of 75848 scintillating crystals of lead tungstate ($PbWO_4$), with an array of photodetectors placed after a preshower detector. The high granularity is achieved by a high density $\rho = 8.28$ g/cm^3 and also by a small Molière radius $R_M = 2.2$ cm, which translates to a good lateral shower containment. Furthermore, the fast time response of crystals allows for 80% of the scintillation light to be emitted within 25 ns. This makes ECAL suitable for an environment with such high rate of bunch crossing as LHC. The ECAL general layout is shown in Fig. 3.8. ECAL has a cylyndrical geometry:

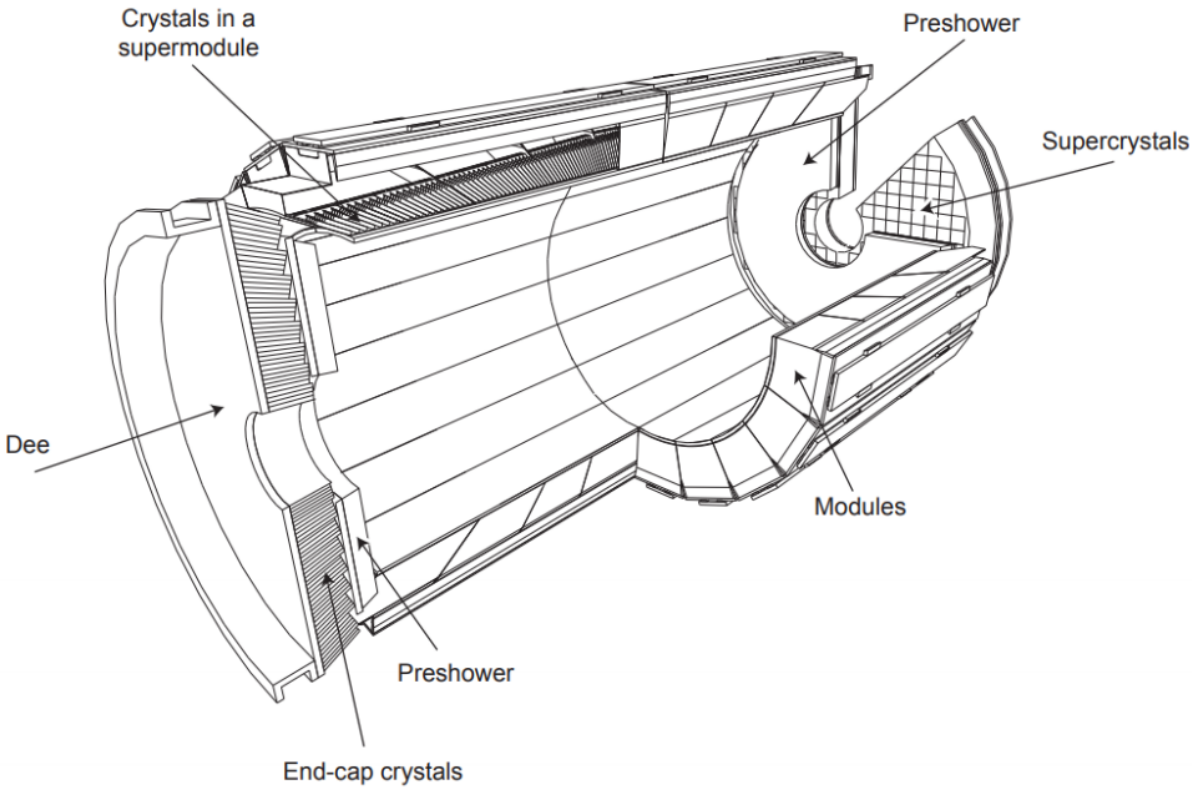

Figure 3.8: Layout of the CMS electromagnetic calorimeter

- *the barrel* (EB): it covers the pseudorapidity range $|\eta| < 1.479$. It is made of 36 identical supermodules. Each supermodule is made of four modules

which contain 400 or 500 trapezoidal-shaped crystals, each one of 230 mm length and and frontal cross section 22 × 22 mm^2.

- *the endcaps* (EE): they cover the pseudorapidity range $1.479 < |\eta| < 3.0$. EE is made of crystals with length 220 cm and frontal cross section of 28.62 x 28.62 mm^2 organized in two semi-circular "dees" (name coming from the D shape of the region) containing 3662 crystals.

- *preshowers* (ES): two preshower detectors are implemented in the endcaps. ES covers the pseudorapidity range $1.7 < |\eta| < 2.6$. They have a total thickness of 20 cm, corresponding to about 3 X_0 and are designed to help to identify electrons against minimum ionizing particles and discriminate $\pi_0 \rightarrow \gamma\gamma$ decays from single photons. It is made of two alternate layers of lead and silicon strip detectors.

The energy resolution for ECAL is given by

$$\left(\frac{\sigma}{E}\right)^2 = \left(\frac{a}{\sqrt{E}}\right)^2 + \left(\frac{\sigma_N}{E}\right)^2 + c^2$$

where E is the energy of electrons or photons in GeV, a includes the statistical fluctuations of the shower containments, σ_N is the noise term (electronic noise) and c is a constants term depending on non-uniformity of the light collected by the calorimeter, non-uniformity of the intercalibration and losses of energy. For the barrel region, the energy resolution is between 1.1% and 2.6% for photons with $E_T \sim 60$ GeV and is better than 2% for the electrons from Z$\rightarrow ee$ decays with $E_T \sim 45$ GeV. For the endcaps region, it is between 2.2% to 5% for both photons and electrons.

3.7 HCAL

The aim of the hadronic calorimeter (HCAL) is to measure the energy of hadrons and jets [47]. Figure 3.9 shows the longitudinal scheme of HCAL. The principal components are four: Hadron Barrel (HB), Hadron Endcap (HE), both inside the solenoid magnet, Hadron Outer (HO), outside the magnet but inside the barrel, and Hadron Forward (HF), which covers the forward zone up to a pseudorapidity of $\eta = 5.2$. HCAL therefore covers an extended pseudorapidity range with respect to the tracking system. This allows to capture a large fraction

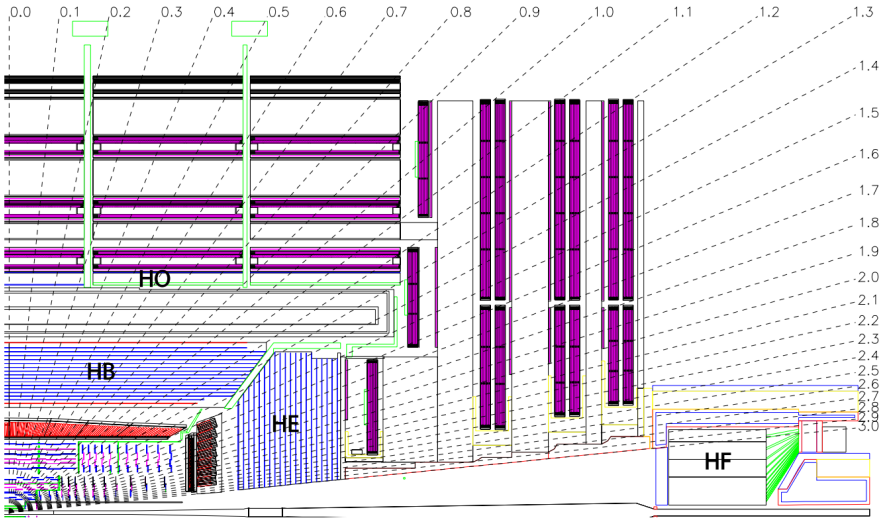

Figure 3.9: Layout of the CMS hadronic calorimeter. The HB, HE, HO and HF components of the detector are highlighted.

of particles achieving a precise detection for neutrinos via measurements on missing transverse energy.

HCAL is a sampling calorimeter. It is made by brass layers, as absorber material. Plastic scintillators intersperse the brass layers in HB and HE. Wavelength-shifting optic fibres are installed in the scintillators tiles to convert scintillation light coming from the projective towers of HB and HE calorimeters. Then the light is detected by hybrid photodiodes and amplified. In HF, plastic scintillators are replaced by quartz fibers, interspersed with layers of iron absorber. HCAL has a total thickness of 7 interaction lengths (λ_0). A complete containment of the shower requires a greater amount of material. To solve this, an additional layer, H0, corresponding to one λ_0 has been added outside the magnet to let HCAL to improve energy resolution.

3.8 Muon system

Inside the iron of the magnet return yoke, the CMS muon system [48] has been designed to measure with high precision muon momenta and determine the electric charge, exploiting the high magnetic field. Three types of gas-ionization chambers compose this system: Drift Tubes, Cathode Strip Chambers and Resistive Plate Chambers. All the information coming from chambers is merged with the one coming from the tracker to achieve more precise measurements.

The muon tracking system is divided in a cylindrical barrel section and two planar endcap regions:

- *Drift Tube Chambers* (DT) are embedded in the barrel region $|\eta| < 1.2$. The chambers are shown in Fig. 3.10 and are split in 4 station, each with 8 layers of tubes for the measurement of the muon bending in the transverse plane and 4 layers in the longitudinal plane. Each chamber contains a stretched wire within a gas volume, which is a mixture of argon (85%) and carbon dioxide (15%), reaching a saturated drift velocity of about 55 µm/ns.

- *Cathode Strip Chambers* (CSC) are installed in the endcaps in a region $0.9 < |\eta| < 2.4$. The fine segmentation, the radiation hardness and the fast response allows the CSC to operate within the high particle flux of this region. CSC are 468 wedge-shaped multi-wired chambers and also these are divided in four stations, interspersed within the stainless steel flux return of the magnet. The good time resolution allows to correctly identify the bunch-crossing from which the muon is coming.

- *Resistive Plate Chambers* (RPC) are located in both central and endcap region, for $|\eta| < 1.6$. RPCs are fast detector that operates in avalanche regime. They consists in parallel anode and cathode plates with a gas gap. The time resolution is below 2 ns.

3.9 The Trigger System

Currently, the LHC operates at an instantenous luminosity of $L(t) = 2 \cdot 10^{34}$ $\text{cm}^{-2}\text{s}^{-1}$ and a bunch crossing frequency of 40 MHz. As already mentioned, 25 ns is the time interval between two consecutive bunches so this corresponds to a rate of 10^9 events per second. Furthermore, multiplying the bunch crossing frequency by the so called *pile-up* (PU) parameter, i.e. the number of collisions per bunch crossing, currently identified by a number between 25 and 70, the number of events to record is very high. Considering that the size of a raw event recorded is about 1 MB, saving all the events is not possible. Therefore, a trigger system has been implemented to preselect events in real time. An online trigger system has to be efficient for the selection of the interesting events, while rejecting most of the events deemed useless for physics analysis and calibrations.

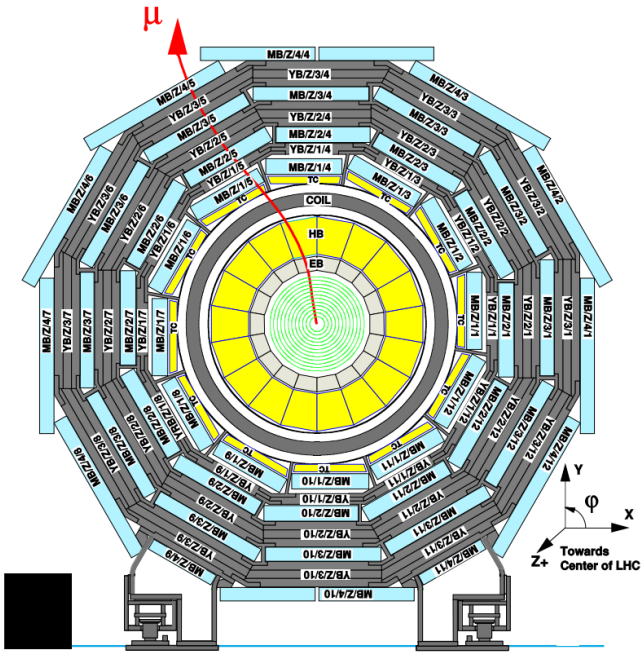

Figure 3.10: Schematic representation of the CMS barrel muon drift chambers.

The CMS trigger has been designed split in two steps to ensure a rate reduction:

- *Level-1 Trigger* (L1): a series of hardware processors that make selections only based on information from the calorimeters and the muon system, the only ones available at this stage. This is due to the fact that the designed latency of the L1 trigger is about 3.2 μs and makes impossible to use information from the entire detector. The maximum design trigger rate of 100 kHz for L1 corresponds to a minimum rejection rate of 10^4.

- *High Level Trigger* (HLT): the HLT is implemented at the software level. It provides a selection of the events that passed the Level-1 trigger, having access to all the information used in and stored by L1. HLT, thus, makes further combinations and topological calculations on the list of object provided by L1 adding also some information from the tracking system. The rate of events that pass the HLT selection is currently up to 1 kHz.

3.10 Particle identification and reconstruction

This section describes the techniques and algorithms used for identification and reconstruction of the particles detected in CMS. High level objects characterize the event:

- *tracks*: charged particle trajectories reconstructed in the tracking system
- *hits*: signals in pixel detector which in sequence identify the track of a charged particle
- *calorimeter clusters*: collection of towers where particles deposit their energy in either ECAL or HCAL
- *primary vertex*: track reconstruction allows to recognize spatially the precise location of the p-p interaction and identify the vertex of the hard collision, called primary vertex.

The analysis presented in this thesis work studies the rare decays $H \rightarrow \rho/\phi/K^{*0}\gamma$. For this purpose, it is necessary to correctly identify and reconstruct the final state of this process, relying on a correct discrimination between electrons and photons and in a precise identification of jets and tracks. CMS has developed an event reconstruction based on the *particle-flow techniques* (PF).

3.11 Particle-flow techniques

The PF algorithm [49] exploits the information stored by the entire list of CMS subdetectors making a combination and optimizes it in order to provide a correct reconstruction and identification for each particle, like muons, electrons, photons, charged hadrons and neutral hadrons. These particles reconstructed by *particle flow* are then used to reconstruct jets, b-jets, hadronic τ decays, and the missing transverse energy of the event. The transverse momentum of muons is calculated from the curvature of the track, bending under the magnetic field. The momentum of charged hadrons is measured in the tracker and, merging the information from the energy deposit in ECAL and HCAL, the energy of the charged hadrons can be calculated. The energy of neutral hadrons is provided by HCAL clusters not associated with a charged track. The energy of electrons is measured combining the electron momentum at the primary interaction vertex

provided by the tracker information, the energy deposited in an associated ECAL cluster and the energy sum of all bremsstrahlung photons spatially compatible with the electron track. The energy of non-converted photons is directly obtained from the ECAL measurement of clusters not associated with charged tracks.

3.12 Track and vertex reconstruction

The trajectory of a charged particle within the CMS detector is reconstructed by merging the trail of hits left on the tracker layers. This process is guided by an algorithm known as the Combinatorial Track Finder (CTF) [50]. The CTF algorithm involves three main stages: seed generation, track finding, and track fitting.

- **Seed Generation:** this initial stage utilizes the hit information from the pixel detector. The choice of the pixel detector is due to its high efficiency, low occupancy, and superior resolution in determining the two-dimensional position.
- **Track Finding:** in this stage, a Kalman filter algorithm [51] is employed. This algorithm extrapolates the track sequentially from the beam interaction point outward. The trajectory is projected onto each tracker layer, and hits are assigned to tracks based on the χ^2 value between the predicted and measured positions.
- **Track Fitting:** the final stage involves refitting all valid tracks using a Kalman filter and a secondary filter that runs backward towards the beam spot, based on the outcomes of the first filter.

Each track is evaluated and assigned a quality criterion based on the χ^2 value and the number of missing hits. Figure 3.11 illustrates the expected performance of track reconstruction for muons and pions at various transverse momenta. The muon track reconstruction efficiency is approximately 99% for $|\eta| < 2.1$, beyond which it decreases due to the limited coverage of the forward pixel detector. Conversely, the lower efficiency for pion track reconstruction is attributed to their interaction with the tracker material. Once the tracks have been reconstructed, a vertex reconstruction algorithm is employed. This algorithm clusters the tracks that appear to originate from the same interaction vertex and determines

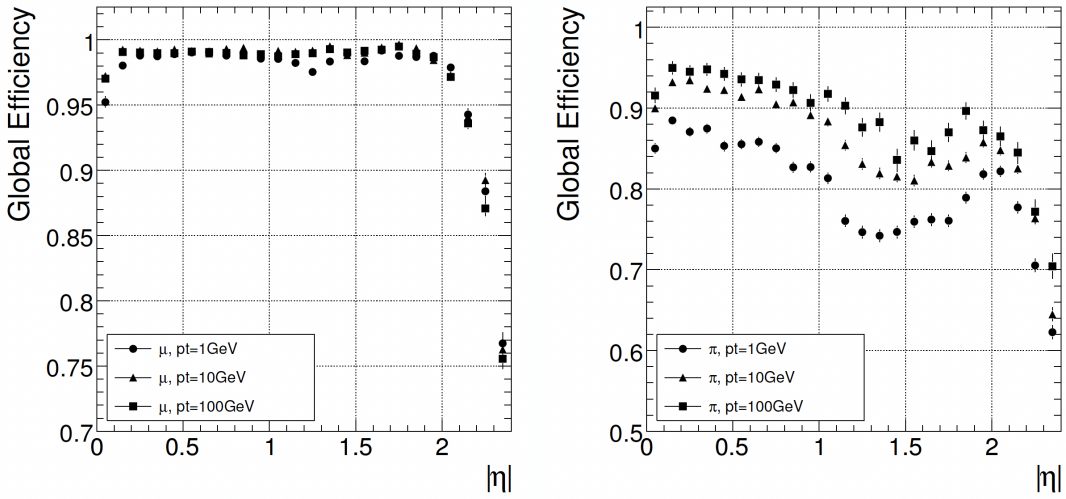

Figure 3.11: Track reconstruction efficiency for muons and pions as a function of pseudorapidity for different transverse momentum.

the position of each vertex using its associated tracks. The vertices are then arranged based on the quadratic sum of the transverse momenta (Σp_T^2) of the tracks associated with each vertex. The primary vertex is identified as the one with the highest sum of p_T^2. Other vertices are considered to be the result of PU interactions. These PU interactions occur due to multiple proton-proton (p-p) collisions happening within the same bunch crossing.

3.13 Electron reconstruction

An electron deposits most of its energy in the ECAL after having lost some energy through the tracker. Therefore, it is necessary to combine both information from ECAL and the tracker to provide a precise measurement of the electron momentum. Electron trajectories are reconstructed from tracks with a dedicated procedure, which consist in finding two or three hits in the silicon tracker considering to be the first hits. Exploiting a model based on calculation of the energy loss with a Bethe-Bloch function, the track is entirely reconstructed, proceeding with iterations from the track parameters retrieved by each layer. If other hits are compatible with the reconstructed one, several tracks candidates are developed, with a limit of five candidate trajectories for each layer. Each electron track must not have more than one missing hit in the layers of the inner tracker. Furthermore, the transverse (d_{xy}) and longitudinal (d_z) impact

parameters must be compatible with the electron origin in the primary vertex. A common issue in electron reconstruction in CMS is the *bremsstrahlung* along the electron path and the subsequently photon conversion in a positron-electron pair, causing thus an incorrect measurement of the electron energy. In order to solve this problem, a dedicated technique has been developed, divided in three steps and is called *PF clustering*. First, local crystal energy deposits above a given threshold are identified as *cluster seeds*. The second step consists in the aggregation of crystals adjacent. The corresponding seeds energies, if above a threshold, are merged in order to create a *topological cluster*. Lastly, presumptive clusters of bremsstrahlung photons and conversions products are merged and then assembled into *PF superclusters*. In order to identify the electrons, multivariate techniques (MVA) are used. Isolation and shower shape are examples of variables given in input to MVA. In Fig. 3.12 the electron identification efficiency is reported as a function of the transverse momentum.

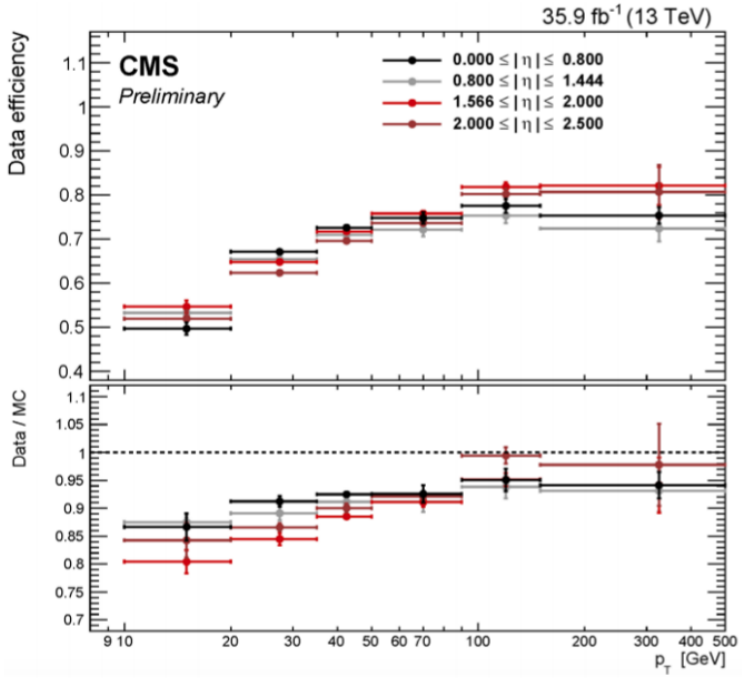

Figure 3.12: The electron ID efficiency as a function of p_T.

Working point	Tight muon ID
Strip hits	> 5
Pixel hits	> 0
Muon chamber with segments	> 1
Global fit	$\chi^2_{\text{dof}} < 10$
Hits in muon system	> 0
Transverse impact parameter	$\lvert d_{xy} \rvert < 2$ mm

Table 3.1: Muon ID requirements table.

3.14 Muon reconstruction

Muons with $p_T > 3$ GeV typically leave hits in the inner tracker, then travel through the CMS calorimeters with minimal energy deposit and leave hits in the muon chambers. This allows the muon identification and reconstrution exploiting information from both inner tracker, defined as *tracker muon reconstruction* and muon chambers, called *standalone muon reconstruction*. The standalone reconstruction consists in measurements in the pseudorapidity range $|\eta| < 2.4$, taking the track segments from local reconstruction within the muon chambers. The inner tracker reconstruction considers only tracks with $p_T > 0.5$ GeV and a total momentum > 2.5 GeV. In order to improve the muon momentum resolution, the *Global Muon reconstruction* matches the information from the standalone and the tracker reconstruction. Also a global–muon track is fitted combining hits from the tracker track and standalone–muon track, ensuring a better momentum resolution for tracks with $p_T > 200$ GeV, thanks to the muon chambers, and a more efficient calculation of low-momentum tracks with $p_T < 5$ GeV, thanks to the inner silicon tracker. Muon identification requirements are reported in Tab. 3.1. These are based on the compatibility with the primary vertex, on the reduction of the identification of muons within jets with high efficiency, ensuring also a low rate for the misidentification of charged hadrons as muons.

3.15 Photon reconstruction

Photons are reconstructed from clusters of ECAL channels around energy deposits, which are merged into superclusters. The material located in front

of the ECAL leads to photon conversion in positron-electron pairs which in their turn may generate photons via the bremsstrahlung effect. The magnetic field, bending the positron and electron trajectories, tends to spread the energy of the electromagnetic shower towards the tracker detector along the ϕ angle. Thus, in order to extrapolate the radiated energy of the shower a dynamic clustering algorithm has been developed. A supercluster (SC) is promoted to a photon candidate, if its transverse energy is greater than 10 GeV. It uses a topological variable $R_9 = E_{3x3}/E_{SC}$ (energy sum of 3 × 3 crystals centered on the most energetic, divided by the energy of the supercluster). If $R_9 > 0.94$ the photon is assumed to be unconverted. In the barrel-endcap transition the efficiency of the photon reconstruction is suboptimal, thus the photon candidates are reconstructed within the ECAL fiducial region $|\eta| < 2.5$, excluding the range $1.44 < |\eta| < 1.57$, the aforementioned region. In Fig. 3.13 the photon identification efficiency is reported as a function of the transverse momentum.

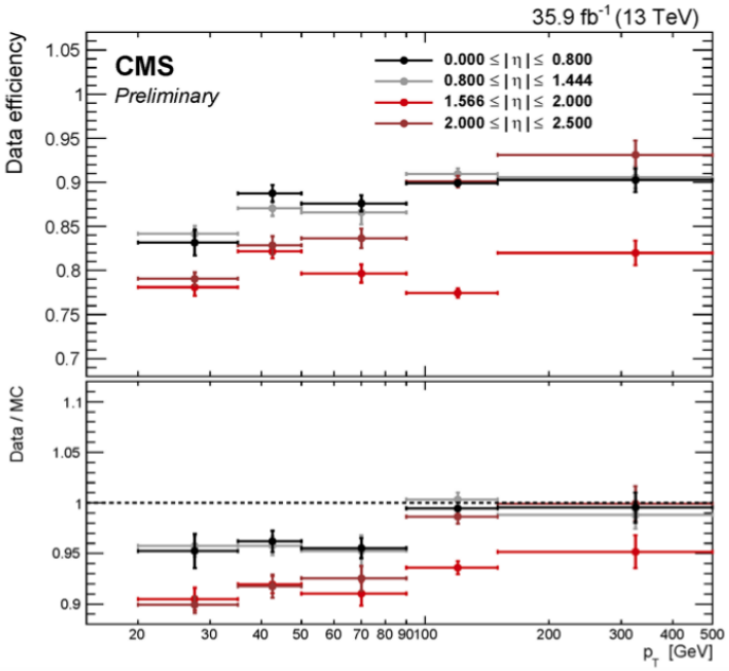

Figure 3.13: Photon ID efficiency as function of p_T.

3.16 Jet reconstruction

The production of color-charged particles like quarks and gluons in p-p collisions at LHC is abundant. The hadronization of partons in resulting collimated shower of particles generates a cluster of energy deposited in a localized areas of the HCAL, called jet. Jets are graphically represented by a cone (Fig. 3.14), which is coaxial to the original direction of the particle. The jet reconstruction consists in

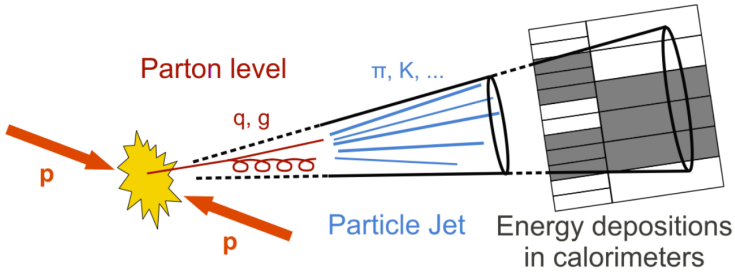

Figure 3.14: Pictorial representation of a jet and its constituents.

determining of the initial energy, momentum and, possibly, the nature of the parton produced in the original interaction, combining all the information from the tracker and the calorimetric system. Particle jets are reconstructed starting from PF particles and then using the anti-k_T clustering algorithm. The anti-k_T behaves as an idealised cone algorithm which imposes a distance parameter between PF candidates of R = 0.4 and rejects the charged hadrons that are associated to a PU secondary vertex. Jets must fulfil several requirements, such as having at least two PF constituents and more than 1% of their energy in either the ECAL or the HCAL. Jet momentum is determined as the vectorial sum of all particle momenta in the jet.

Analysis Strategy 4

The search for the decays of the Higgs boson $H \to \rho/\phi/K^{*0}\gamma$ is a tough challenge due to a variety of reasons. Firstly, it involves a hadronic decay channel, which is inherently difficult to trigger in a hadronic collider. Secondly, the branching ratio for this decay process is expected to be several orders of magnitude lower than the most common Higgs decays in the SM. These factors collectively make the detection and analysis of the $H \to \rho/\phi/K^{*0}\gamma$ decay mode a highly complex and demanding task in the field of high-energy physics. The analysis targets the Higgs boson production via gluon fusion, vector boson fusion and in association with a vector boson (Z, $W^{\pm}$). The production modes are depicted in Fig. 2.4. The final states of interest comprise of an isolated and energetic photon and meson pair with or without 2 VBF-tagging hadronic jets or in association with one or more additional leptons (μ, e). The meson considered here is a ρ, ϕ or K^{*0} with consequent decay in two charged particles.

The predicted branching ratios for the Higgs boson rare decay into a meson and photon are reported in Tab. 2.4 and Tab. 2.5. Given the constraints of the limited data collected and the impossibility to observe the SM direct process within the available dataset, the ultimate aim of this analysis is to establish an upper limit on the branching fractions. The ATLAS Collaboration has already conducted a research for these decay channels measuring observed upper limits (UL) at 95% confidence level (CL) for branching ratios of $\mathcal{B}(H \to \rho\gamma) = 10.4 \cdot 10^{-4}$, $\mathcal{B}(H \to \phi\gamma) = 5.0 \cdot 10^{-4}$ [26] in a 36 fb^{-1} dataset and $\mathcal{B}(H \to K^{*0}\gamma) = 1.2 \cdot 10^{-4}$ [27] in a 134 fb^{-1} dataset.

Prior to delving into the details of the various stages of the analysis, it is pertinent to provide some context regarding the timing and development of the analysis. Started in the early 2021, this project represents a concerted endeavor spanning approximately three years, involving two groups within

the CMS Collaboration: the Torino (University along with INFN) and the MIT groups. Each group targeted different Higgs boson production mechanisms. The gluon fusion analysis was undertaken by the Torino group, led by the author of this doctoral dissertation, who also was the contact person for the entire paper. Meanwhile, the MIT contingent focused on the VBF and VH analyses. Despite their distinct focus, both groups engaged in cooperative efforts across each category to ensure the analysis process was uniform and to combine the outcomes from all modes. This doctoral dissertation encapsulates the collective efforts of these two groups as conducted for this project.

4.1 Analysis overview

The strategy for reconstructing Higgs boson candidates involves the identification and characterization of a photon from energy clusters in the electromagnetic calorimeter, along with the identification of mesons through their decays into charged tracks, specifically $\rho \to \pi^+\pi^-$, $\phi \to K^+K^-$, and $K^{*0} \to K^\pm\pi^\mp$. Following a multistep selection procedure designed to highlight the topological characteristics of signal-like events while rejecting background, a fit to the invariant mass spectrum of the two tracks and the photon is performed to extract the number of signal events.

The following list gives a preliminary overview the selection procedure that will be described in detail in the following chapters:

- *HLT*: the high level trigger, employed during Run2 data taking, is the first step of the selection, consisting in a dedicated online selection which imposes thresholds on transverse momentum of nearby charged tracks and on transverse energy of a photon in coincidence.

- *preselection*: a more refined selection criteria, based on further requirements on transverse momentum, isolation parameter of the candidate meson and photon and invariant mass of the oppositely charged track pairs.

- *MVA-based selection*: a stricter selection criteria on specific variables as input of a Multivariate Analysis (MVA) designed to better distinguish signal from background and enhance the discriminating power of the analysis.

To differentiate among production modes, specific criteria are implemented at each selection step. These criteria are tailored to target the distinctive

characteristics of each mode and they are comprehensively outlined in the next chapters. The value of the branching ratios are estimated from the number of signal events extracted from the $m_{\mathcal{M}\gamma}$ spectrum fit. The value can be parametrized as following:

$$N_{\text{sig}} = \mathcal{L}_{\text{int}} \times \epsilon \times \sigma^{H}_{13\ \text{TeV}} \times \mathcal{B}(\mathcal{M} \to \text{trk}^{+}\text{trk}^{-}) \times \mathcal{B}(H \to \mathcal{M}\gamma) \tag{4.1}$$

where $\mathcal{L}_{int}$ is the integrated luminosity, ϵ is the total efficiency of the selection, trk stands for "track", $\mathcal{M}$ for "meson". Since no significant number of signal events over the background has been observed at the conclusion of this analysis, an upper limit to the value $\mathcal{B}(H \to \mathcal{M}\gamma)$ has been determined. The entire statistical procedure which has led to this conclusion will be described in the following chapters.

4.2 Data sample

During the 2018 data taking period, the CMS experiment recorded in proton-proton collisions at $\sqrt{s}$ =13 TeV a total integrated luminosity of $\mathcal{L}_{int}$ = 63.67 fb^{-1} (Fig. 4.1). The data sample used to perform this analysis is lower, as a dedicated trigger for this analysis was not operational during the whole year. The dedicated trigger started to operate when a part of the total integrated luminosity has already been delivered, thus the available data sample corresponds to $\mathcal{L}_{int}$ = 39.54 fb^{-1}. This trigger targets mostly the gluon fusion mechanism, therefore this dataset is the most contributing to the final result of this analysis. However, several triggers have been considered to increase the statistics in the other less sensitive production modes (VBF and VH), resulting in a dataset up to 137 fb^{-1}. The specific characteristics of the triggers employed for each category will be delineated in the next chapters.

4.3 Monte Carlo simulation

Samples of simulated Higgs boson events, produced via the gluon-gluon fusion ggH, VBF, $t\bar{t}H$, WH, and ZH modes, are generated at next-to-leading order (NLO) in quantum chromodynamics (QCD) using POWHEG 2.0, with improved MiNLO accuracy where available [52, 53, 54, 55, 56, 57]. Background estimation relies solely on data. However, for data-simulation comparisons and the evaluation of corrections that account for differences between the two, simulated samples are

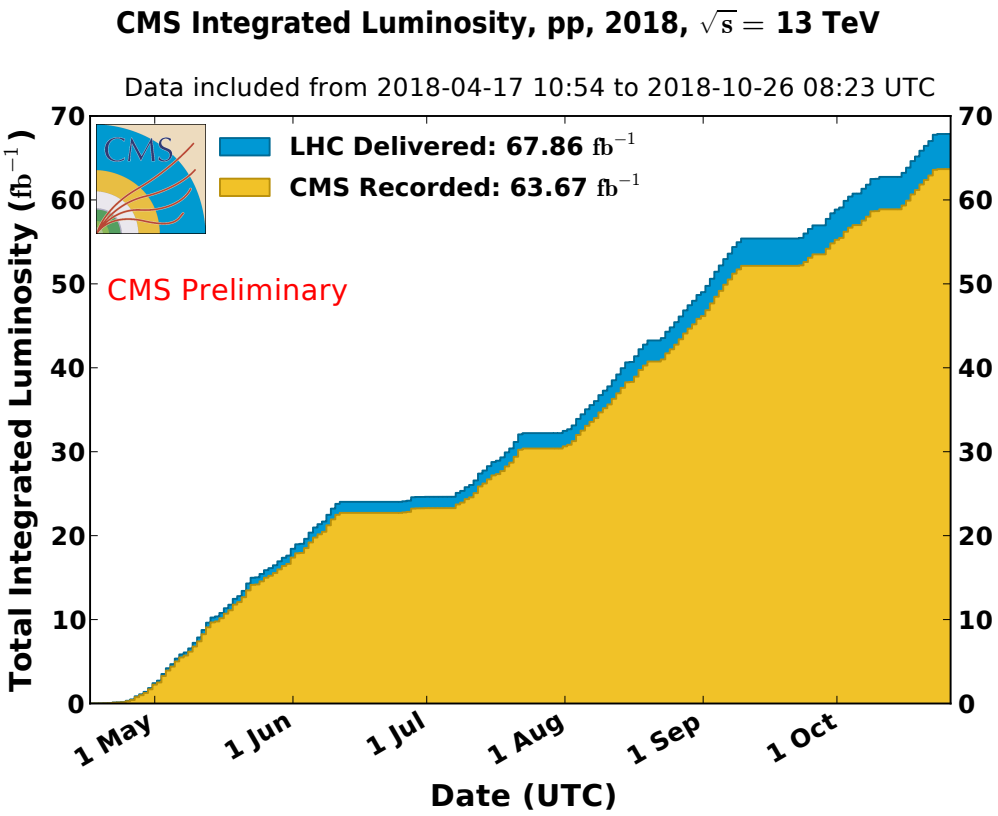

Figure 4.1: Cumulative measured luminosity versus day delivered by LHC and recorded by CMS during the 2018 data taking period in proton-proton collisions at $\sqrt{s}$ =13 TeV.

used. The related SM processes are: γ, γ-jets, dijet, $W \to \ell\nu$, and Drell–Yan (DY) $Z \to \ell\ell$ production associated to jets, WW, ZZ as well as $t\bar{t}H$, $WH\gamma$ and $ZH\gamma$ production. These samples are generated either at NLO using POWHEG or at leading order (LO) using MADGRAPH5 aMC@NLO 2.6.5 [58]. The NNPDF 3.1 parton distribution functions (PDFs) [59] at next-to-next-to-leading order are used for all samples. All generated samples are interfaced with PYTHIA 8.212 [60] to model parton showering and hadronization. The description of the underlying event is provided by the CP5 tune [61]. In the signal samples the decays $H \to \rho\gamma$, $H \to \phi\gamma$, or $H \to K^{*0}\gamma$ are also modelled using PYTHIA. As the Higgs boson is a scalar particle, angular momentum conservation enforces fully transverse spin alignment of the outgoing mesons, while PYTHIA simulates unpolarised decay products. Signal events are therefore weighted by a factor proportional to $\sin^2\theta$, where θ is the angle between the direction of the positive kaon or pion in the meson rest frame and the meson flight direction in the

laboratory, at generation level. More details about this reweighting are reported in Sec. 8.3.

Additional PU interactions, generated with PYTHIA, are added to all simulated events in accordance with the expected PU distribution. All generated events are passed through a GEANT4-based [62] simulation of the CMS detector before being reconstructed with the same version of the CMS event reconstruction software as used for data. Detector conditions corresponding to the different data-taking periods in years 2016, 2017 and 2018 are simulated separately.

The main contributing backgrounds are those including jets with a high total transverse momentum and photons with high transverse energy. In the following list, these are the main background contributions to the final state:

- dijet: this kind of background samples consists in events containing two jets, in which a jet is misidentified as a photon, resulting for instance from the electromagnetic decay of an energetic π^0 produced during hadronization.
- γ-jet: processes with a photon and a jet with high transverse momentum

The entire list of the MC background samples is reported in Tab. 4.1, with the corresponding cross section.

For each MC sample, the number of events produced is fixed and different from sample to sample. Therefore, they can be compared only through an appropriate normalization. The normalization factor is hereafter referred to as $\mathcal{W}$, defined as

$$\mathcal{W} = \frac{\sigma \cdot \mathcal{B} \cdot \mathcal{L}_{\text{int}} \cdot W}{N_{\text{events}}} \tag{4.2}$$

where N_{events} is the total number of events generated for each MC background sample and σ is the cross section of the process, while W is a factor comprehensive of several corrections applied to simulation samples and described in Chap. 8.

MC background samples	cross section (pb)
$t\bar{t} \rightarrow W^+\bar{b}W^-b \rightarrow 4qb\bar{b}$	$3.78 \cdot 10^2$
$t\bar{t} \rightarrow W^+\bar{b}W^-b \rightarrow 2q\ell\nu b\bar{b}$	$3.65 \cdot 10^2$
$t\bar{t} \rightarrow 2\ell 2\nu$	88.29
Drell-Yan process with $10 < m_{\ell\ell} < 50$ GeV	$1.88 \cdot 10^4$
Drell-Yan process with $m_{\ell\ell} > 50$ GeV	$2.08 \cdot 10^3$
WW	12.18
WZ	27.60
$W\gamma \rightarrow jj\gamma$	8.64
$Z\gamma \rightarrow jj\gamma$	4.14
Di-jet and multijet processes	$3.17 \cdot 10^7$
γ-jets	$1.52 \cdot 10^4$
γ-jets with $20 < p_T^{jet} < 40$ GeV and $m_{\gamma\gamma} > 80$ GeV	$2.32 \cdot 10^2$
γ-jets with $p_T^{jet} > 20$ GeV and $40 < m_{\gamma\gamma} < 80$ GeV	$3.16 \cdot 10^3$
γ-jets with $p_T^{jet} > 40$ GeV and $m_{\gamma\gamma} > 80$ GeV	$8.74 \cdot 10^2$
W-jet with $W \rightarrow \ell\nu$	$6.15 \cdot 10^4$

Table 4.1: MC background samples used for this analysis with corresponding cross sections in pb.

Selection Procedure 5

In this chapter, the selection procedure is described in depth. The entirety of the procedure is broken down into sections based on the categories and reconstructed objects. The selection criteria have been decided using a *blind analysis* approach. The signal region in data was not looked at until all the selection criteria were decided, not to bias this selection. The signal region was defined as $120 < m_{\text{ditrk}\gamma} < 130$ GeV, where $m_{\text{ditrk}\gamma}$ is the invariant mass of the pair of tracks and the photon, namely the invariant mass of the Higgs candidate. The complementary regions ($100 < m_{\text{ditrk}\gamma} < 120$ GeV and $130 < m_{\text{ditrk}\gamma} < 160$ GeV) are called $m_{\text{ditrk}\gamma}$ sidebands. In order to estimate the shape of signal and background models in the signal region, we used the signal MC sample for the former, and the sidebands from data for the latter.

5.1 Trigger selection

This section details the triggers employed for each category, each having distinct features that necessitate a specific online selection for every mode.

5.1.1 Gluon fusion trigger

As explained in Chap. 3, the trigger system at LHC reduces the huge amount of recorded data arising from the high bunch crossing frequency and the number of particles created in each interaction. The search for Higgs decay to a meson and a photon at CMS cannot be performed by looking for the photon or the meson only. Indeed, the CMS standard HLT energy thresholds for single photon or jets are too high (i. e. $E_T^{\gamma} > 120$ GeV, $p_T^{\text{jet}} > 200$ GeV) for 2018 running conditions at an instantaneous luminosity of $1.8 \cdot 10^{34}$ cm^{-2} s^{-1}. Therefore, the trigger

selection used for this category exploits the full final state of the studied channel, whose features allows to significantly reduce the recorded event rate.

The trigger tailored for the gluon fusion analysis selects a photon with $E_T^\gamma > 35$ GeV and a hadronic τ-jet with $p_T^{\text{jet}} > 35$ GeV. The event rate recorded by this trigger was about 8 Hz at maximum instantaneous luminosity in 2018. A trigger developed to select a jet resulting from a τ decay in few close-by tracks can be used, as first approximation, for a jet coming from a ρ, ϕ or K^{*0} decay in two pions, kaons or a combination of them. Table 5.1 reports the photon trigger selection, which consists in cuts on H/E parameter, i.e. the fraction of the HCAL cluster energy and ECAL energy cluster, on transverse energy, R_9 parameter (described in Sec. 3.15) and PF cluster isolation ("iso" in the table) for both ECAL and HCAL, which represents the energy collected around the cluster after subtracting the energy collected within the cluster in a $\Delta R < 0.4$.

Photon sequence	
H/E cut	< 0.1
E_T^γ	> 35 GeV
R_9	> 0.9
ECAL PF cluster iso	< 6 GeV$+1.2\% \cdot E_T^\gamma$
HCAL PF cluster iso	< 6 GeV$+1.2\% \cdot E_T^\gamma$
$\lvert\eta_\gamma\rvert$	< 2.1

Table 5.1: Photon selection sequence applied by the trigger.

Table 5.2 reports the τ selection criteria of the this trigger, which consists in cuts on the minimum size of the cone containing the τ-jet and the photon, $\Delta R_{\text{jet}\gamma} > 0.3$, and on the transverse momentum of the jet. Furthermore, jets must contain at least two charged tracks.

5.1.2 Vector boson fusion triggers

The VBF triggers select a photon with $p_T^\gamma > 75$ GeV in the barrel detector and forward jets with high m_{jj} and large $|\Delta\eta_{jj}|$.
The trigger paths were prescaled during 2016 providing an effective luminosity

τ-jet selection	
$\Delta R_{\text{jet},\gamma}$	> 0.3
n. tracks inside the jet	> 2
p_T^{jet}	> 35 GeV
$\lvert\eta_{\text{jet}}\rvert$	< 2.1

Table 5.2: τ-jet selection sequence applied by the trigger.

of 28.2 fb^{-1}. Trigger prescaling is a technique used to manage the data acquisition rate when the number of events meeting the trigger criteria exceeds the processing or storage capabilities of the detector system. Prescaling a trigger consists in adjusting the frequency at which certain triggers are allowed to record events.
The VBF trigger paths in 2017 were enabled only in October, close to the end of data taking and the data collected with this trigger correspond to an integrated luminosity of 7.7 fb^{-1}. In 2018, the trigger requirement was set to a higher threshold on the m_{jj} and events with lower values of m_{jj} are recovered with the custom trigger outlined in Sec. 5.1.1. Basically, for the 2016 and 2017 eras the considered triggers select a high energy photon with $E_T^\gamma > 75$ GeV and R_9, H/E and isolation requirements or a very high photon with $E_T^\gamma > 175$ or 200 GeV (depending on the year). The same triggers have been used for 2018 era, with the addition of a high dijet invariant mass cut at 300 GeV.

5.1.3 Associated production triggers

The presence of a vector boson in the VH production mode allows to exploit leptonic triggers. The trigger requires the presence of at least one isolated muon (electron) with $p_T > 24(27)$ GeV in the 2016 data-taking period, $p_T^\mu > 27(35)$ GeV during 2017 and $p_T^\mu > 27(32)$ GeV during 2018.

5.2 Preselection

The purpose of the preselection step is to select events based on the basic topological properties of signal-like events and to reject most background events. Data collected by the triggers are processed offline, using several criteria to identify the $H \to \mathcal{M}\gamma$ candidates. The analysis primarily relies on photons and

tracks in order to extract the final state signature of exclusive hadronic decays, but it also makes use of other physics objects such as additional leptons (muons or electrons), hadronic jets, to tag the different Higgs boson production modes as well as to suppress specific backgrounds.

In this analysis, events are categorized in order to construct high-purity regions. Categorization allows for the optimization of the analysis sensitivity by adapting the selection criteria to the specific features of different production modes or based on the outcome of a MVA classifier. Such categories are preliminarily described below in order of decreasing signal purity and increasing expected signal yield. More details about the differences between the categories are highlighted in the next sections of this chapter describing the selection criteria for each object. Events falling into a certain category are removed from lower-purity ones, thus making categories exclusive.

- The *VH category* targets associated production of a Higgs and a heavy vector boson and also captures $t\bar{t}H$ events with leptons in the final state. In the $W \to \ell\nu$ channel, the presence of a muon or an electron is required while a pair of muons or electrons in the $Z \to \ell\ell$ channel. In these categories muons and electrons must satisfy p_T, η, isolation and identification criteria. Events with two opposite-sign and same-flavor charged leptons are consistent with a Z boson decay if they satisfy $|M_{\ell\ell} - M_Z| < 15$ GeV. In the VH category, photons are retained if they satisfy specific criteria on transverse momentum, presudorapidity and identification. For meson candidates it is requested that they pass transverse momentum and isolation cuts. In addition, in the single-muon final state, it is required that $\Delta R(\mu, M) > 0.5$. In the single-electron final state, events with electron-photon pairs consistent with the Z boson decays are vetoed specifying $|M_{e\gamma} - M_Z| > 10$ GeV. In the dilepton final state an additional requirement is imposed on the invariant mass of the dilepton-γ system, $M_{\ell\ell\gamma} > 96$ GeV.

- The *high-p_T^γ VBF category* (VBF) targets high-energy VBF events. In this category, photons are retained if they have $p_T^\gamma > 75$ GeV, with further requirements on pseudorapidity and identification. With respect to the VH category, meson candidates are retained if they pass a lower p_T threshold and a tigher isolation cut. In addition, two jets not overlapping with the $H \to M\gamma$ signal candidates are required, which must satisfy specific criteria described in Sec. 5.2.4.

- The *low-p_T^γ VBF category* (VBFlow) targets remaining VBF events. Online selection is based on a trigger stream which was only active in 2018 and was expressly designed for the present analysis. In this category, photons are retained if they have $40 < p_T^\gamma < 75$ GeV, and further cuts are applied on η and isolation. Meson candidates and the two additional jets have same requirements of the high-p_T^γ VBF category.
- The *ggH category* contains all remaining candidate events and has the largest search sensitivity. After overlap with other categories is removed, photons and mesons are retained if they pass requirements on the same variables of the other categories.

In addition to this categorization, each event category employing a MVA-based classification, i.e. ggH, VBFlow and VBF, is further split in two sub-categories of different purity, whose MVA-score thresholds are carefully chosen to optimize the sensitivity of the analysis. Considering the MVA-based classification, described in Chap. 7, the categorization results in a total of seven distinct categories per channel.

5.2.1 Primary vertex

Events must contain at least one primary vertex, considered as the vertex of the hard interaction. At least four tracks must be associated to the selected primary vertex. The longitudinal and radial distances of the vertex from the center of the detector must be smaller than 24 cm and 2 cm, respectively. For events with more than one selected vertex, the primary vertex (PV) is taken to be the vertex corresponding to the hardest scattering in the event, evaluated using tracking information alone [63].

5.2.2 Leptons

The isolated and high energetic muons and electrons are used to identify the W and Z bosons produced in association to the Higgs boson. Additional leptons are also vetoed in the event in order to suppress the V+jets and top pair background in the hadronic categories or multileptons final states.

Muons are considered if above a minimum p_T threshold. The muon track should be within a specific distance from the PV along the beam axis and in the transverse plane. Muons originating from a W or Z boson decay are expected to

produce a track that is isolated from those of the other particles generated in the pp collision. Therefore, A relative isolation variable is defined as

$$I^{\mu}_{\text{rel}} = \frac{\sum_{\text{charged}} p_T + \max\left(0, \sum_{\text{neutral}} p_T - 0.5 \sum_{\text{charged}} p_T^{\text{PU}}\right)}{p_T^{\mu}}, \tag{5.1}$$

where $\sum_{\text{charged}} p_T$ refers to the scalar sum of the transverse momenta of all charged particles and $\sum_{\text{neutral}} p_T$ is the sum of the p_T of neutral hadrons and photons. These two sums are calculated within a cone of radius $\Delta R = 0.4$ around the direction of the muon and the p_T of the muon is excluded from these sums. To reduce the effects from PU, charged particles are only considered in the isolation sum if they are associated with the PV. The term $0.5 \sum_{\text{charged}} p_T^{\text{PU}}$ estimates the contributions from neutral particles.

Electrons are reconstructed by combining clusters of energy deposits in the ECAL with hits in the tracker [64]. To reduce contamination from particles incorrectly identified as electrons, reconstructed electrons are required to pass a multivariate electron identification discriminant. This discriminant [65] combines information about the quality of the tracks, the shower shape, kinematic quantities, and hadronic activity in the vicinity of the reconstructed electron.

A *conversion veto* is applied to electrons, an algorithm that rejects electrons coming from photon conversions in the tracker, which should instead be reconstructed as part of the photon. The electrons and muons identification, isolation criteria and kinematic requirements are summarized in Tabs. 5.3 and 5.4.

	WH	ZH	veto
p_T (GeV)	> 20	$>$ (20,10)	> 10
$\lvert\eta_\mu\rvert$	< 2.4	< 2.4	< 2.4
ID	tight	medium	loose
I^{μ}_{rel}	< 0.15	< 0.25	< 0.25
d_{xy}(cm)	0.05	0.05	0.05
d_z(cm)	0.10	0.10	0.10

Table 5.3: Muon selection used in the analysis.

5.2.3 Photons

Photon candidates are reconstructed as SuperClusters in the electromagnetic calorimeter. A *pixel veto* ensures that the candidate photon has not left any hit in

	WH	ZH	veto
p_T (GeV)	> 30	> (20,10)	> 10
$\|\eta_e\|$	< 2.5	< 2.5	< 2.5
ID	tight	medium	loose
d_{xy}(cm)	0.2	0.2	0.2
d_z(cm)	0.5	0.5	0.5
Conversion veto	Applied	Applied	Applied

Table 5.4: Electron selection used in the analysis.

the pixel tracker in the extrapolated trajectory, avoiding contamination between photons and prompt electrons. A conversion veto, described in Sec. 5.2.2, is also applied in some categories. Each photon must pass a multivariate selector for identification (mvaID) with working point with 80% (WP80) or 90% (WP90) efficiencies depending on the category. The mvaID outcome is based on an isolation variable measured both in the calorimeters and in the tracking devices as well as on the shower shape and extension. In the ggH, VBFlow and VBF categories, additional photons with loose requirements ($E_T^\gamma > 20$ GeV and WP90 version of the mvaID) are vetoed to reduce the diphoton potential contribution.

Table 5.5 summarizes photon selection criteria. For each event, among all of

	VH	ggH	VBFlow	VBF
E_T^γ (GeV)	> 40	> 38	$38 < E_T^\gamma < 75$	> 75
$\|\eta^\gamma\|$	< 2.5	< 2.1	< 2.1	<1.4
mvaID	WP90	WP80	WP80	WP90
pixel veto	yes	no	no	no
conversion veto	no	yes	yes	yes

Table 5.5: Photon selection used in the analysis.

those photons above the aforementioned thresholds, the one with the highest transverse energy is promoted to *best photon of the event*.

5.2.4 Jets

Since the mesons from the Higgs-boson decays have a large momentum, their secondary decay products are expected to be very collimated in the laboratory

jet ID	
n. of particle within the jet	> 1
$E_{\text{had}^0}/E_{\text{tot}}$	< 0.8
$E_{\text{em}^0}/E_{\text{tot}}$ (photon-veto)	< 0.8
$E_{\text{had}^\pm}/E_{\text{tot}}$	> 0
$E_{\text{em}^\pm}/E_{\text{tot}}$	< 0.8
E_{μ}/E_{tot}	< 0.8
charged hadron multiplicity	> 0

Table 5.6: Jet ID criteria. Cuts on energy fractions avoid to select jets with a predominant amount of energy from charged or neutral hadrons ($E_{\text{had}^\pm}$ and E_{had^0} respectively), from charged or neutral electromagnetic processes ($E_{\text{em}^\pm}$ and E_{em^0} respectively) and from muons (E_{μ}).

frame, hence their signature can be identified as a jet by clustering algorithms. As a consequence, jets are used to reduce track combinatorial in the low-purity event category targeting ggH production. Jets are reconstructed from particle-flow candidates using the anti-k_T clustering algorithm with a radius parameter of $R = 0.4$ and required to pass basic identification criteria. Since all the PF candidates are used as input to the clustering algorithm, medium identification criteria are applied to the jets, in order to distinguish them from common objects. The ID criteria for jets are provided centrally by CMS and reported in Tab. 5.6. To mitigate the effect of PU, charged hadrons that do not arise from the PV are removed. Tight PU-rejection criteria are used to reduce the contamination of jets with $p_T^{\text{jet}} < 50$ GeV initiated by PU interactions. Jets are corrected for the response inside the detector, differentially in $|\eta|$, for the pileup contributions, and, for data only, the residual residual difference observed between data and simulation.

In addition, the VBF production mode is characterized by the presence of jets in the final state. Two jets not overlapping with the $H \to \mathcal{M}\gamma$ signal candidates are required in both VBF categories, which must satisfy $p_T^{\text{jet}} > 40$ GeV, $m_{\text{jj}} > 400$ GeV and $|\Delta\eta_{\text{jj}}| > 3$.

5.2.5 Meson

The ρ, ϕ and K^{*0} mesons decay products are reconstructed using charged particle tracks measured in the tracker. The ρ and ϕ are reconstructed from its decay

into $\pi^+\pi^-$ or K^+K^- while the K^{*0} is reconstructed from the decay $K^\pm\pi^\mp$.

In the ggH category, the strategy to reconstruct the products of the meson decay consists in exploiting those jets of the event that pass ID and kinematic requirements described in Sec. 5.2.4 adding other requirements: $p_T^{\text{jet}} > 40$ GeV, $|\eta_{\text{jet}}| < 2.1$ and $m_{\text{jet}\gamma} > 100$ GeV. The procedure is to select among the constituents of these jets a charged pair whose properties best match with ones of a pair of charged tracks coming from the meson. As a consequence, jets are used to reduce track combinatorial in the low-purity event category targeting ggH production. The other categories selects the tracks in the full combinatorics. The tracks are required to originate from the PV and to pass *high-purity* reconstruction requirements. These requirements are based on the number of tracker layers with hits, the track fit quality, and the values of the impact parameters relative to their uncertainties. The algorithm is described in more detail in Ref. [66]. A ρ, ϕ or K^{*0} meson candidate, is a pair of oppositely charged tracks, with $p_T > 5$ GeV and $|\eta| < 2.5$ and where, in both cases, at least one of the tracks must have $p_T > 20$ GeV. The rapidity of the meson is restricted to match trigger requirements.

A dedicated isolation of the candidate based on charged tracks is determined from the meson momentum and other tracks in a cone of radius $\Delta R = 0.3$ around the direction of the di-track system as follows:

$$\text{iso}_{\text{ch}}^{\text{ditrk}} = \frac{p_T^{\text{ditrk}}}{p_T^{\text{ditrk}} + \sum_{\text{trk}} |p_T^{\text{trk}}|} \tag{5.2}$$

Only tracks with $p_T > 0.9$ GeV associated with the same meson vertex are used, excluding the candidates defining the meson. The isolation is required to be greater than 0.9 (0.8 for VH production modes). Table 5.7 summarizes the meson candidate selection used.

It is required that the track-pair invariant mass, under the appropriate charged-pion or charged-kaon mass hypothesis for the tracks, is consistent with the ρ, ϕ or K^{*0} meson mass. The experimental resolution ranges from approximately 3 MeV for m_{KK} to 8 MeV for $m_{\pi\pi}$. Events are selected if the invariant mass of ditrack system in one of the hypotheses is within $0.62 < m_{\pi\pi} < 0.92$ GeV, $1.008 < m_{KK} < 1.032$ GeV, or $0.84 < m_{K\pi} < 0.94$ GeV. In the last case, if both the $K^+\pi^-$ and the $K^-\pi^+$ combinations fall in the mass interval, the one with the invariant mass closest to the nominal K^{*0} mass is chosen. Moreover, candidates where m_{KK} is consistent with the ϕ meson mass and have a transverse momentum

	ϕ (K^+K^-)	ρ ($\pi^+\pi^-$)	K^{0*} ($K^\pm\pi^\mp$)
mass	1.02 ± 0.01 (~ 3 Γ)	0.77 ± 0.15 (~ 1 Γ)	0.89 ± 0.05 (~ 1 Γ)
p_T (GeV)	> 38(30 for VBF)	> 38 (30 for VBF)	> 38 (30 for VBF)
p_T^{leadTrk} (GeV)	> 20	> 20	> 20
$p_T^{\text{subLeadTrk}}$ (GeV)	> 15	> 5	> 5
p_T^{π} (GeV)	-	-	> 5
p_T^{K} (GeV)	-	-	> 20
$\text{iso}_{\text{ch}}^{\text{ditrk}}$	> 0.9 (0.8 for VH)	> 0.9 (0.8 for VH)	> 0.9 (0.8 for VH)

Table 5.7: Meson selection.

higher than a ρ candidate in the same event are rejected from the $\rho\gamma$ channel, and viceversa.

Among all those pairs above these thresholds, the one with the highest transverse momentum is promoted to *best pair of the event*. In ggH category, the jet containing the best pair is promoted to *best jet of the event*.

Background estimation 6

An accurate modeling of the background is essential to perform a more refined selection based on a multivariate analysis (MVA). VBF category uses background samples described in Sec. 4.3. The lack of statistics in the VH category doesn't allow to perform a multivariate analysis and further reduce the number of events in the invariant mass spectrum. Since MC background samples do not adequately describe the data behaviour in the gluon fusion category, a fully data driven background estimation is used in this case. For all the decay channels, the background is estimated by data events in the sidebands of the meson invariant mass distribution, exploiting the narrow peaks centered on the resonance mass of the mesons. The sidebands range has been defined aiming to the best agreement between data and background estimation. In Tab. 6.1 the sidebands definition is reported.

$\rho\gamma$ **sidebands**	
Left sideband	0.55 GeV $< m_{\pi\pi} <$ 0.62 GeV
Right sideband	0.92 GeV $< m_{\pi\pi} <$ 1.00 GeV

$\phi\gamma$ **sidebands**	
Left sideband	1.000 GeV $< m_{KK} <$ 1.008 GeV
Right sideband	1.032 GeV $< m_{KK} <$ 1.040 GeV

$K^{*0}\gamma$ **sidebands**	
Left sideband	0.800 GeV $< m_{K\pi} <$ 0.842 GeV
Right sideband	0.942 GeV $< m_{K\pi} <$ 1.000 GeV

Table 6.1: Sidebands range definition for background estimation.

Figure 6.1 shows the invariant mass distribution of the MC signal samples of simulated $H \to \rho\gamma$, $H \to \phi\gamma$ and $H \to K^{*0}\gamma$ events. Signal regions (SR) and

control regions (CR) are also reported. The masses of candidate mesons are calculated assuming the charged particle mass equals to the pion or kaon mass, respectively.

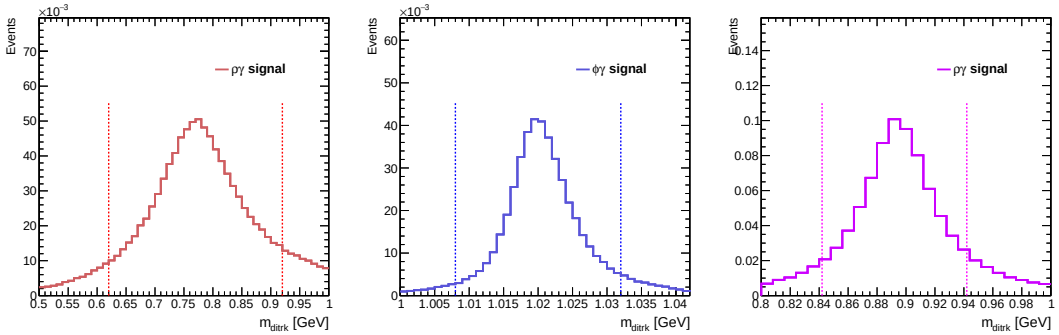

Figure 6.1: Invariant mass distribution of the for the two channels. The dashed lines define the sidebands (CR) and the SR.

6.1 Preselection distributions

In the following plots, from Fig.6.2 to Fig.6.10, the MC and data after preselection are shown for the gluon fusion category, which is the most sensitive category of this search. Some interesting distributions shown are:

- $\mathrm{iso}_{\mathrm{ch}}^{\mathrm{trk}_1}$: relative isolation of the first track candidate from charged particles, determined in a cone of radius $\Delta R = 0.3$ around the direction of the first track, and defined as

$$\mathrm{iso}_{\mathrm{ch}}^{\mathrm{trk}_1} = \frac{p_T^{\mathrm{trk}_1}}{\sum p_T^{\mathrm{ch}} + p_T^{\mathrm{trk}_1}} \tag{6.1}$$

- $p_T^{\mathrm{ditrk}}/m_{\mathrm{ditrk}\gamma}$: transverse momentum of the best pair of the event divided by the invariant mass of the best pair and the photon;

- $E_T^{\gamma}/m_{\mathrm{ditrk}\gamma}$: transverse energy of the best photon of the event divided by the invariant mass of the best pair and the photon;

- $\mathrm{iso}_{\mathrm{ditrk}}^{\mathrm{neu}}$: relative isolation of the best pair from neutral particles, in a cone of radius $\Delta R = 0.3$ around the direction of the di-track system and defined as

$$\mathrm{iso}_{\mathrm{ditrk}}^{\mathrm{neu}} = \frac{p_T^{\mathrm{ditrk}}}{\sum p_T^{\mathrm{neu}} + p_T^{\mathrm{ditrk}}}. \tag{6.2}$$

The first three variables are used as input of the MVA classifier while the last one is employed for a further selection after the MVA-based cut. The application of these variables is discussed comprehensively in Chap. 7.

Data events falling in the sidebands of the meson invariant mass are used as background estimation, which is normalized to the number of data events in the signal region and represented by the colored area in the plots. Gluon fusion MC events are also reported in figures to show the expected signal distribution. The signal yield is magnified of a factor greater then 1 to make the signal visible in the plots. Furthermore, in the gluon fusion category the entire selection is also applied to a VBF MC sample to incorporate the contribution of those events that are not rejected by the VBF veto. Those VBF MC events surviving after the selection skimming are reported in figures. In Fig. 6.11, the invariant mass spectrum $m_{\mathrm{ditrk}\gamma}$ is shown blinded in the region $115 < m_{\mathrm{ditrk}\gamma} < 135$ GeV centered on the Higgs rest mass.

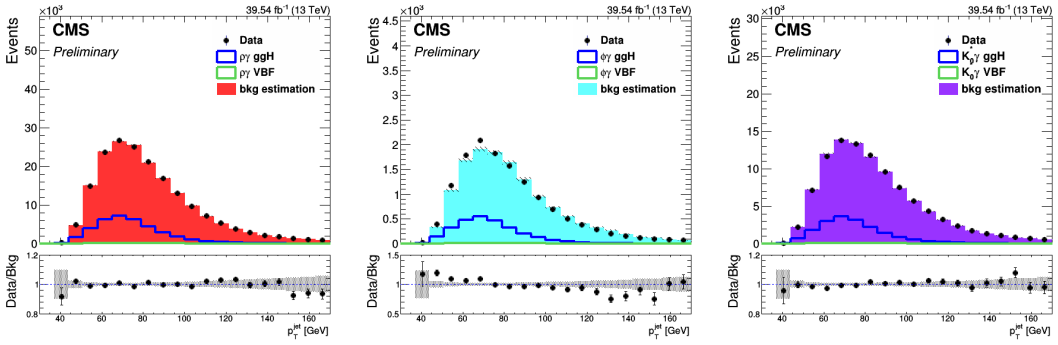

Figure 6.2: Transverse momentum distribution of the jet containing the best pair of the event. Red, azure and purple areas, corresponding to the ρ, ϕ, K^{*0} invariant mass sidebands, respectively, are normalized to areas under data events in the SR (black dots).

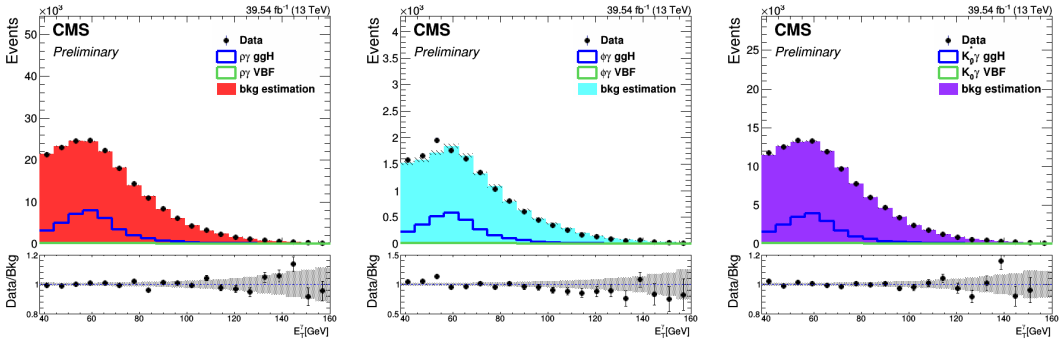

Figure 6.3: Photon transverse energy distribution.

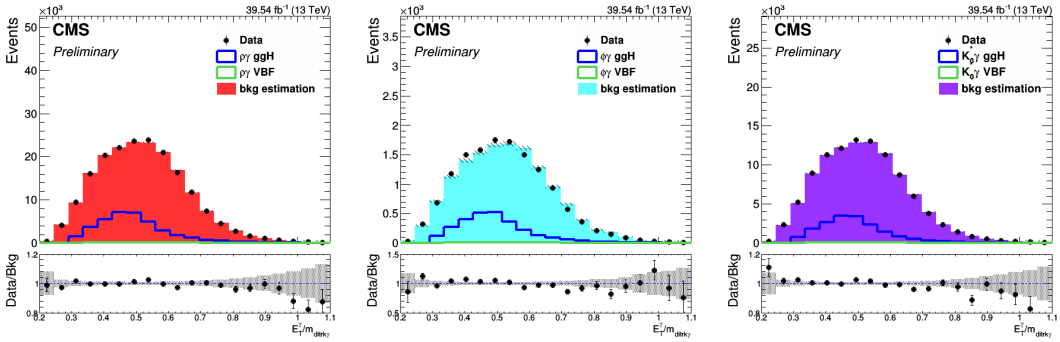

Figure 6.4: Photon transverse energy distribution divided by the invariant mass of the Higgs candidate.

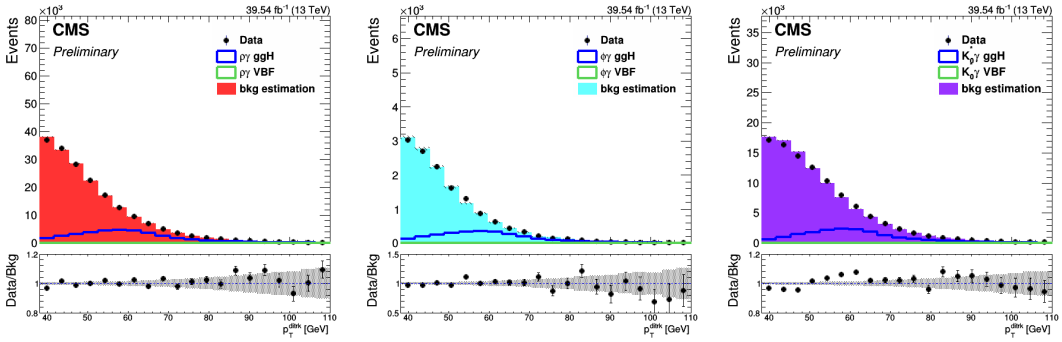

Figure 6.5: Transverse momentum distribution of the best pair of the event.

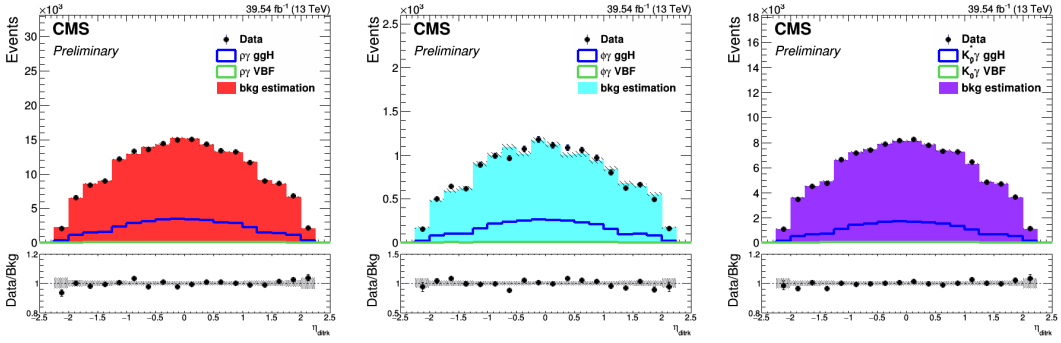

Figure 6.6: Pseudorapidity distribution of the best pair of the event.

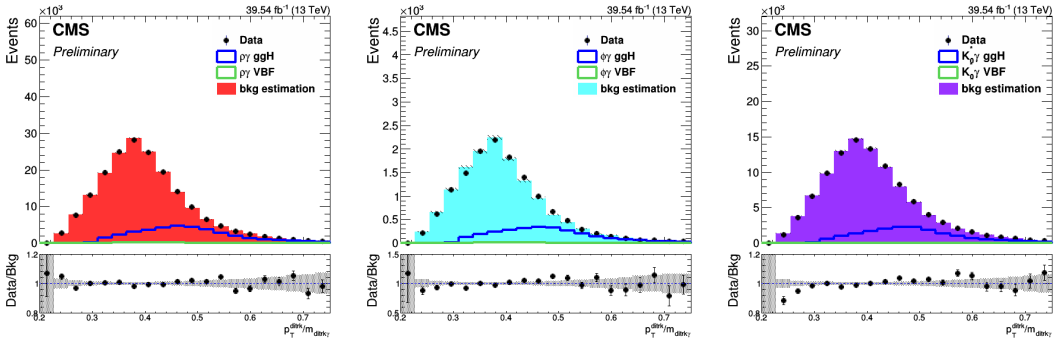

Figure 6.7: Transverse momentum distribution of the best pair of the event divided by the invariant mass of the Higgs candidate.

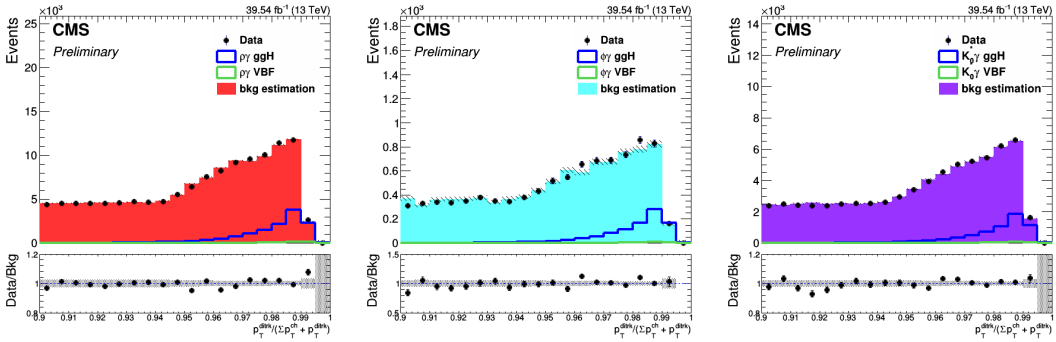

Figure 6.8: Relative isolation from charged particles of the best pair of the event.

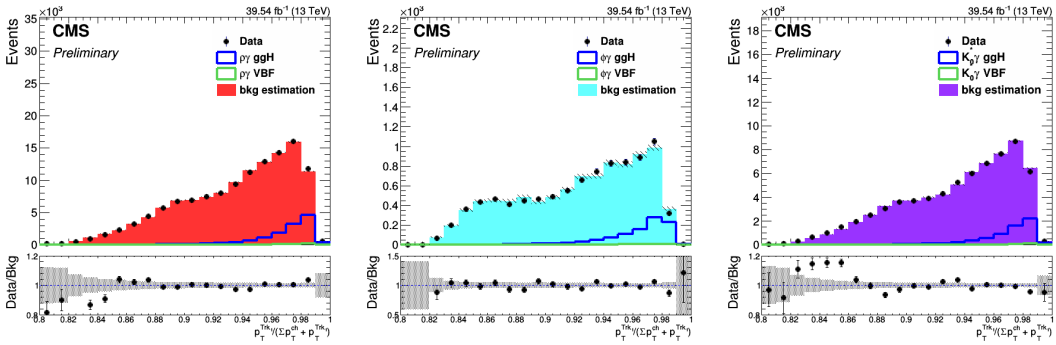

Figure 6.9: Relative isolation from charged particles of the leading track of the best pair.

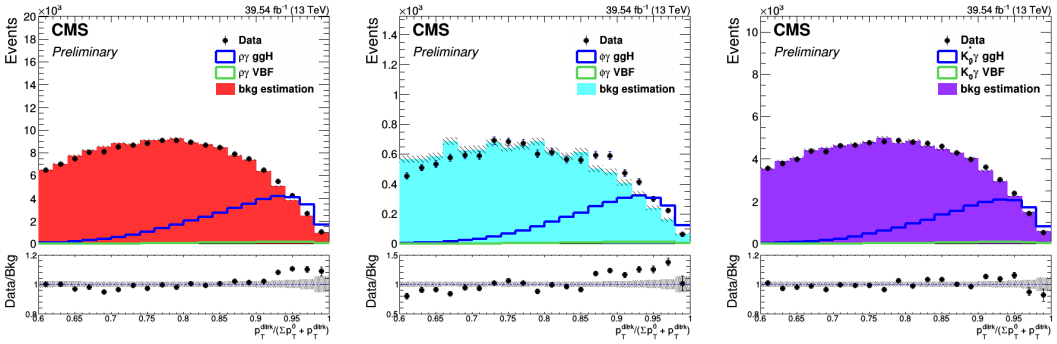

Figure 6.10: Relative isolation from neutral particles of the best pair of the event.

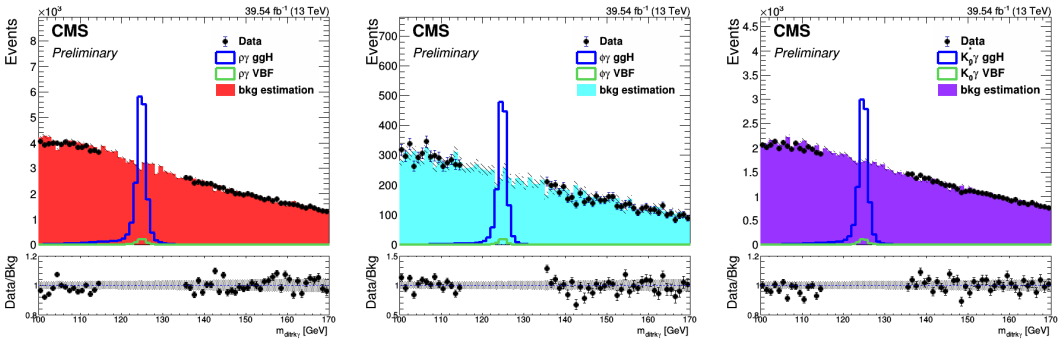

Figure 6.11: Invariant mass distribution of the ditrack and the photon.

Multivariate analysis 7

The selection described until here involves minimal thresholds on the kinematic variables of the final states investigated by this note. Therefore, a further event selection is required to enhance background and signal discrimination. This is performed through a multivariate analysis technique, namely a boosted decision tree (BDT) [67]. The decision tree is able to split the phase space into a large number of hypercubes, each of which is identified as either *signal-like* or *background-like*. The signal MC and data driven background estimation from the meson invariant mass sidebands defined in Chap. 6 are used as input samples of the MVA. In this analysis, a BDT classifier based on the root library TMVA [68] is trained using half of the signal and background events, and validated through the other half. The BDT used in this analysis exploits the Gradient Boost algorithm [69], which takes as input several variables that capture the distinctive kinematic features of the signal and the background. In addition to the boosting method, a number of other configuration options is available to set up the BDT classifier. In particular, in this analysis the following parameters are used:

- Number of grid points in the variable range used to find the optimal cutoff in node splitting: 20;
- Maximum depth of the decision tree: 3. A low value for this parameter, which indicates the maximum number of secondary nodes per tree, helps reducing the probability of overtraining (see the end of this section);
- Minimum percentage of training events required in a leaf node before interrupting the splitting: 2.5 %. If this number is too large, detailed features in the parameter space are hard to be modeled. If it is too small, the risk to overtrain rises and boosting proved to be less effective. This

parameter may implicitly set the maximum depth of the decision tree in case a node ends up containing less than 2.5 % of training events before 3 splittings;

- Number of trees in the "forest" (i.e., number of trees generated in the boosting procedure): 600.

Several values and combinations of these configuration parameters were tested. The ones chosen have proved to provide a good separation between signal and background distributions in the BDT discriminant, and a generally better signal efficiency for a given background rejection efficiency with respect to the other configurations tested. At the same time, an attempt was made to limit the phenomenon of *overtraining* (that is a better signal efficiency in the training than in the validation sample, for a given background efficiency) by choosing "overtraining-safe" values of some of the parameters, such as the maximum depth of the decision tree.

The BDT input variables have been chosen accurately, taking care to individuate ones with a strong signal-to-background discrimination power, low correlation between each other and a good agreement between data and background estimation.

In the next sections, the differences of the MVA category per category are explained. As anticipated, the VH category is statistically limited, and the MVA has not been attempted.

7.1 Gluon fusion MVA

The variables feeding the BDT in the gluon fusion category are:

- $\mathrm{iso}_{\mathrm{ch}}^{\mathrm{trk}_1}$ defined in Eq. 6.1,
- $p_T^{\mathrm{ditrk}}/m_{\mathrm{ditrk}\gamma}$,
- $E_T^{\gamma}/m_{\mathrm{ditrk}\gamma}$,
- η_{ditrk}.

The tranverse momentum of the best pair and the transverse energy of the photon are divided by the invariant mass of the best pair and the photon in order to decrease their correlation with the invariant mass spectrum and reduce

its distorsion. In Tab. 7.1 the correlation matrices between variables are reported for the $\rho\gamma$ decay channel. A ranking of the BDT input variables is derived by

$\rho\gamma$ signal - correlation matrix

input var.	$\mathrm{iso}_{\mathrm{ch}}^{\mathrm{trk}_1}$	$p_T^{\mathrm{ditrk}}/m_{\mathrm{ditrk}\gamma}$	$E_T^{\gamma}/m_{\mathrm{ditrk}\gamma}$	η_{ditrk}	$m_{\mathrm{ditrk}\gamma}$
$\mathrm{iso}_{\mathrm{ch}}^{\mathrm{trk}_1}$	+1.000	−0.243	−0.091	−0.000	+0.011
$p_T^{\mathrm{ditrk}}/m_{\mathrm{ditrk}\gamma}$	−0.243	+1.000	+0.008	−0.001	−0.069
$E_T^{\gamma}/m_{\mathrm{ditrk}\gamma}$	−0.091	+0.008	+1.000	+0.002	−0.031
η_{ditrk}	−0.000	−0.001	+0.002	+1.000	−0.009
$m_{\mathrm{ditrk}\gamma}$	+0.011	−0.069	−0.031	−0.009	+1.000

$\rho\gamma$ background - correlation matrix

input var.	$\mathrm{iso}_{\mathrm{ch}}^{\mathrm{trk}_1}$	$p_T^{\mathrm{ditrk}}/m_{\mathrm{ditrk}\gamma}$	$E_T^{\gamma}/m_{\mathrm{ditrk}\gamma}$	η_{ditrk}	$m_{\mathrm{ditrk}\gamma}$
$\mathrm{iso}_{\mathrm{ch}}^{\mathrm{trk}_1}$	+1.000	−0.156	+0.000	+0.001	−0.033
$p_T^{\mathrm{ditrk}}/m_{\mathrm{ditrk}\gamma}$	−0.156	+1.000	−0.197	+0.006	−0.221
$E_T^{\gamma}/m_{\mathrm{ditrk}\gamma}$	+0.000	−0.197	+1.000	+0.003	−0.010
η_{ditrk}	+0.001	+0.006	+0.003	+1.000	+0.002
$m_{\mathrm{ditrk}\gamma}$	−0.033	−0.221	−0.010	+0.002	+1.000

Table 7.1: Correlation matrices for the BDT input variables of the $H \to \rho\gamma$ channel. The invariant mass of the Higgs candidate has been added to the last row and column just to check the correlation with other variables, but no training or testing have been performed using this variable.

counting how often the variables are used to split the decision tree nodes, and by weighting each split occurrence by the separation gain-squared it has achieved and by the number of events in the node. The results are presented in Tab. 7.2. In Fig. 7.1 the BDT discriminant distribution is reported, showing the different behaviour of signal and background estimation, while in Fig. 7.2 the trend of the background rejection efficiency as a function of the signal efficiency is shown. The ROC curve integral is about 85 % for $\rho\gamma$ channel, about 86 % for $\phi\gamma$ channel and about 85 % for $K^{*0}\gamma$ channel. It is chosen as the BDT discriminant threshold the one which maximizes the significance Z, which is calculated as

$$Z = \frac{S\epsilon_S^{\mathrm{BDT}}}{\sqrt{B\epsilon_B^{\mathrm{BDT}}}} \tag{7.1}$$

$\rho\gamma$ **channel**		$\phi\gamma$ **channel**		$K^{*0}\gamma$ **channel**	
variable	R	variable	R	variable	R
η_{ditrk}	0.34	η_{ditrk}	0.35	η_{ditrk}	0.32
$p_T^{\text{ditrk}}/m_{\text{ditrk}\gamma}$	0.25	$p_T^{\text{ditrk}}/m_{\text{ditrk}\gamma}$	0.24	$p_T^{\text{ditrk}}/m_{\text{ditrk}\gamma}$	0.25
$\text{iso}_{\text{ch}}^{\text{trk}_1}$	0.24	$\text{iso}_{\text{ch}}^{\text{trk}_1}$	0.23	$\text{iso}_{\text{ch}}^{\text{trk}_1}$	0.24
$E_T^{\gamma}/m_{\text{ditrk}\gamma}$	0.18	$E_T^{\gamma}/m_{\text{ditrk}\gamma}$	0.18	$E_T^{\gamma}/m_{\text{ditrk}\gamma}$	0.19

Table 7.2: Ranking of the BDT input variables. "R" column reports the "ranking" parameter for each variable.

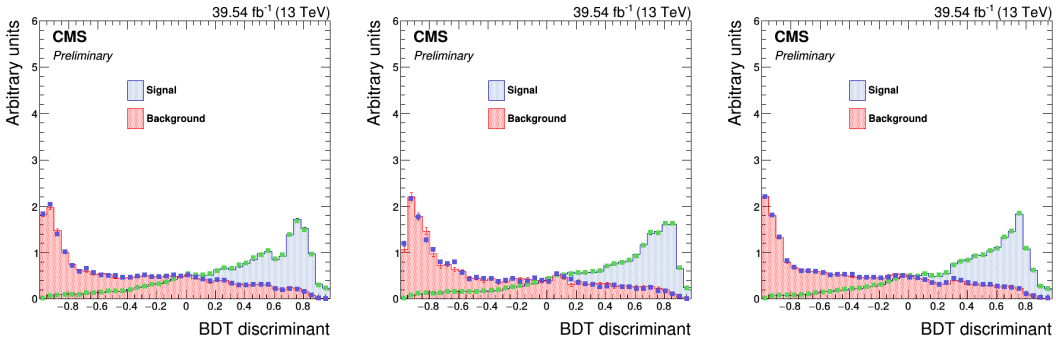

Figure 7.1: Event distributions as a function of the BDT discriminant for $\rho\gamma$ (left), $\phi\gamma$ (middle) and $K^{*0}\gamma$ (right) channels. The signal and background histograms are normalized to the same area. Dots refer to training samples, while colored areas to testing ones.

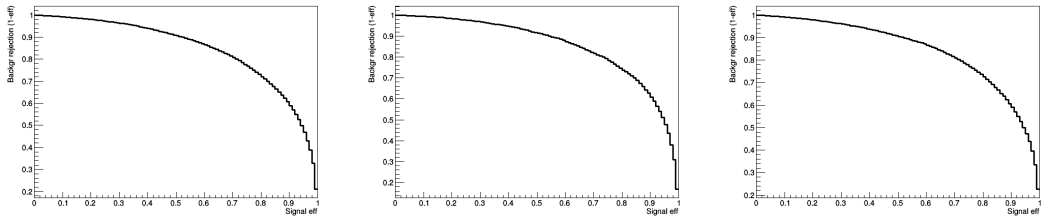

Figure 7.2: ROC curve: observed trend of the background rejection efficiency as a function of the signal efficiency, for $\rho\gamma$ (left), $\phi\gamma$ (middle) and $K^{*0}\gamma$ (right) channels. ROC curve integral are respectively 85 %, 86 %, 85 %.

where S and B are the expected number of signal events with a branching ratio of 10^{-5} and background events after the first event selection, and ϵ_S^{BDT} and ϵ_B^{BDT} are the signal and background efficiencies as a function of the BDT discriminant. To prevent bias from background-enriched mass sidebands, the Z-score is calculated only using signal and background events in the invariant mass range from 120 to 130 GeV. In Fig. 7.3, significance trends for the three

decay channels are reported as function of the signal efficiency. Therefore, the

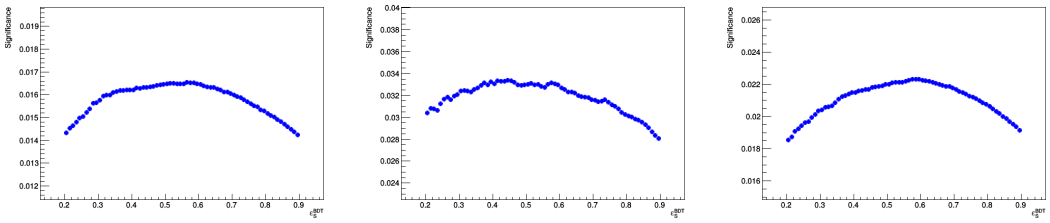

Figure 7.3: Significance as a function of the signal efficiency for the $\rho\gamma$ (left), $\phi\gamma$ (middle) and $K^{*0}\gamma$ (right) channels.

BDT discriminant threshold has to be preferred considering the largest value of significance which could also allow to contain enough events in the SR of the $m_{\text{ditrk}\gamma}$ distribution to be well fitted. In summary, the following thresholds on the BDT discriminant and respective significance values are defined:

- $\rho\gamma$ channel : BDT> 0.395 for $Z = 0.017$;
- $\phi\gamma$ channel : BDT> 0.427 for $Z = 0.033$.
- $K^{*0}\gamma$ channel : BDT> 0.373 for $Z = 0.022$.

BDT thresholds are used to define the most sensitive category. This BDT category includes events with a BDT-score higher than thresholds listed above for $\rho\gamma$ and $\phi\gamma$ channels respectively. Rather than discarding events that do not fall into the most sensitive category, a less sensitive BDT category is considered, taking into account events with a BDT-score lower than those thresholds. The strategy is to exploit the two BDT categories to maximise the combined significance. From now on, the most sensitive category will be labeled in this note as BDTcat0, while the other one as BDTcat1.

The lower output-score threshold for BDTcat1 has been decided with the aim to achieve a reasonable improvement to the combined significance. To guarantee this, a significance scan have been performed lowering the value of the lower output-score threshold until the improvement on combined significance was found to be negligible. For each decay channel this border has been set to BDT-score equal to -0.4. Once the MVA selection has been performed, a further cut has been added on isolation of the meson from neutral particles. Events are rejected if the meson candidate does not meet the following requirement:

$$\text{iso}^{\text{neu}}_{\text{ditrk}} > 0.8, \tag{7.2}$$

where $\text{iso}^{\text{neu}}_{\text{ditrk}}$ is defined in Eq. 6.2. This cut has a big discriminating power between signal and background and it has been applied at this stage, after the MVA, to let the MVA to have enough statistics for training and testing procedures. The reason to not include this variable among the ones used as BDT input variables is to facilitate the calculation of data/MC scale factors on isolation efficiency, explained in Sec. 8.2. The cut flow of data events and signal efficiencies after each step of the selection are reported in Tab. 7.3 and in Tab. 7.4 respectively.

Data events cut flow	
Triggered events	45862248
Ev. with a best photon	15835700

Decay channel	$\rho\gamma$	$\phi\gamma$	$K^{*0}\gamma$
Ev. with a best pair	194984	14440	102603
BDTcat0 (BDTcat1)	10513 (22841)	785 (1568)	6635 (12081)
BDTcat0 (BDTcat1) m_{ditrk} sideb.	3372 (7720)	597 (1232)	4541 (9157)

Table 7.3: Data events cut flow in ggH category. The last row reports the events remaining in the sidebands of the m_{ditrk} distribution after the MVA-based cut.

Signal MC events cut flow	$\rho\gamma$	$\phi\gamma$	$K^{*0}\gamma$
Ev. triggered	23.8%	20.7%	23.2%
Ev. with a best photon	20.9%	18.3%	20.4%
Ev. with a best pair	10.0%	11.0%	9.5%
BDTcat0 (BDTcat1)	4.8% (2.9%)	5.5% (3.2%)	5.0% (2.7%)

Table 7.4: Signal MC events cut flow in ggH category.

Distributions of the invariant mass of the two tracks and the photon are shown in Fig. 7.4 and Fig. 7.5 for both ggH BDT sub-categories. Despite the low statistics, a good agreement between data and background estimation is still observed within the statistical uncertainties.

7.2 VBF MVA

As it has been previously mentioned, the VBF signal offers a distinctive signature involving two jets with a large m_{jj} and $|\Delta\eta_{jj}|$. Therefore, different variables are

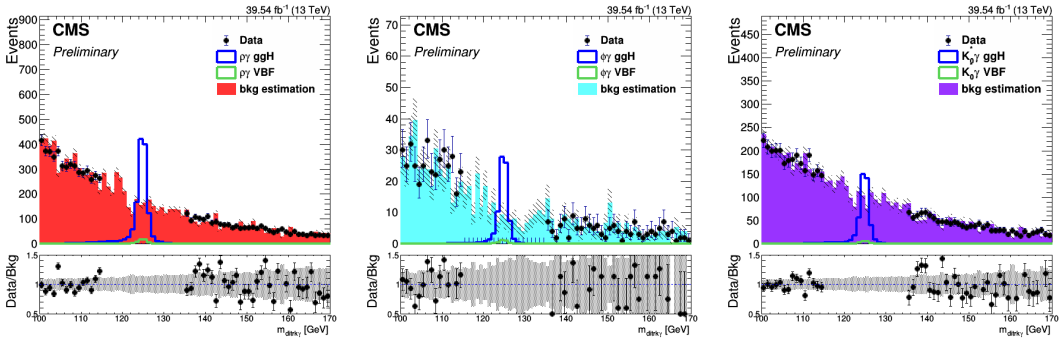

Figure 7.4: Invariant mass distribution of the ditrack and the photon for ggH BDTcat0.

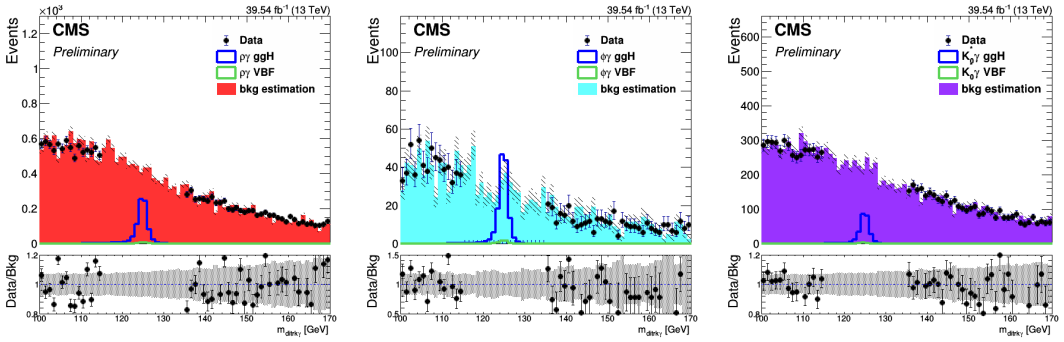

Figure 7.5: Invariant mass distribution of the ditrack and the photon for ggH BDTcat1.

used to feed the BDT are in the VBF and VBFlow categories. They are:

- $p_T^{\text{ditrk}\gamma}$: transverse momentum of the Higgs candidate of the event;
- p_T^{γ}: transverse energy of the best photon of the event;
- p_T^{ditrk}: transverse momentum of the candidate meson of the event;
- ΔR_{ditrk}: spatial separation between the two tracks composing the meson;
- mvaID_{γ}: multivariate selector for photon identification;
- $\text{iso}_{\text{ch}}^{\text{ditrk}}$: isolation of the best pair from charged particles;
- m_{jj}: invariant mass of the two VBF jets;
- $\Delta\phi(j_1, j_2)$: difference of the azimuthal angles of the two VBF jets.

In Fig. 7.6 and Fig. 7.7 the BDT discriminant distributions for VBF and VBFlow categories are reported, showing the different behaviour of signal and background estimation. Most contributing MC backgrounds are reported in plot

legends, and data sidebands of the invariant mass of the meson are used as a validation. The thresholds on the BDT discriminant have been defined with the same criteria used in the gluon fusion category and set to BDT > 0.7 for VBF and VBFlow categories. Furthermore, a less sensitive BDT category is considered, as done for ggH, by defining two sub-categories for each VBF category, labeled BDTcat0 and BDTcat1. The lower border of BDTcat1 has been set to BDT-score equal to -0.6.

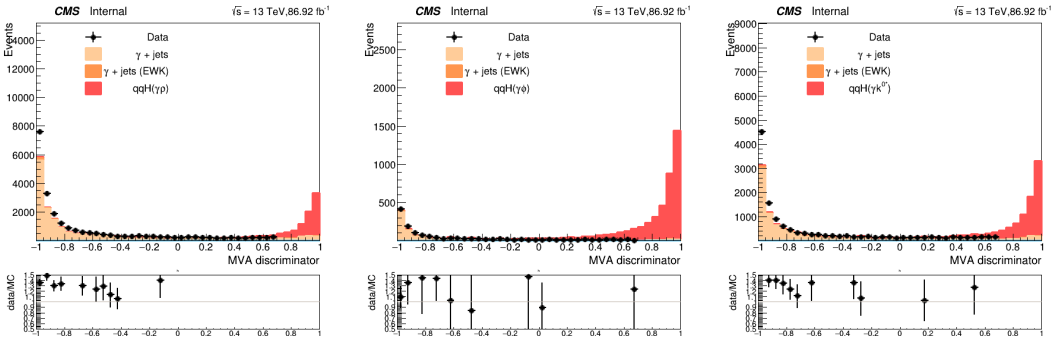

Figure 7.6: Event distributions as a function of the BDT discriminant for $\rho\gamma$ (left), $\phi\gamma$ (middle) and $K^{*0}\gamma$ (right) channels in the VBF category. Most contributing MC backgrounds are reported in plot legends, and data sidebands (black dots) of the invariant mass of the meson are used as a validation.

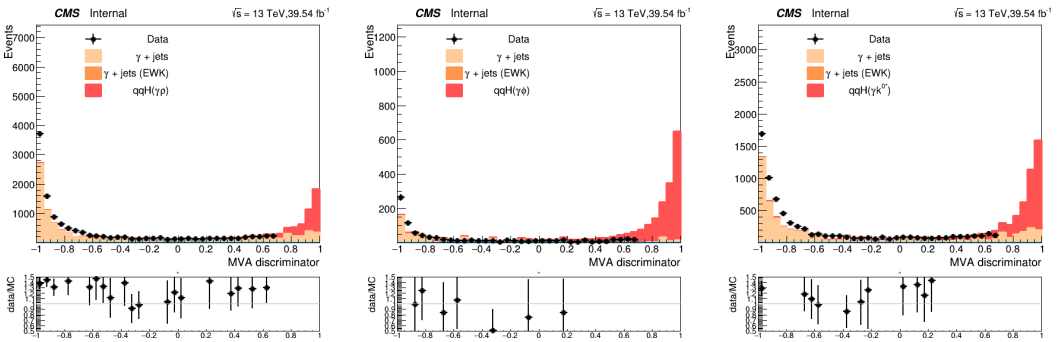

Figure 7.7: Event distributions as a function of the BDT discriminant for $\rho\gamma$ (left), $\phi\gamma$ (middle) and $K^{*0}\gamma$ (right) channels in the VBFlow category. Most contributing MC backgrounds are reported in plot legends, and data sidebands (black dots) of the invariant mass of the meson are used as a validation.

Data/MC corrections 8

The weight of the simulated events, defined as W in Eq. 4.2, incorporates scale factors (SFs) that correct the conditions used in MC to those observed during the data-taking. Within the CMS Collaboration, these SFs are typically the same for all analyses in the Collaboration. They address disparities between data and MC in areas such as the efficiency of the trigger system, as well as in the identification, reconstruction, and isolation of particles. An exception is noted for the HLT efficiency SFs related to the specific trigger described in Sec. 5.1.1. Additionally, the isolation variable created in this study to separate signal from background is a custom variable designed for this search. It is necessary to ensure that the selection based on this variable performs comparably in both data and simulations, and to measure any discrepancies by calculating SFs.

Furthemore, the signal MC samples used in this analysis are simulated without considering polarization effects that arise from angular momentum conservation. A correction for this effect is reported in this chapter, along with the entire procedure of HLT and isolation efficiency SFs determination and corrections due to the PU distribution.

8.1 HLT efficiencies

The HLT used in the analysis is described in Sec. 5.1. Since the trigger selects a pair of tracks with high transverse momentum in coincidence with an energetic photon, the calculation of trigger efficiency scale factors can be computed independently for the track pair and for the photon, factorizing them. In either case, SFs are computed as the ratio between the trigger efficiency calculated on

data and the trigger efficiency calculated on a simulated dataset:

$$\mathrm{SF} = \frac{\epsilon_{\mathrm{Data}}}{\epsilon_{\mathrm{MC}}}. \tag{8.1}$$

Given that the dataset employed for these calculations cannot be the one collected by this specific trigger, it is essential to calculate the scale factors using an orthogonal dataset. This dataset should be unbiased to the selection criteria of the trigger for which the SFs are being computed. Dataset and MC simulation used to perform the entire procedure are respectively a dataset from a HLT trigger selecting an isolated muon with a threshold of 24 GeV and a DY MC sample with muons in the final state.

In order to simplify the procedure, the trigger SFs are factorized into two orthogonal contributions, *photon leg* (PL) and *two prongs leg* (TPL), such that

$$\mathrm{SF} = \mathrm{SF}_{\mathrm{PL}} \cdot \mathrm{SF}_{\mathrm{TPL}}. \tag{8.2}$$

A single photon trigger (HLT_γ) requiring a photon with $p_T^\gamma = 30$ GeV and a muon with $p_T^\mu = 17$ GeV and a tau jet trigger ($\mathrm{HLT}_{\mathrm{jet}}$) with a cut on the jet transverse momentum of 35 GeV and requiring a muon with $p_T^\mu = 24$ GeV, are used to compute two separated sets of SFs for the two legs.

For the PL, the trigger efficiency is calculated via the formula below

$$\epsilon_\gamma^{\mathrm{HLT}} = \frac{\mathrm{HLT}_\gamma \ \wedge \ \text{offline selection} \ \wedge \ \mathrm{HLT}_\mu}{\text{offline selection} \ \wedge \ \mathrm{HLT}_\mu} \tag{8.3}$$

which is the ratio between the sum of events that trigger simoultaneously HLT_γ and HLT_μ, a trigger requiring a muon with $p_T^\mu = 24$ GeV, and pass the offline selection of the photon as described in Sec. 5.2.3, over the sum of events that trigger HLT_μ and pass the offline selection. The photon selection within HLT_γ is the same adopted by the trigger used for this analysis with the only difference in the transverse energy threshold. The photon transverse energy threshold has been moved to 35 GeV reproducing exactly the original photon trigger leg within HLT_Photon35_TwoProngs35. Furthermore, in order to guarantee a good agreement between data and MC DY sample, a pair of muons with opposite charge compatible with the Z boson is required in the offline selection. Muon selection is reported in Tab. 8.1. PL scale factors are computed via the Eq. 8.1 as the ratio of this efficiency calculated in data and MC sample. They are reported in Fig. 8.1 binned in transverse energy of the photon.

muon ID	tight
$p_T^{\mu,\text{leading}}$	> 25 GeV
$p_T^{\mu,\text{subleading}}$	> 5 GeV
$\lvert\eta_\mu\rvert$	< 2.4
d_{xy}	< 0.2 cm
d_z	< 0.5 cm
$m_{\mu\mu}$	between 65 and 115 GeV

Table 8.1: Muons selection for the trigger efficiency scale factors calculation.

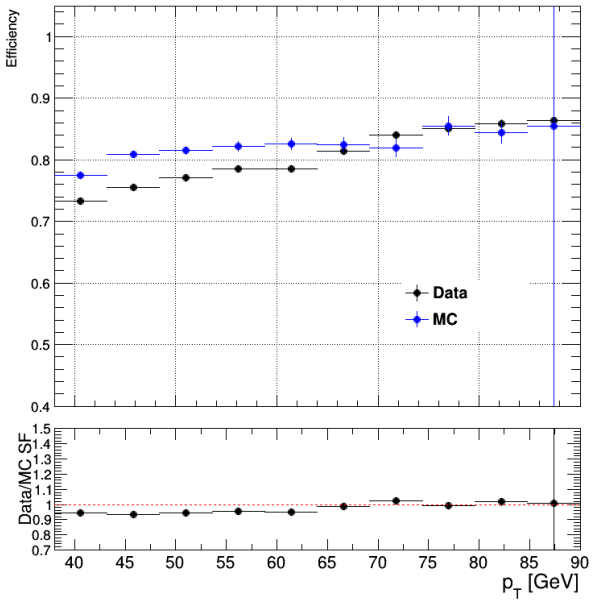

Figure 8.1: Photon trigger efficiencies binned in transverse energy of the photon for data and MC (top) and corresponding SFs (bottom).

The efficiency of the TPL is calculated via a similar formula

$$\epsilon^{\text{HLT}}_{\text{TwoProngs}} = \frac{\text{HLT}_{\text{jet}} \ \wedge \ \text{offline selection} \ \wedge \ \text{HLT}_\mu}{\text{offline selection} \ \wedge \ \text{HLT}_\mu} \tag{8.4}$$

which is the ratio between the sum of events that trigger simoultaneously HLT_{jet} and HLT_μ and pass the offline selection of the best pair of the event as described in Sec. 5, over the sum of events that trigger HLT_μ and pass the offline selection. HLT_{jet} is a control trigger created on purpose with the same selection for the two tracks described in Sec. 5.1.

While for the PL, numerator and denominator of $\epsilon_\gamma^{\text{HLT}}$ are calculated as a ratio of the number of events for each of the transverse energy bin, the calculation

of numerator and denominator of $\epsilon^{\text{HLT}}_{\text{TwoProngs}}$ is less trivial for two main reasons. First, the smaller amount of data forces a reduction in the number of bins and to implement different bin sizes for higher values of transverse momentum. Second, all those events that satisfy numerator and denominator conditions in Eq. 8.4 are further required to fall under the peak of the invariant mass spectrum of the meson. This removes fake mesons in the efficiency calculation. To perform this, the number of events for numerator and denominator are computed (for each bin) as the area between the background-only and the signal-plus-background fits to the invariant mass spectrum of the meson. The per-bin efficiency determination is accomplished by performing a simultaneous fit on both the events that pass the trigger selection (*pass* region) and on the events that fail the trigger selection (*fail* region). The fit is conducted with the constraint that the signal corresponds to the number of signal events extracted by the fit in the pass region multiplied by the efficiency and the number of signal events in the pass region multiplied by (1 - eff). Examples of fits to pass and fail distributions of a p_T bin are reported in Fig. 8.3 for data and Fig. 8.4 for MC, while the resulting trigger efficiency and scale factors are shown in Fig. 8.5.

Since kaons and pions are indistinguishable at trigger level, SFs are computed exploting the ϕ meson narrow width, hence the same SFs are applied for $\rho\gamma$ and $K^{*0}\gamma$ channels. To validate the choice of the DY MC sample a data/MC comparison is reported in Fig. 8.2.

8.2 Isolation efficiency

A tag-and-probe approach is used to measure the isolation efficiency of ρ, ϕ and K^{*0} candidates in data and simulation, using $Z \to \mu\mu$ events. The *Tag and Probe* method in high-energy physics is a commonly used technique for measuring the efficiency of particle identification and reconstruction. This method hinges on the identification of two types of particles: the tag and the probe. The tag is a particle identified with high confidence using stringent selection criteria, ensuring that it is very likely to be the particle type of interest, such as an electron or muon. The reliability of the tag is crucial, as it serves as a reference for measuring the efficiency of identifying the probe. The probe is a particle whose identity is not yet confirmed. It is used to test the efficiency of the identification criteria. By applying these criteria to the probe and observing its rate of passing, the efficiency of the particle identification process is assessed. The efficiency is

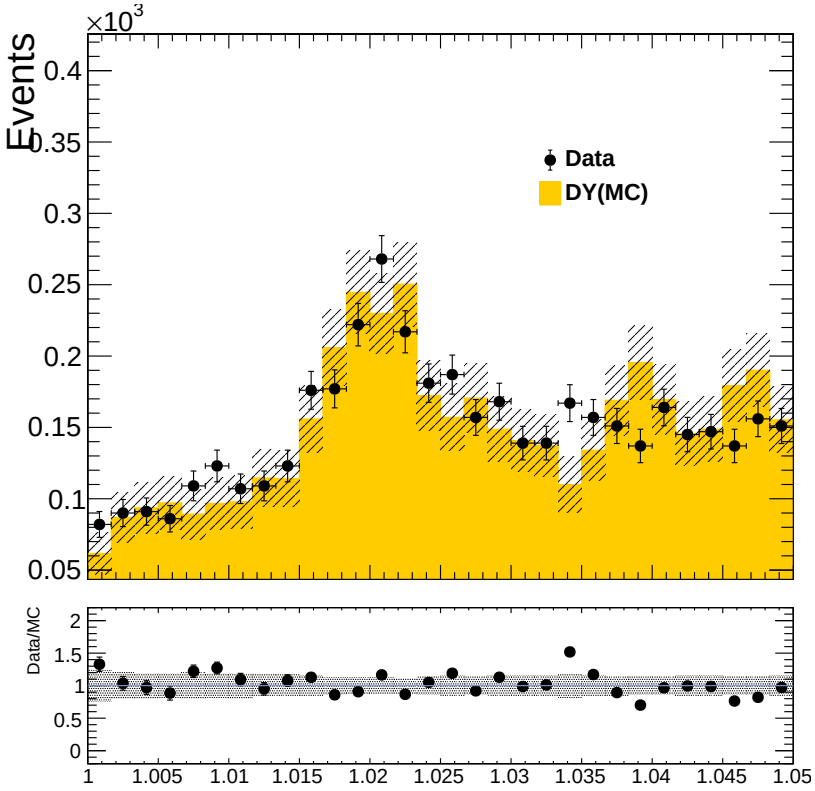

Figure 8.2: DY MC vs data comparison plot in the invariant mass of the ϕ meson distribution. MC area is normalized to data one.

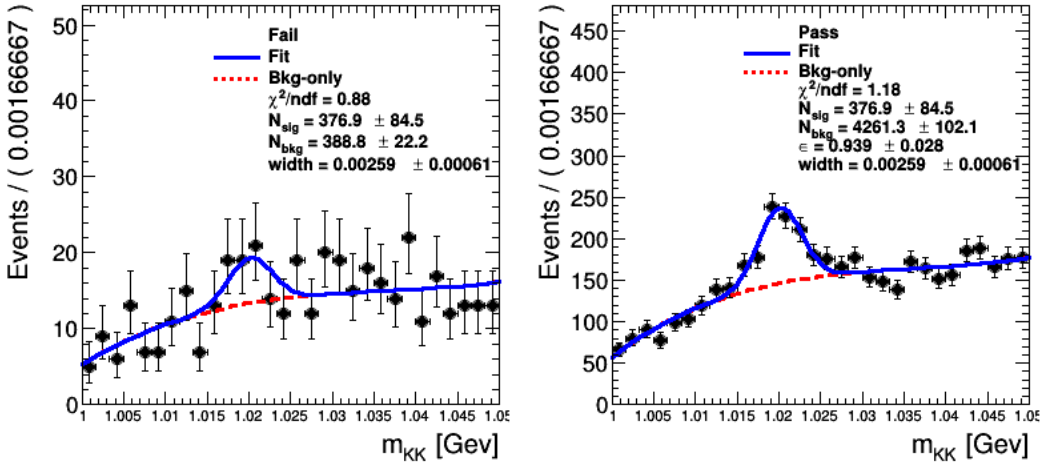

Figure 8.3: Background-only (red) and signal-plus-background (blue) fits to invariant mass spectrum of the meson for the second transverse momentum bin in data (corresponding to $42 < p_T^{KK} < 50$ GeV).

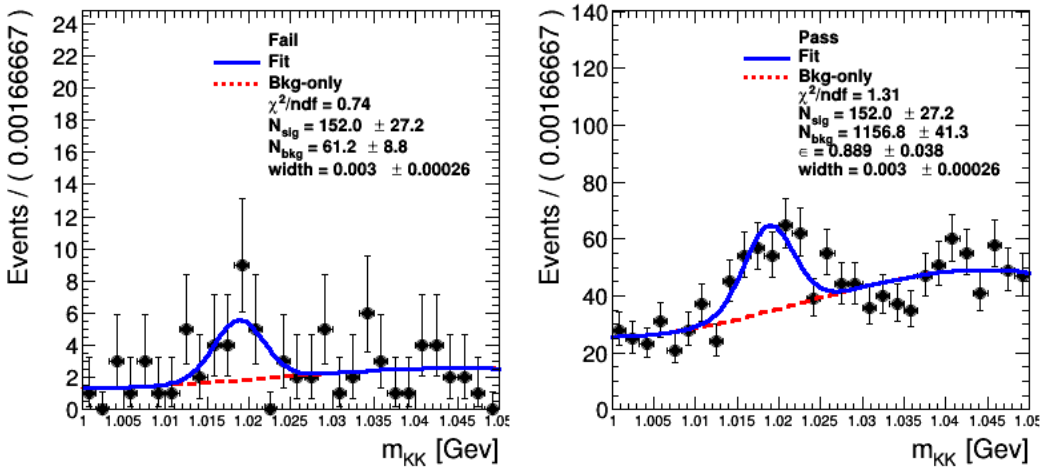

Figure 8.4: Background-only (red) and signal-plus-background (blue) fits to invariant mass spectrum of the meson for the second transverse momentum bin in MC (corresponding to $42 < p_T^{KK} < 50$ GeV).

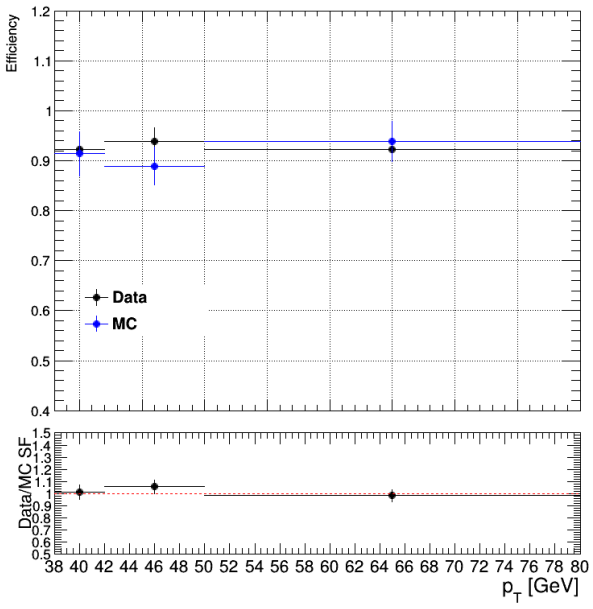

Figure 8.5: Two prongs trigger scale factors binned in transverse momentum of the pair of tracks.

calculated using the formula:

$$\epsilon = \frac{\text{Number of probes passing selection criteria}}{\text{Total number of probes}} \tag{8.5}$$

This formula yields the ratio of probes correctly identified as the intended particle type (e.g., electrons, muons) to the total number of probes tested,

providing a direct measure of the effectiveness of the identification criteria. In the measurement described in this section, the probe muon serves as a proxy for the di-track candidate and it is not subjected to stringent isolation requirements. The criteria for the tag muon are such that it must comply with the tight muon ID and must be isolated. Additionally, the tag muon must activate the single muon trigger detailed in Sec. 5.1. Tag-and-probe pairings are generated by combining tag muons and probe muons that have a separation of $\Delta R > 0.4$ and fall in an invariant mass range compatible with the Z rest mass. Efficiencies are computed for the isolation variables $\text{iso}^{\text{ch}}_{\text{ditrk}}$ and $\text{iso}^{\text{neu}}_{\text{ditrk}}$. Regions of pass and fail are defined by whether the probe muon passes or fails the isolation requirement, respectively $\text{iso}^{\text{ch}}_{\text{ditrk}} > 0.9$ and $\text{iso}^{\text{neu}}_{\text{ditrk}} > 0.8$. The $\text{iso}^{\text{ch}}_{\text{ditrk}}$ threshold is identical to the one implemented in the preselection, while the $\text{iso}^{\text{neu}}_{\text{ditrk}}$ threshold is implemented after the MVA-based cuts.

Efficiencies are computed in seven p_T bins of the probe muon and two η bins depending on whether the proxy meson falls in the barrel or endcap region, and extracted by conducting a simultaneous fit to the di-muon mass distribution in the pass and fail datasets for both the probes that pass and those that fail the isolation requirement. The $Z \to \mu\mu$ signal is modeled using a Voigtian, while the background is represented by a 2nd order Chebychev polynomial. Figures 8.6 and 8.7 present the isolation efficiencies of $\text{iso}^{\text{ch}}_{\text{ditrk}}$ and $\text{iso}^{\text{neu}}_{\text{ditrk}}$ from both data and MC simulations and the corresponding scale factors. Deviations of up to 2 % have been noted by comparing efficiency computed from the $Z \to \mu\mu$ simulation and the efficiency found in the signal samples. Based on such observation, a systematic uncertainty is computed as the maximum observed difference between the efficiency as measured with the $Z \to \mu\mu$ tag-and-probe and the efficiency ascertained from the signal samples, as shown in Chap. 10.

8.3 Spin-alignment reweighting

The decays $H \to \phi\gamma \to KK$, $H \to \rho\gamma \to \pi\pi$ and $H \to K^{*0}\gamma \to K\pi$ are simulated isotropically using Pythia, yet in reality polarisation effects are significant. As the Higgs boson is a scalar particle, angular momentum conservation enforces fully transverse spin alignment of the outgoing mesons. To incorporate these effects, the expected angular distribution is computed for a polarisation state, then the signal samples are adjusted accordingly through reweighting. This reweighting relies on the polar angle between the trajectory of one of the tracks

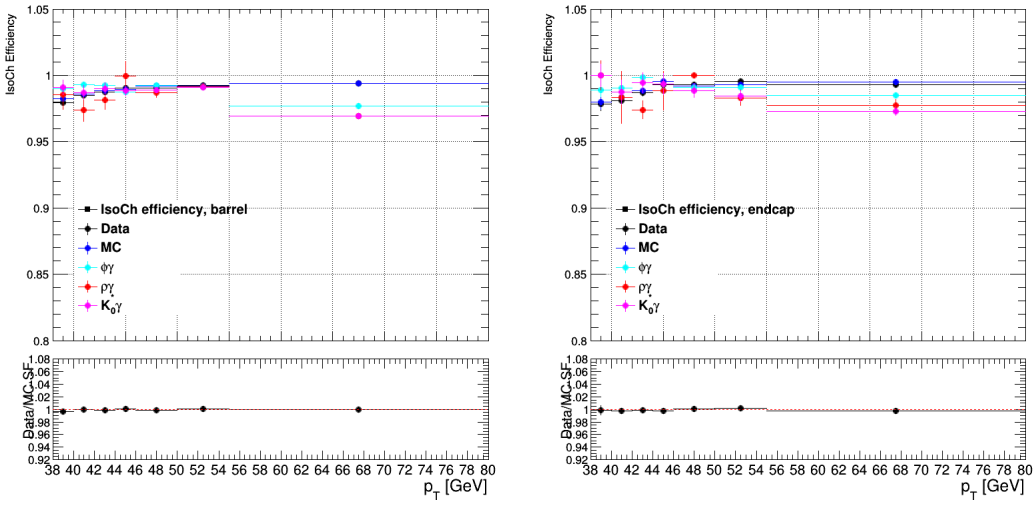

Figure 8.6: The efficiency for muons to pass the track-based $\text{iso}^{\text{ch}}_{\text{ditrk}}$ for barrel mesons (left) and for the endcap mesons (right). The efficiency determined through a *T&P* technique is juxtaposed with the di-track isolation efficiency derived from the signal samples.

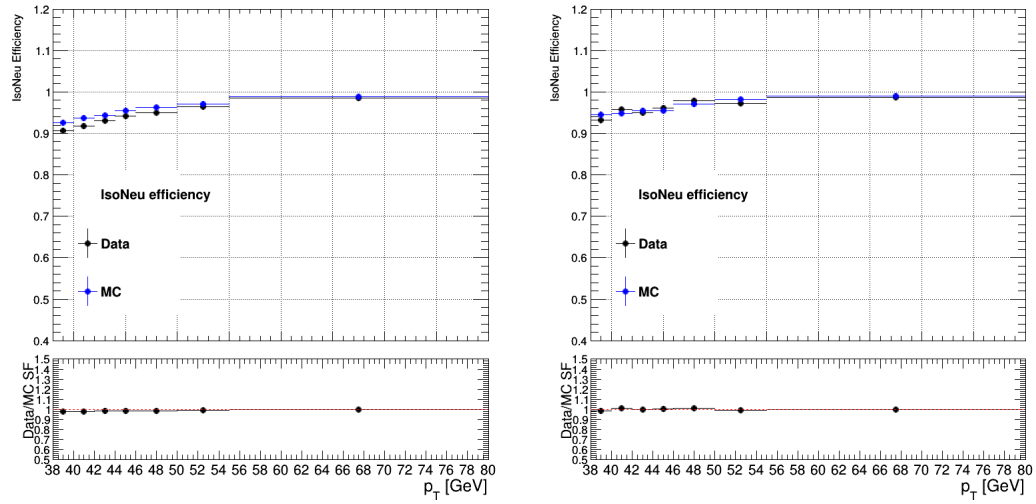

Figure 8.7: The efficiency for muons to pass the track-based $\text{iso}^{\text{neu}}_{\text{ditrk}}$ for barrel mesons (left) and for the endcap mesons (right).

(decay products of the meson) in the rest frame of the meson and the direction of the meson in the Higgs boson frame. While this reweighting does not alter the reconstructed Higgs boson mass, it can affect the signal yields as the reweighting is applied prior to kinematic selections.

The meson's decay introduces an angular distribution,

$$I(\theta) \propto \frac{\sin^2(\theta)}{2}. \tag{8.6}$$

In this formula, θ represents the polar angle. The reweighting function is multiplied by a normalisation factor such that they preserve the total normalisation before kinematic selection, and this factor is 3. Figure 8.8 the distribution of $\cos\theta$ for the two different polarisation scenarios.

The subsequent Figs. 8.9, 8.10, 8.12 depict the impact of the reweighting process on some interesting variables at the generator level. While the pseudorapidity of the outgoing leading tracks is basically not modified by the reweighting, the p_T spectrum is moved to larger values, as shown in figures. The reweighting, despite the varied helicity states, leaves the shape of the reconstructed Higgs boson mass distribution unaffected. Nevertheless, it does cause an adjustment in the signal efficiency, increasing it by a factor of 6.6% for the ϕ channel, 7.2% for the ρ channel and 9.4 % for the K^{*0} channel.

8.4 Pile-up reweighting

To ensure consistency between simulated events and observed data, the signal MC PU distribution is corrected by assigning weights to align it with data. This is achieved by adjusting the generated count of inelastic collisions for each event through a weigh that compensates for the variations in instantaneous luminosity.

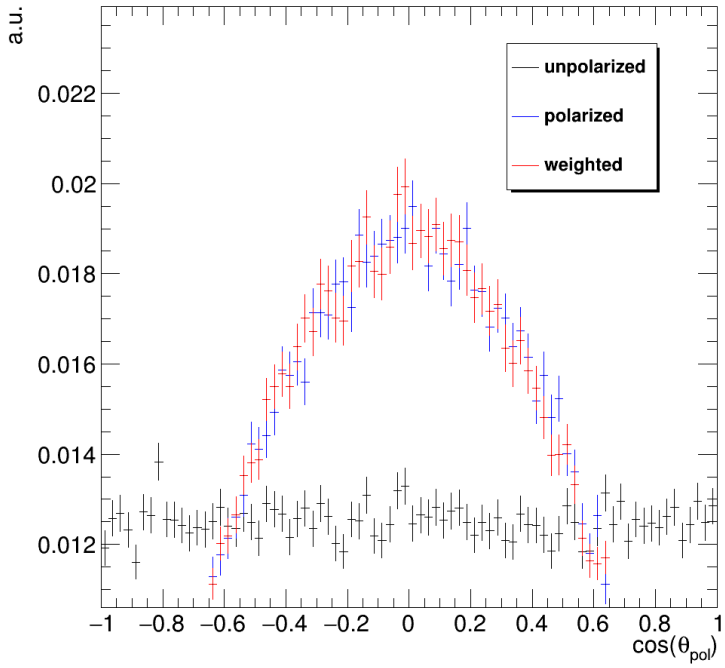

Figure 8.8: $\cos\theta$ for the ρ meson decay. The black flat distribution illustrates the polarization angle within the centrally produced MC signal. The blue distribution portrays a privately generated MC signal wherein the accurate polarization was already incorporated. The red distribution results from reweighting the black distribution using the reweighting technique outlined in this section.

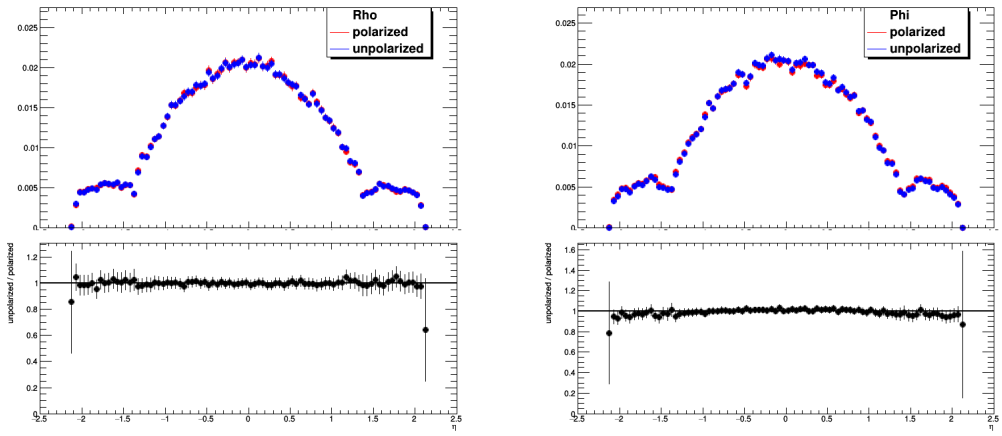

Figure 8.9: η distribution of the leading track for the polarized and unpolarized scenarios.

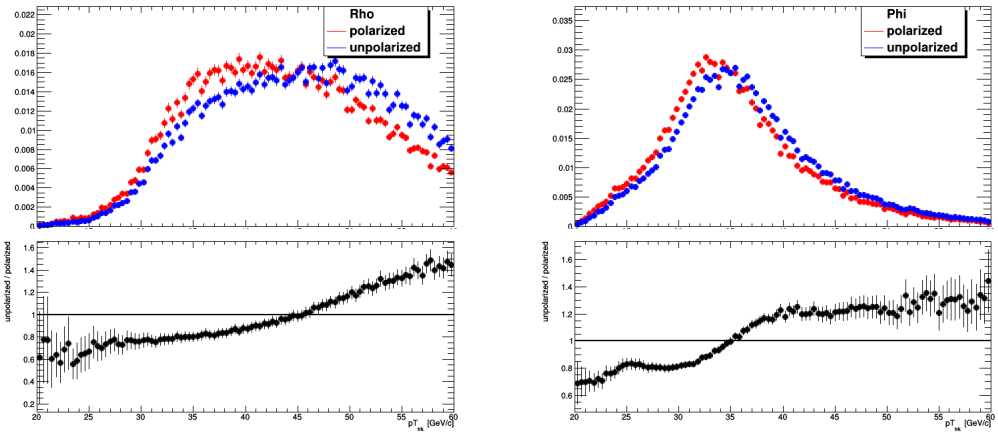

Figure 8.10: p_T distribution of the leading track for the polarized and unpolarized scenarios.

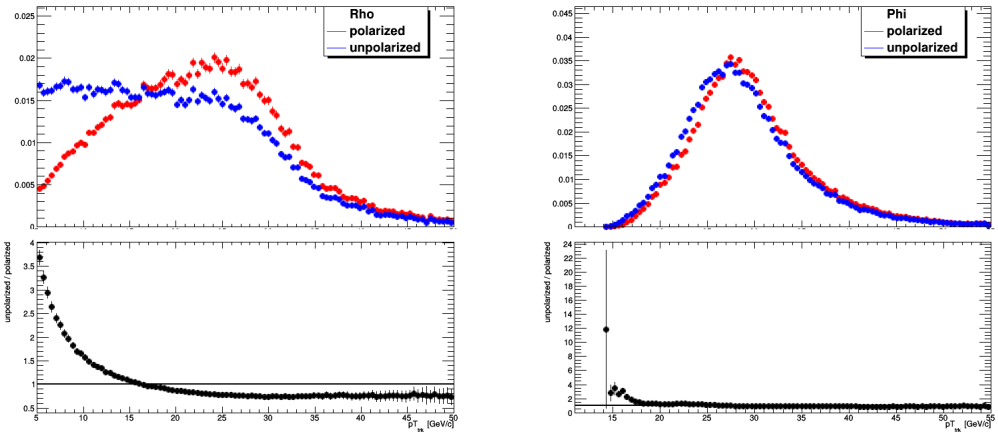

Figure 8.11: p_T distribution of the leading track for the polarized and unpolarized scenarios.

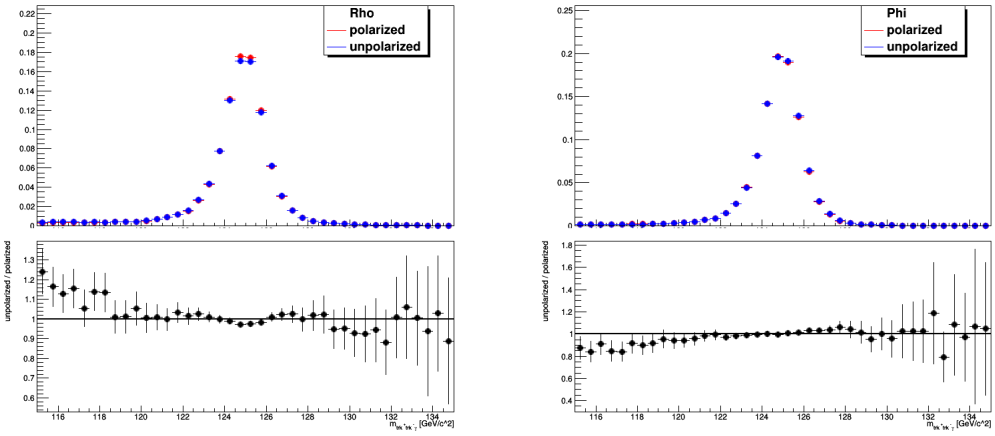

Figure 8.12: Higgs invariant mass distribution for the polarized and unpolarized scenarios for the $H \to \rho\gamma$ (left) and $H \to \phi\gamma$ (right).

Invariant mass fit 9

The purpose of this analysis is to measure the branching ratio of Higgs boson rare decays $H \to \rho\gamma$, $H \to \phi\gamma$ and $H \to K^{*0}\gamma$. The value of the branching ratios can be measured counting the excess in data around the Higgs boson mass in the invariant mass spectrum, which cannot be compatible with a statistical fluctuation of the background. If this will not be the case, an upper limit of the branching ratio can be determined given a certain confidence level. The observable related to the branching ratio is the number of signal events. Therefore, the entire selection procedure has been conceived to select the signal and reject the background.

The characterization of signal and background in the invariant mass spectrum and the *maximum likelihood method* employed for fitting are reported in this chapter. Once the probability density functions (pdf) which best model background and signal distributions are found, they are combined providing a total pdf sensitive to a signal presence over a background in the invariant mass spectrum. The main parameter of interest to be extracted from the invariant mass fit is the branching ratio. The observable correlated to the $\mathcal{B}$ value via Eq. 4.1 is N_{sig}. The pdf used to perform the fit is composed by the background pdf P_{bkg} and the pdf used for the description of the signal distribution, called P_{sig}. The combined pdf is thus defined as

$$P_{\text{TOT}} = N_{\text{sig}} \cdot P_{\text{sig}} + N_{\text{bkg}} \cdot P_{\text{bkg}}, \tag{9.1}$$

where N_{bkg} is a parameter representing the number of background events.

9.1 Maximum likelihood method

An extended maximum likelihood fit is performed in order to extract the signal yield. Assuming that one experiment measures the values $x_1, ..., x_n$ of n random variables and assuming also that the pdf depends on $\theta_1, ..., \theta_m$ unknown parameters, the *extended log-likelihood function* is defined as

$$-\ln \mathcal{L}(\vec{x};\vec{\theta}) = -\ln p(N;\vec{\theta}) - \sum_{i=1}^{N} \ln f(x_1^i, ..., x_n^i; \theta_1, ..., \theta_m), \tag{9.2}$$

where f is the pdf of the random variables $x_1, ..., x_n$ and $p(N;\vec{\theta}) = \frac{e^{-\nu(\vec{\theta})}\nu(\vec{\theta})^N}{N!}$ is the Poisson distribution.

The fit parameters are extracted minimizing the negative extended log-likelihood function. In this thesis work, a 1-dimension distribution is fitted and the analysis tool used to perform the maximum likelihood fit is MINUIT. MINUIT [70] is conceived as a numerical minimization computer program to find the minimum value of a multi-parameter function and analyze the shape of the function around the minimum. Its main application is the minimization of χ^2 and log-likelihood functions for statistical analysis, and it is used to compute the best-fit parameter values and uncertainties, including correlations between the parameters.
The Minuit processors MIGRAD and HESSE normally produce an error matrix. In this analysis the uncertainties of the fit parameter are calculated by MIGRAD, which works under the assumption that the likelihood behaves like an n-dimensional Gaussian. The error matrix provided by HESSE is the inverse of the matrix of second derivatives of the log-likelihood function.

9.2 Signal model

As explained in Sec. 4.1, the number of signal events, extracted from the invariant mass spectrum fit, can be parameterised as Eq. 4.1 where the integrated luminosity, the total efficiency of the selection, the Higgs boson production cross section at LHC, branching ratios of the meson decays are reported in Tab. 9.1.

The shapes of the signal distribution for the rare decays $H \to \rho\gamma$, $H \to \phi\gamma$ or $H \to K^{*0}\gamma$ aren't known "a priori". Therefore, the distribution of MC signal

	ggH	VBF	WH	ZH
$\mathcal{L}_{int}$ (fb^{-1})	39.5	137	137	137
$\sigma^{H,tot}_{13TeV}$ (pb) [71]	48.6	3.78	1.37	0.88
$\mathcal{B}(\phi \to K^+K^-)$ [71]	48.9%	48.9%	48.9%	48.9%
$\mathcal{B}(\rho \to \pi^+\pi^-)$ [71]	100%	100%	100%	100%
$\mathcal{B}(K^{*0} \to K^\pm\pi^\mp)$ [71]	100%	100%	100%	100%

Table 9.1: Values used for the $\mathcal{B}$ calculation.

events passing the selections is used to characterize the signal shape. The shape of the $m_{\text{ditrk}\gamma}$ distribution for simulated signal is parameterised for each Higgs boson decay mode. The pdf chosen for signal modelling is a double-sided Crystal Ball function (DCB). The core of the DCB function consists of a Gaussian distribution and tails are modelled by two functions:

$$\text{DCB} = \begin{cases} e^{-(m_{\text{ditrk}\gamma}-\hat{m})^2}/2\sigma^2, & -\alpha_L < \frac{m_{\text{ditrk}\gamma}-\hat{m}}{\sigma} < \alpha_R \\ (\frac{n_L}{|\alpha_L|})^{n_L} e^{-\alpha_L^2/2} (\frac{n_L}{|\alpha_L|} - |\alpha_L| - \frac{m_{\text{ditrk}\gamma}-\hat{m}}{\sigma})^{-n_L}, & \frac{m_{\text{ditrk}\gamma}-\hat{m}}{\sigma} \leq -\alpha_L \\ (\frac{n_R}{|\alpha_R|})^{n_R} e^{-\alpha_R^2/2} (\frac{n_R}{|\alpha_R|} - |\alpha_R| + \frac{m_{\text{ditrk}\gamma}-\hat{m}}{\sigma})^{-n_R}, & \frac{m_{\text{ditrk}\gamma}-\hat{m}}{\sigma} \geq \alpha_L \end{cases} \tag{9.3}$$

where $\hat{m}$ is the mean of the gaussian core and σ its standard deviation and $\alpha_{L,R}$ and $n_{L,R}$ are the parameters of the left and right tails.
Figures 9.1 and 9.2 show the fits for $\rho\gamma$, $\phi\gamma$ and K^{*0} channels for the two most sensitive categories of this analysis, BDTcat0 and BDTcat1, respectively. The values of the parameters extracted from the fit and the relative uncertainties computed by the HESSE algorithm of the MINUIT tool are reported in the plots legend.

The values of the σ parameter, representing the width of the distribution, underline a remarkable resolution of less than 1% on these final states, achieved also thanks to the CMS detector features.

9.3 Background Model

In order to evaluate the signal yield, a fit to the invariant mass spectrum, including the background, is performed. The choice of the pdf modelling the background is performed on data excluding the signal region. The description of the background distribution is provided by a *Chebychev Polynomial* pdf for all

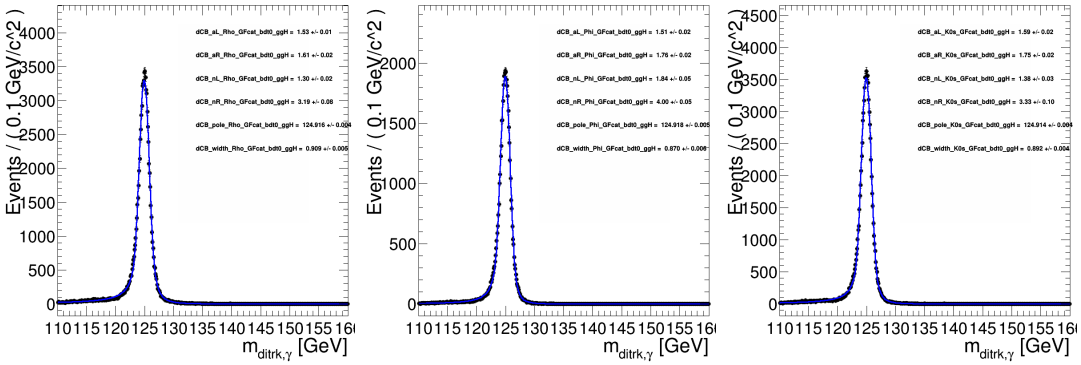

Figure 9.1: Signal model for $\rho\gamma$ (left), $\phi\gamma$ (middle), $K^{*0}\gamma$ (right) decay channels in the ggH BDTcat0 category.

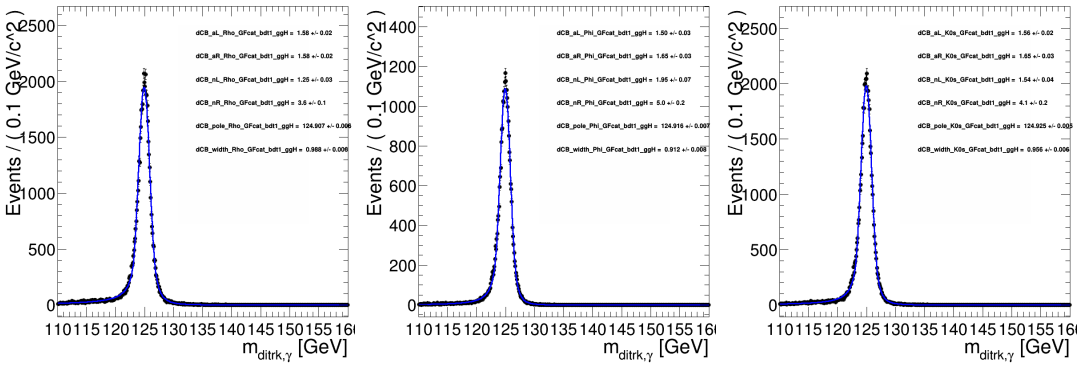

Figure 9.2: Signal model for $\rho\gamma$ (left), $\phi\gamma$ (middle), $K^{*0}\gamma$ (right) decay channels in the ggH BDTcat1 category.

the channels. A Chebychev Polynomial pdf of degree n is obtained by means of Rodrigue's formula:

$$T_n(x) = \frac{(-2)^n n!}{(2n)!}\sqrt{1-x^2}\frac{d^n}{dx^n}(1-x^2)^{n-1/2} \qquad n = 0, 1, 2, 3, ...$$

An arbitrary function can be expanded as a series of Chebychev polynomials:

$$f(x) = A_0T_0(x) + A_1T_1(x) + A_2T_2(x) + ... = \sum_{n=0} A_nT_n(x).$$

The fits, performed on data blinded in a region between 120 GeV and 130 GeV, are reported in Figs. 9.3-9.8 for the two most sensitive categories of this analysis, BDTcat0 and BDTcat1. The order of the Chebychev polynomial is determined using an F-test, in order to decide the optimal number of shape parameters to be used in the fit.

Considering n as the degree of a polynomial function, if the pdf of order

$n+1$ does not fit significantly better than the one of order n, the pdf of order $n+1$ is selected and the procedure is iterated at next order. Parameters of the aforementioned functions are allowed to float freely in the fit to data.

Relying on the F-test outcome, for the BDTcat0 category a second order Chebychev function is chosen as nominal fitting function for all the channels in both BDT categories. In order to investigate biases with different background parametrizations, a $n+1$ order Bernstein pdf (where n is the order of the nominal pdf) and an exponential are considered. The results of the fits to sidebands are reported in Fig. 9.3-9.8 with related parameters reported in the plots legend.

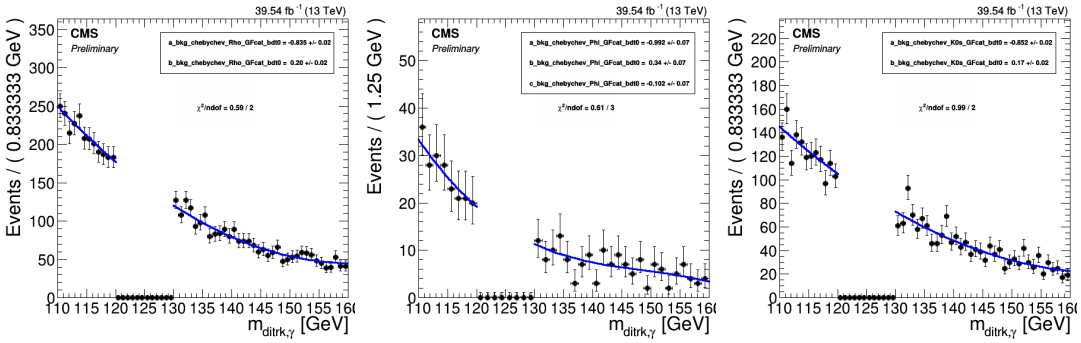

Figure 9.3: Chebychev pdf fit to sidebands of invariant mass spectrum for $\rho\gamma$ channel (left), $\phi\gamma$ channel (middle) and $K_0^*\gamma$ channel (right) for the BDTcat0 category.

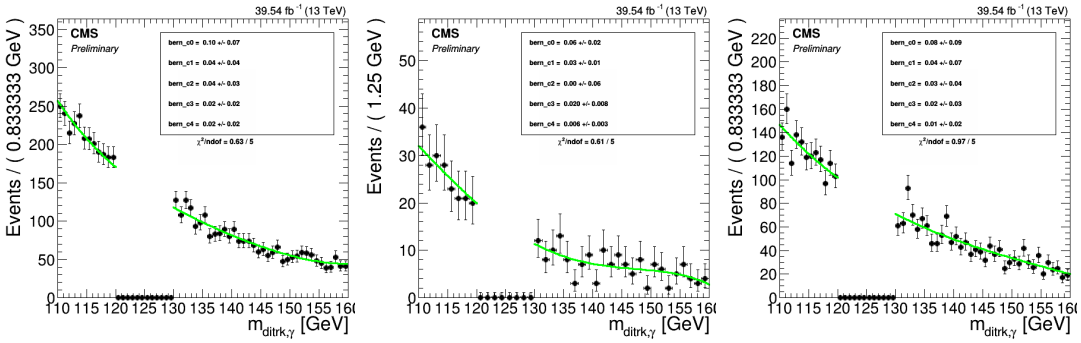

Figure 9.4: Bernstein pdf fit to sidebands of invariant mass spectrum for $\rho\gamma$ channel (left), $\phi\gamma$ channel (middle) and $K_0^*\gamma$ channel (right) for the BDTcat0 category.

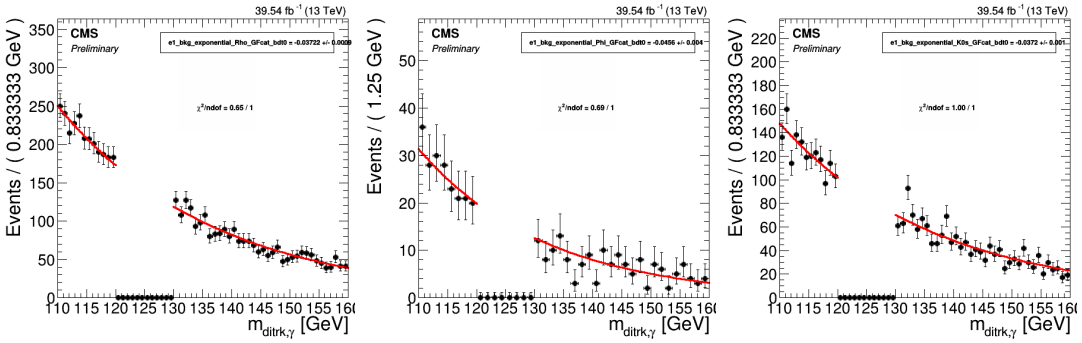

Figure 9.5: Exponential pdf fit to sidebands of invariant mass spectrum for $\rho\gamma$ channel (left), $\phi\gamma$ channel (middle) and $K_0^*\gamma$ channel (right) for the BDTcat0 category.

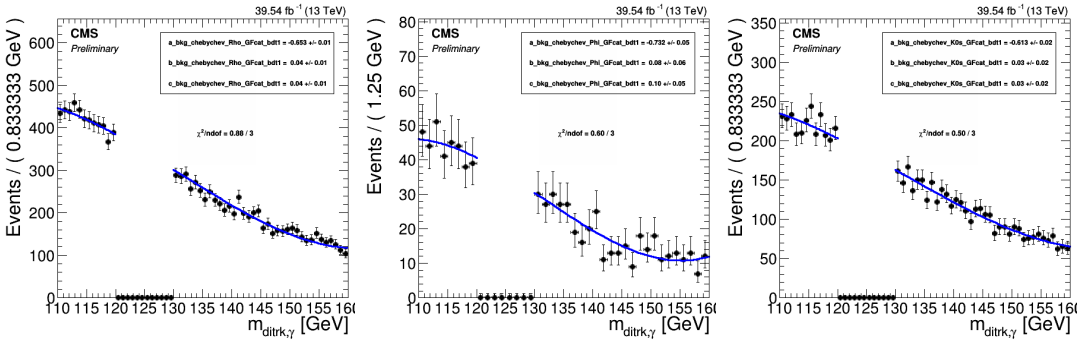

Figure 9.6: Chebychev pdf fit to sidebands of invariant mass spectrum for $\rho\gamma$ channel (left), $\phi\gamma$ channel (middle) and $K_0^*\gamma$ channel (right) for the BDTcat1 category.

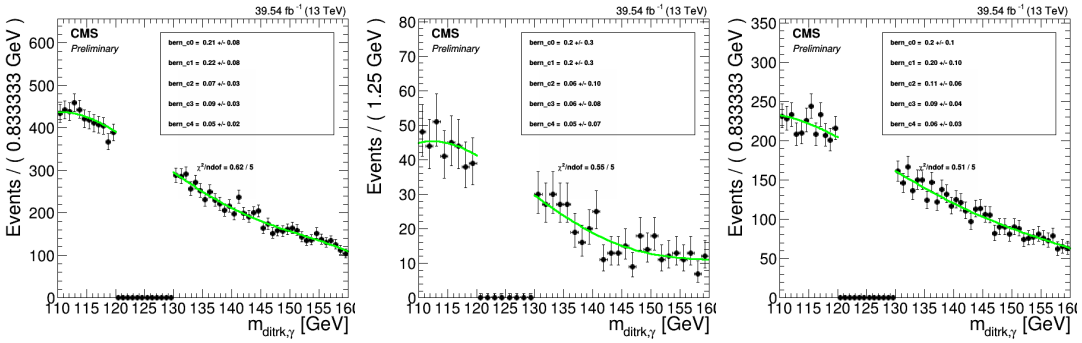

Figure 9.7: Bernstein pdf fit to sidebands of invariant mass spectrum for $\rho\gamma$ channel (left), $\phi\gamma$ channel (middle) and $K_0^*\gamma$ channel (right) for the BDTcat1 category.

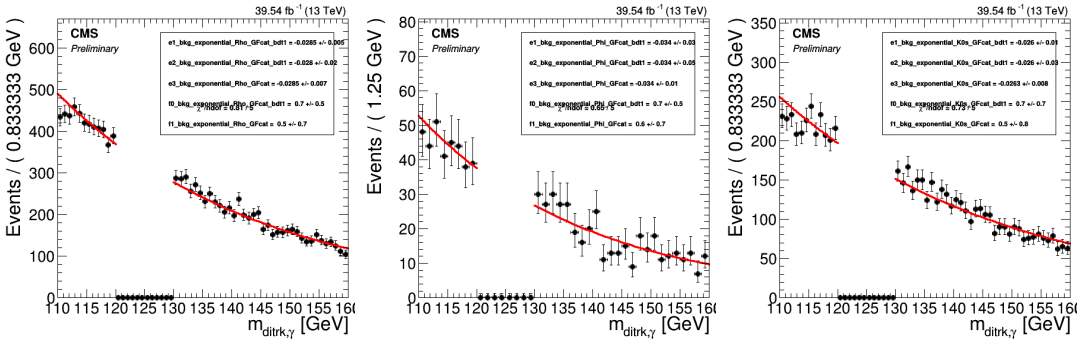

Figure 9.8: Exponential pdf fit to sidebands of invariant mass spectrum for $\rho\gamma$ channel (left), $\phi\gamma$ channel (middle) and $K_0^*\gamma$ channel (right) for the BDTcat1 category.

9.4 Fit Validation

The potential bias due to the choice of the background parametrization is evaluated by using a tailored study. The fit is validated through 5000 pseudo-experiments, known as *Toy-MC*. Toys are built generating events following the distribution of an alternative background model and are fitted through the model for which the potential bias is to be evaluated. For each toy, the invariant mass spectrum is generated according to the total distribution P_{TOT} in Eq. 9.1 and varying the number of signal and background events according to a Poisson fluctuation. This is introduced in order to avoid any biases in the event generation due to correlations of observed events among pseudo-experiments. For each pdf used for the background modeling discussed in Sec. 9.3 the potential bias is evaluated generating events according to a model and fitting For each pseudo-experiment, a fit to the invariant mass spectrum is performed and the branching ratio is extracted with respective uncertainties. In order to detect any bias in the fitted parameters, the "pull" is constructed and defined as

$$\text{pull} = \frac{x_{\text{fit}} - x_{\text{true}}}{\sigma_x}, \tag{9.4}$$

where x_{fit} and σ_x are the fitted parameter and the error on it, and x_{true} is the true value of the parameter of interest. In this case, x_{fit} and σ_x are the $\mathcal{B}$ and its uncertainty extracted from the fit and calculated for each toy, and x_{true} is an arbitrary input value of $\mathcal{B}$, corresponding to 10^{-5}, compatible with the $\mathcal{B}$ extracted by the fit on the unblinded data, reported in the next section. The pull is expected to be compatible with a normal Gaussian centered in 0 and with a width of 1. The pull distribution of the 5000 pseudo-experiment compared with a normal Gaussian is reported in Figs. 9.9-9.10 for some $\phi\gamma$ categories. Pulls for all the categories and channels are reported in Tabs. 9.2-9.4. Pull distributions are reported

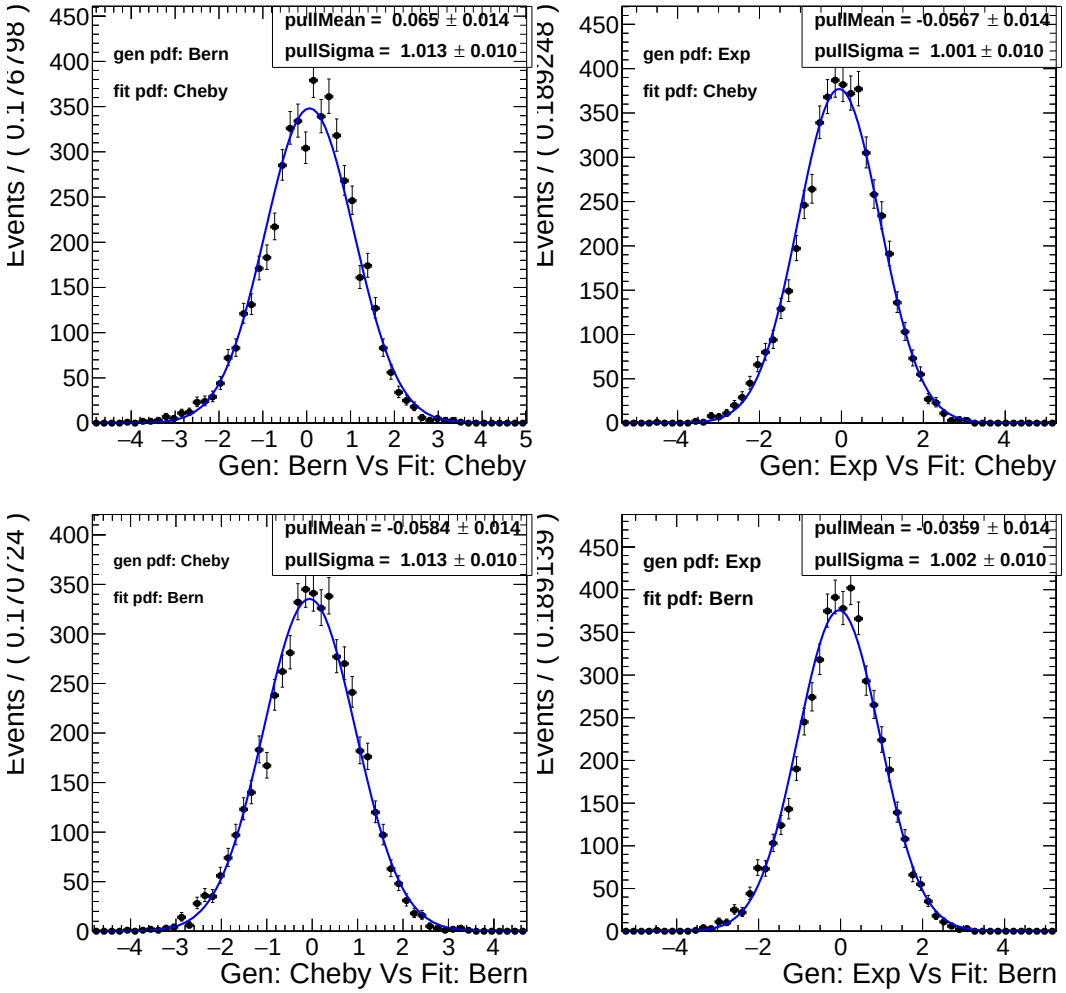

Figure 9.9: Pull distribution for $\mathcal{B} = 10^{-5}$ injected in the ggH BDTcat0 $\phi\gamma$ category, generating toys from a background function and fitting with the same or alternative functions. "Cheby" label refers to the nominal Chebychev function, "Bern" to the alternative Bernstein function, "Exp" to the exponential.

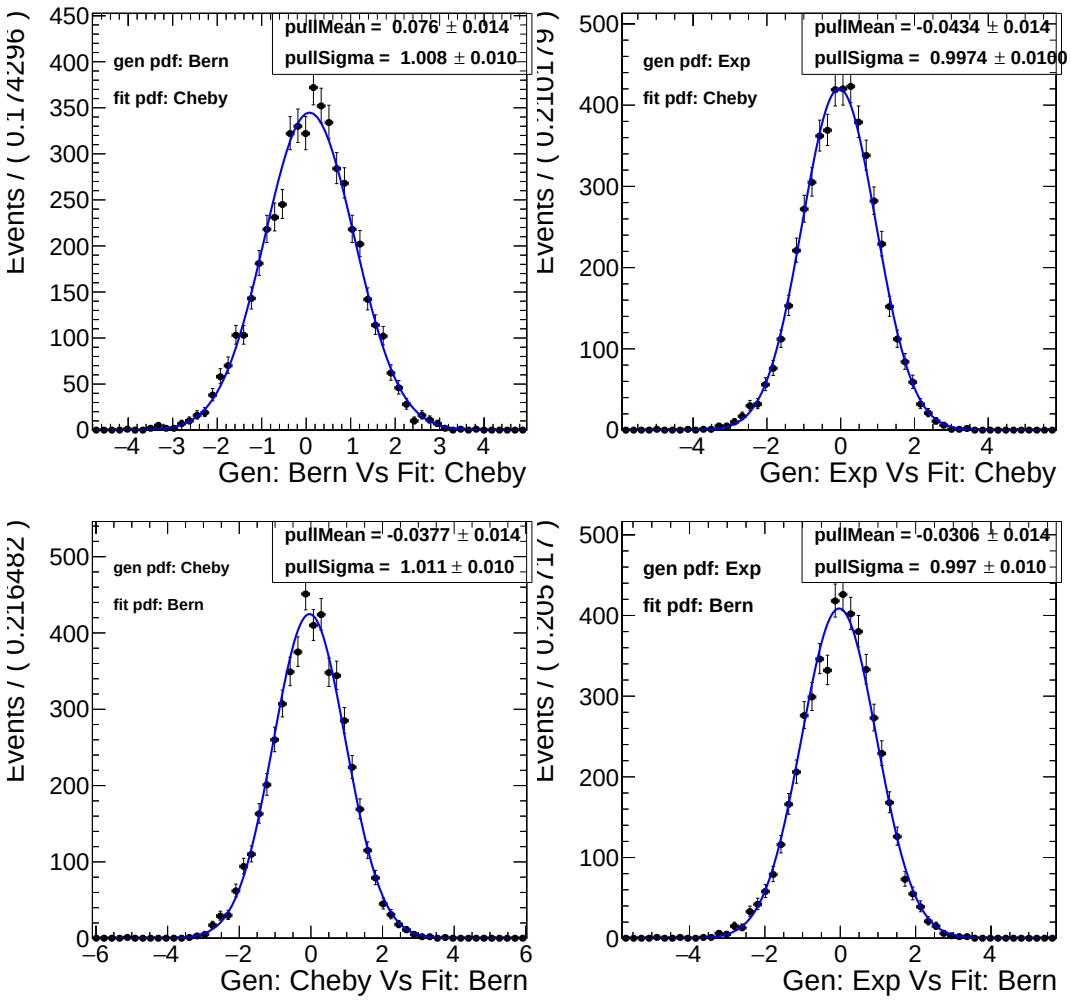

Figure 9.10: Pull distribution for $\mathcal{B} = 10^{-5}$ injected in the ggH BDTcat1 $\phi\gamma$ category, generating toys from a background function and fitting with the same or alternative functions. "Cheby" label refers to the nominal Chebychev function, "Bern" to the alternative Bernstein function, "Exp" to the exponential.

	C Vs B	C Vs E	B Vs C	B Vs E	E Vs C	E Vs B
ggH BDTcat0	5.1 %	7.4 %	6.1 %	4.1 %	5.2 %	3.4 %
ggH BDTcat1	4.5 %	10.8 %	9.6 %	4.0 %	3.8 %	10.0 %
VBF high-p_T^γ BDTcat0	9.1 %	–	2.9 %	–	–	–
VBF high-p_T^γ BDTcat1	3.2 %	–	5.5 %	–	–	–
VBF low-p_T^γ BDTcat0	6.1 %	–	6.1 %	–	–	–
VBF low-p_T^γ BDTcat1	7.2 %	–	3.8 %	–	–	–
VH	3.0 %	–	6.8 %	–	–	–

Table 9.2: The results of the bias studies across all categories in $\rho\gamma$ channel. The employed notation – "C" for Chebychev polynomial, "B" for Bernstein polynomial, and "E" for exponential function – refers to the generating function versus the fitting function bias.

	C Vs B	C Vs E	B Vs C	B Vs E	E Vs C	E Vs B
ggH BDTcat0	5.8 %	6.8 %	6.5 %	7.1 %	5.7 %	3.6 %
ggH BDTcat1	3.8 %	5.8 %	7.6 %	4.8 %	4.3 %	3.1 %
VBF high-p_T^γ BDTcat0	5.1 %	–	7.1 %	–	–	–
VBF high-p_T^γ BDTcat1	4.8 %	–	6.2 %	–	–	–
VBF low-p_T^γ BDTcat0	7.0 %	–	5.4 %	–	–	–
VBF low-p_T^γ BDTcat1	3.4 %	–	5.1 %	–	–	–
VH	3.2 %	–	4.0 %	–	–	–

Table 9.3: The results of the bias studies across all categories in $\phi\gamma$ channel. The employed notation – "C" for Chebychev polynomial, "B" for Bernstein polynomial, and "E" for exponential function – refers to the generating function versus the fitting function bias.

	C Vs B	C Vs E	B Vs C	B Vs E	E Vs C	E Vs B
ggH BDTcat0	4.2 %	8.4 %	5.6 %	4.6 %	10.7 %	6.4 %
ggH BDTcat1	3.9 %	8.1 %	7.8 %	4.0 %	7.5 %	2.2 %
VBF high-p_T^γ BDTcat0	6.3 %	–	5.5 %	–	–	–
VBF high-p_T^γ BDTcat1	6.1 %	–	2.8 %	–	–	–
VBF low-p_T^γ BDTcat0	11.3 %	–	6.7 %	–	–	–
VBF low-p_T^γ BDTcat1	5.1 %	–	9.1 %	–	–	–
VH	3.9 %	–	5.0 %	–	–	–

Table 9.4: The results of the bias studies across all categories in $K^{*0}\gamma$ channel. The employed notation – "C" for Chebychev polynomial, "B" for Bernstein polynomial, and "E" for exponential function – refers to the generating function versus the fitting function bias.

Systematic Uncertainties 10

This chapter presents the systematic uncertainties impacting the measurement of $\mathcal{B}(H \to \mathcal{M}\gamma)$, delineating the estimation methods of these uncertainties and their consequent effects on the outcomes.

10.1 Nuisance parameters

Previously, in Chap. 9, the process of deriving parameter values for the pdf to match the $m_{\text{ditrk}\gamma}$ distribution within the data SR was detailed. This technique relies on the minimization of the negative log-likelihood based on the pdf.

For a more straightforward explanation of this method, the likelihood function $L(x;\theta_i)$ for an observable x, encompassing a solitary parameter θ_i, is considered. Assuming the optimal value $\hat{\theta}_i$, which maximizes the likelihood, and its corresponding uncertainty σ_{θ_i}, are known, an auxiliary parameter can be introduced:

$$k = 1 + \frac{\sigma_{\hat{\theta}_i}}{\hat{\theta}_i}. \tag{10.1}$$

The aforementioned expression is infused into the definition of the signal event count as follows:

$$N_{\text{sig}} = \sigma^{H}_{13\text{TeV}} \cdot \mathcal{B}(H \to \mathcal{M}\gamma) \cdot \mathcal{B}(\mathcal{M} \to \text{trk}^{+}\text{trk}^{-}) \cdot \mathcal{L}_{int} \cdot \epsilon \cdot k^{\beta}, \tag{10.2}$$

with β representing an arbitrary parameter. The remaining components of this formula are elaborated upon succeeding Eq. 4.1. Given these conditions, one can formulate a Gaussian pdf $G(\beta;0,1)$ characterized by the variable β as

the observable, a mean of 0 and a standard deviation of 1. Subsequently, the likelihood $L(x;\theta_i)$ is combined with $\mathcal{G}(\beta;0,1)$ to yield:

$$L(x;\theta_i,\sigma_{\theta_i},\beta) = L(x;\theta_i)\cdot\mathcal{G}(\beta;0,1). \tag{10.3}$$

The revised likelihood function applies a Gaussian correction to encapsulate the systematic uncertainty related to a particular model parameter and its effect on the parameter of interest, namely the $H \to \mathcal{M}\gamma$ branching fraction. It is crucial to note that this modality leaves the parameter $\hat{\theta}_i$ unaltered. The mode of integration for each nuisance parameter within the likelihood function is expounded in the subsequent sections.

10.2 Source of systematic uncertainties

Several sources of systematic uncertainties have been considered. The way these systematics are assigned to the cross sections, integrated luminosity, efficiencies, signal and background parametrization is discussed in this section. As the background is modelled using analytic functions, the parameters of the functions as well as the normalisation are left to float freely in the fit. In order to estimate systematic uncertainties on this analytical shapes, a discrete profile method is used, described in Sec. 10.2.11. In addition, several systematic uncertainties affect the normalization of the simulated signal templates. The impact of these uncertainties on the $m_{\text{ditrk}\gamma}$ lineshape is negligible and they are all modelled via a log-normal nuisance parameter.

10.2.1 QCD scale uncertainties

Scale uncertainties are estimated by varying the renormalization (μ_R) and factorization (μ_F) scales between 0.5 and 2 times their default value m_H. Notably, for ggH process, the choice of μ_R and μ_F can lead to significant differences in the distributions. For VBF and VH, the effect is smaller but still non-negligible. The typical procedure for estimating scale uncertainties involves taking half of the maximum differences in acceptance among all the scale choices. However, since the largest difference is in all cases between the scenarios where $\mu_R = \mu_F = 2$ and $\mu_R = \mu_F = 0.5$, the uncertainty is specifically computed as half the difference in acceptance between these two scale choices. Using this procedure, theoretical uncertainties from the choice of QCD renormalization and factorization scales

in the ggF production cross section amount to 3.9%, with uncertainties in the VBF, WH, ZH, and ttH production cross sections being, respectively, 0.4, 0.7, 3.8, and 2.6% [7].

10.2.2 PDF+α_S uncertainty

The overall uncertainty for PDF (Parton Distribution Function) plus α_S (strong coupling constant) is calculated by summing the individual PDF and α_S uncertainties in quadrature. For MC samples of the signal, specifically for ggH and VBF productions, the NNPDF3.1 PDF set [59] is used. The signal samples include weights for both the default PDF and its error set, comprising 100 parameter variations, known collectively as the PDF members. The PDF uncertainty is estimated by calculating the standard deviation of the acceptances resulting from reweighting the signal to each of the members. The uncertainty arising from the value of α_S, the strong coupling constant, is estimated by altering α_S from its default value of 0.118 to both 0.116 and 0.120. The uncertainty in acceptance is then calculated as half the difference in the acceptances resulting from these altered α_S values. This calculated uncertainty is subsequently scaled down by a factor of 0.75. This scaling is done to align with the PDF4LHC's recommended one standard deviation uncertainty on α_S of 0.0015 [72].

10.2.3 Luminosity uncertainty

The uncertainty in the measured integrated luminosity is determined through dedicated Van-der-Meer scans and by assessing the stability of the detector response during data-taking [73]. The Van-der-Meer method allows for a minimization of an unwanted separation by transversally scanning one beam through the other. The beam sizes at the interaction point can also be determined by this method and used to give an absolute measurement of the luminosity. The uncertainty values are specific to each dataset year: for the 2016 dataset [74], the uncertainty is 2.5%; for 2017 [75], it is 2.3%; and for 2018 [76], the uncertainty is 2.5%. These uncertainties are partially correlated among the datasets of the three years and applicable to all signals.

10.2.4 Pile-up uncertainty

The uncertainty associated with the PU reweighting originates from the uncertainty in the inelastic proton-proton total cross section. This uncertainty is quantified as 4.6%. This value is then propagated to the PU weight, leading to the to the generation of its upward and downward variations. Consequently, the resulting systematic uncertainty in the PU reweighting is estimated to be approximately 1%.

10.2.5 Di-track isolation uncertainty

Uncertainties in the charged and neutral di-track isolation efficiency, computed as the maximum observed difference between the efficiency as measured with the $Z \to \mu\mu$ tag-and-probe and the efficiency derived from the signal samples (Fig. 8.6). These uncertainties amount to 1.5 % for the $\rho\gamma$ channel, to 1.2 % for the $\phi\gamma$ channel and to 1.1 % for the $K^{*0}\gamma$ channel.

10.2.6 Jet energy scale and resolution uncertainties

The energy scale of jets is measured using the transverse momentum balance technique. This technique involves jets with Z bosons and photons in $Z \to e^+e^-$, $Z \to \mu^+\mu^-$, and γ+jets events, as well as the p_T balance between jets in dijet and multijet events [77]. The uncertainty in the jet energy scale is typically a few percent, depending on the p_T and pseudorapidity of the jet. To evaluate the effect of jet energy scale uncertainties on event yields, the jet energy corrections are varied within their uncertainties, and the impact is then propagated to the final result. The impact of these uncertainties is not negligible for categories targeting VBF, where it is around 3.5%. For the ggH category it amounts to less than 1%.

10.2.7 Photon identification uncertainty

Photon mvaID uncertainty is derived from $Z \to e^+e^-$ events and their uncertainty is propagated to the signal efficiency [64]. The uncertainties are kinematic dependent and amount to up to 1.5%.

10.2.8 Lepton identification uncertainty

Uncertainties in the muon and electron identification for the VH category, isolation, and trigger efficiency measurements arise from the method used to measure the efficiency and from the limited size of the simulated samples used for the measurement in simulation, and they amount to less than 1.0% (1.5%) for muons (electrons) [78, 64].

10.2.9 Tracking efficiency uncertainty

The uncertainty in the tracking efficiency amounts to 4.6-4.8% (corresponding to 2.3-2.6% per track), depending on the data-taking period. This uncertainty is determined by comparing ratios of D^* meson decay products and tracker-only muons from $Z \rightarrow \mu^+\mu^-$ events in data and simulation [79].

10.2.10 Trigger efficiency uncertainty

Uncertainties in the efficiency of the dedicated trigger are computed by factorizing the trigger efficiency into the photon and τ-like jet parts. Independent data-to-simulation corrections are computed, as outlined in Sec. 8.1, whose uncertainties amount to 2.2-3.4% for the photon part and 5.3-5.6% for the jet part, slightly different in the ggF and VBF categories.

10.2.11 Uncertainty due to the choice of the background model

When analyzing scenarios where a small signal is superimposed on a large background, even minor alterations to the background shape can substantially influence the perceived magnitude and position of the signal. In cases where there is no robust theoretical or simulation-based framework to constrain the background shape, a degree of uncertainty arises regarding the selection of an appropriate function for background parameterization. Different choices of the functional form for background modeling can lead to varying results in the determined signal parameters. Consequently, this variability introduces a systematic uncertainty that is inherently linked to the choice of the function used for background parameterization.

The technique of selecting various sets of nuisance parameters and constructing an envelope can be conceptually applied to the uncertainty associated with the functional form of the background. In this method, each background function under consideration is assigned a unique integer label. This integer then serves as a discrete nuisance parameter within the profile likelihood calculation. Consequently, this approach is defined *discrete profiling*. The minimum of the envelope generated by considering all these functions provides the overall profile curve. This envelope inherently accounts for any systematic error stemming from the choice of the background function. This is because the envelope, by its nature, tends to be broader than any of the individual curves contributing to it, thus encompassing the uncertainty associated with the function selection.

10.3 Impact of systematic uncertainties

The impact of the largest systematic uncertainties on the observed $H \to \mathcal{M}\gamma$ branching fraction are shown in Figs. 10.1, 10.2, 10.3. The uncertainties with the largest impact come from the choice of the alternative PDFs used as background model, as well as those from the trigger efficiency corrections. No significant pulls away from zero are observed. The right-hand side of impacts plots shows the observed impacts for small, in this case non-zero, values of $\Delta\hat{r}$, which corresponds in the plot to the branching fraction. The left-hand side displays the pull quantity $(\theta - \theta_0)/\Delta\theta$, where θ and θ_0 are post-fit and pre-fit nuisance parameter values, and $\Delta\theta$ is the pre-fit uncertainty.

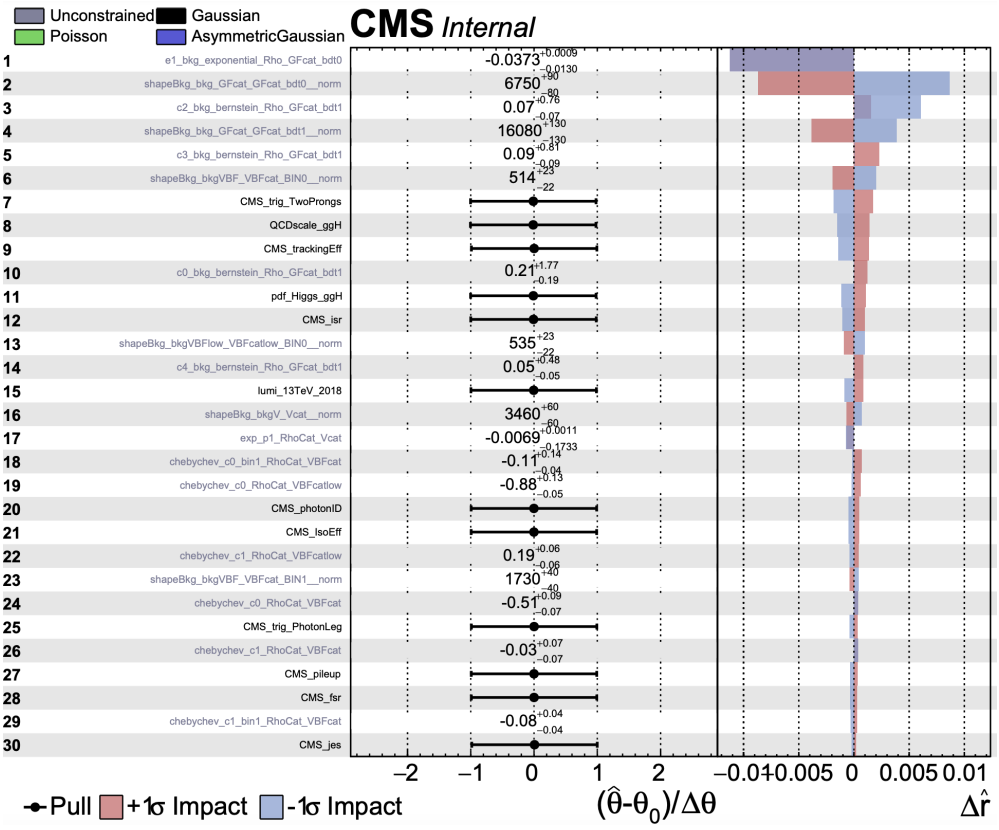

Figure 10.1: Impact of systematic uncertainties for the $\rho\gamma$ channel. The right-hand side of impacts plots shows the observed impacts for small, in this case non-zero, values of $\Delta\hat{r}$, which corresponds in the plot to the branching fraction. The impacts on $\Delta\hat{r}$ must be multiplied by 10^{-2}. The left-hand side displays the "pull" quantity $(\theta - \theta_0)/\Delta\theta$, where θ and θ_0 are post-fit and pre-fit nuisance parameter values, and $\Delta\theta$ is the pre-fit uncertainty. The rows labeled as "shapeBkg" represent the observed background yields per category with corresponding uncertainties.

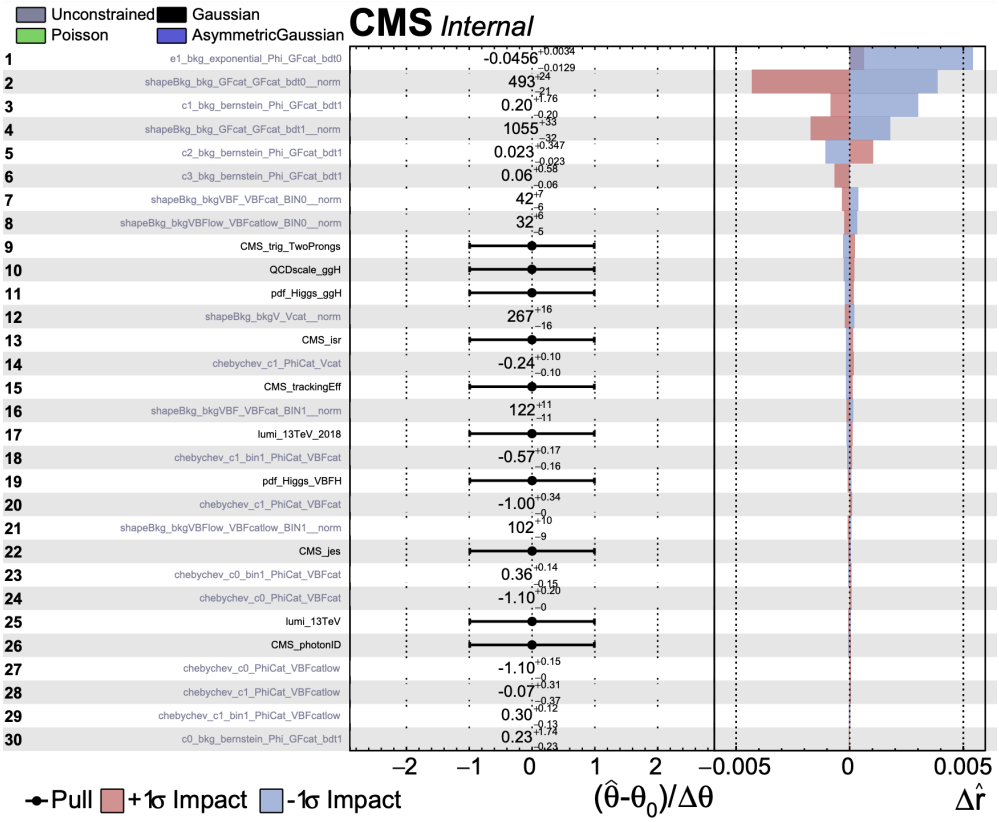

Figure 10.2: Impact of systematic uncertainties for the $\phi\gamma$ channel. The right-hand side of impacts plots shows the observed impacts for small, in this case non-zero, values of $\Delta\hat{r}$, which corresponds in the plot to the branching fraction. The impacts on $\Delta\hat{r}$ must be multiplied by 10^{-2}. The left-hand side displays the "pull" quantity $(\theta - \theta_0)/\Delta\theta$, where θ and θ_0 are post-fit and pre-fit nuisance parameter values, and $\Delta\theta$ is the pre-fit uncertainty. The rows labeled as "shapeBkg" represent the observed background yields per category with corresponding uncertainties.

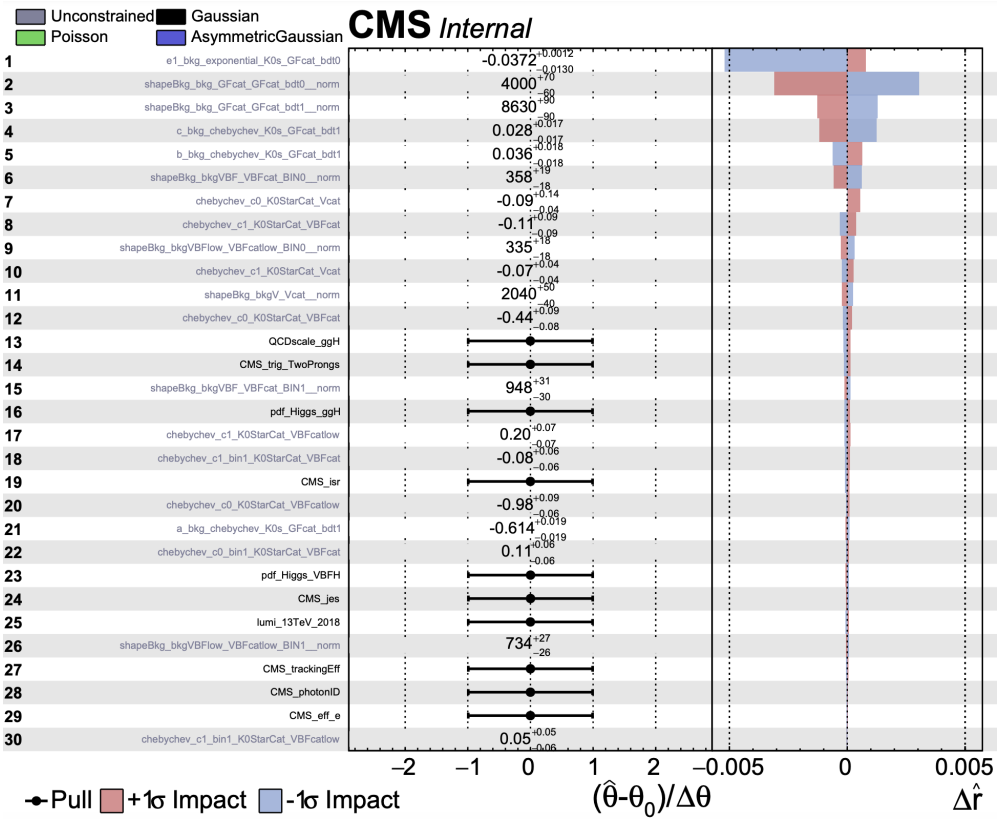

Figure 10.3: Impact of systematic uncertainties for the $K^{*0}\gamma$ channel. The right-hand side of impacts plots shows the observed impacts for small, in this case non-zero, values of $\Delta\hat{r}$, which corresponds in the plot to the branching fraction. The impacts on $\Delta\hat{r}$ must be multiplied by 10^{-2}. The left-hand side displays the "pull" quantity $(\theta - \theta_0)/\Delta\theta$, where θ and θ_0 are post-fit and pre-fit nuisance parameter values, and $\Delta\theta$ is the pre-fit uncertainty. The rows labeled as "shapeBkg" represent the observed background yields per category with corresponding uncertainties.

Results 11

Since the sensitivity of the analysis is much lower than the SM prediction, the reported results set upper limits on the branching ratios for $H \to \rho/\phi/K^{*0}\gamma$ decays. This chapter aims to provide a hypothesis testing, addressing the question of the level of compatibility of the observation with the background-only hypothesis. An upper limit on the signal branching ratio in the scenario where the presence of signal is permitted is also estimated. Additionally, this chapter details the process of "unblinding". This critical step involves revealing the data that has been hidden during the initial phases of analysis.

11.1 The unblinding procedure

As said, in a search of Higgs boson decay, the technique of blinding the signal region in the invariant mass distribution of data sample is an approach necessary to ensure that the researcher does not induce any bias by optimising the analysis based on what was already seen, i.e. manipulating the selection criteria to create an artificial increase in events near the expected rest mass of the Higgs boson. Once satisfied with the selection procedure and the fit validation, the researcher can then proceed to reveal the data in the blind region. This step is known as "unblinding", where the actual results are finally observed.

11.1.1 Goodness-of-fit

During the unblinding process, a crucial step is to evaluate how compatible the observed data are with the model pdf. This evaluation is known as the Goodness-of-fit (GOF) and is conducted via a hypothesis test that employs likelihood ratios. The Neyman-Pearson lemma [80] is applied to optimize the

discriminating power of the test and the saturated model [81] of the GOF is used to compute a p-value, running on 500 toy MC. The p-values, listed in Tab. 11.1, measure the adequacy of the parameters derived from the fit in describing the observed data.

channel	p-value
$H \to \rho\gamma$	0.27
$H \to \phi\gamma$	0.70
$H \to K^{*0}\gamma$	0.65

Table 11.1: p-values corresponding to the Goodness of fit tests for each channel.

11.1.2 Post-fit distributions

In this section, post-fit results are reported. Table 11.2 shows the expected and observed number of events of signal and data samples for the most sensitive category of this analysis. Fits to unblinded background only spectra for the most sensitive category are reported in Figs. 11.1, 11.2, 11.3, while postfits to the other categories are shown in Figs. 11.4, 11.5, 11.6. The $m_{\mathrm{ditrk}\gamma}$ distributions in data and the background model with signal and background fit components are shown. No significant excess above the background expectation is observed in either of the three searches.

BDTcat0 ggH	obs. yields (exp. background)	exp. signal yields
	$110 < m_{\mathrm{ditrk}\gamma} < 160$ GeV	($\mathcal{B} = 10^{-4}$)
$H \to \rho\gamma$	6714 (6745 ± 78)	4.6 ± 0.1
$H \to \phi\gamma$	493 (492 ± 22)	9.0 ± 0.1
$H \to K^{*0}\gamma$	3999 (4002 ± 62)	9.1 ± 0.1

Table 11.2: The number of observed events and the expected background yields. The expected Higgs boson signal yields for ggH BDTcat0, estimated using simulations, are also shown.

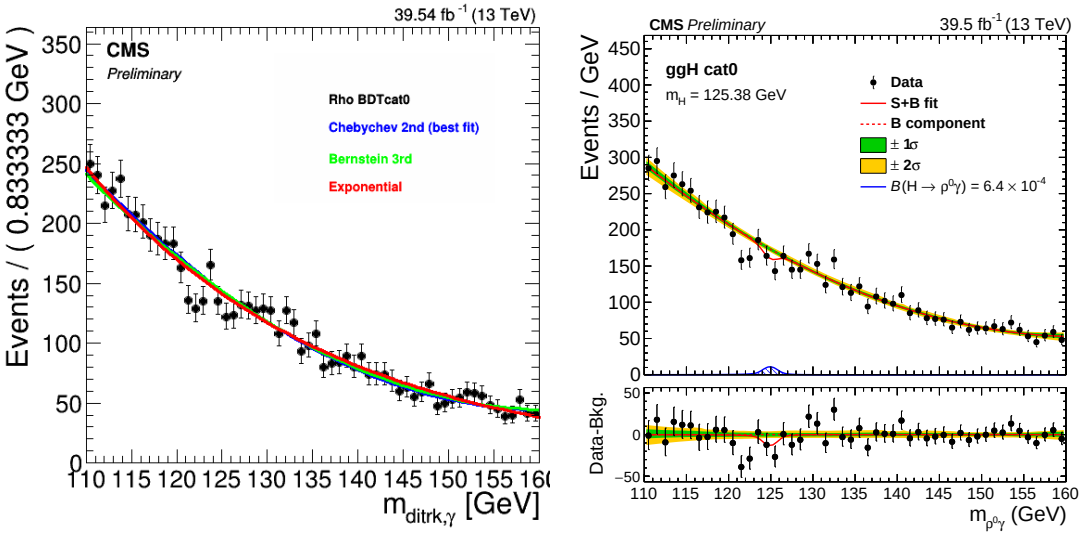

Figure 11.1: Left: $m_{\rho\gamma}$ background-only fits with nominal and alternative pdfs for the ggH BDTcat0 category. Right: $m_{\rho\gamma}$ distribution in data and the background model for the ggH BDTcat0 category with signal and background fit components and 1- and 2-σ fit uncertainty.

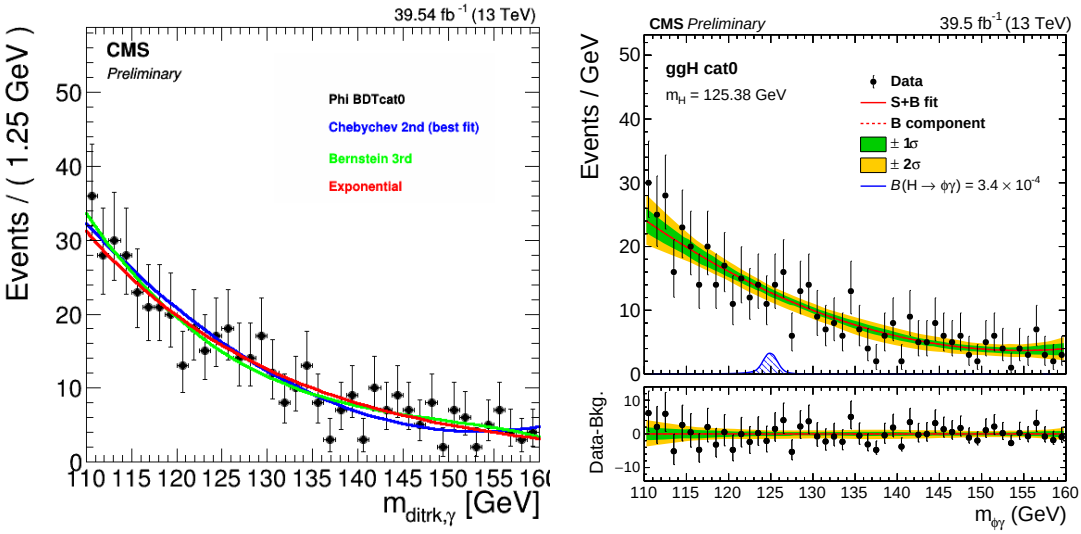

Figure 11.2: Left: $m_{\phi\gamma}$ background-only fits with nominal and alternative pdfs for the ggH BDTcat0 category. Right: $m_{\phi\gamma}$ distribution in data and the background model for the ggH BDTcat0 category with signal and background fit components and 1- and 2-σ fit uncertainty.

11.2 Hypothesis testing and CL$_s$ method

In physics, a *test statistic* is a variable computed from a sample that discriminates between two hypotheses H_0 and H_1. In general, one of these hypotheses repre-

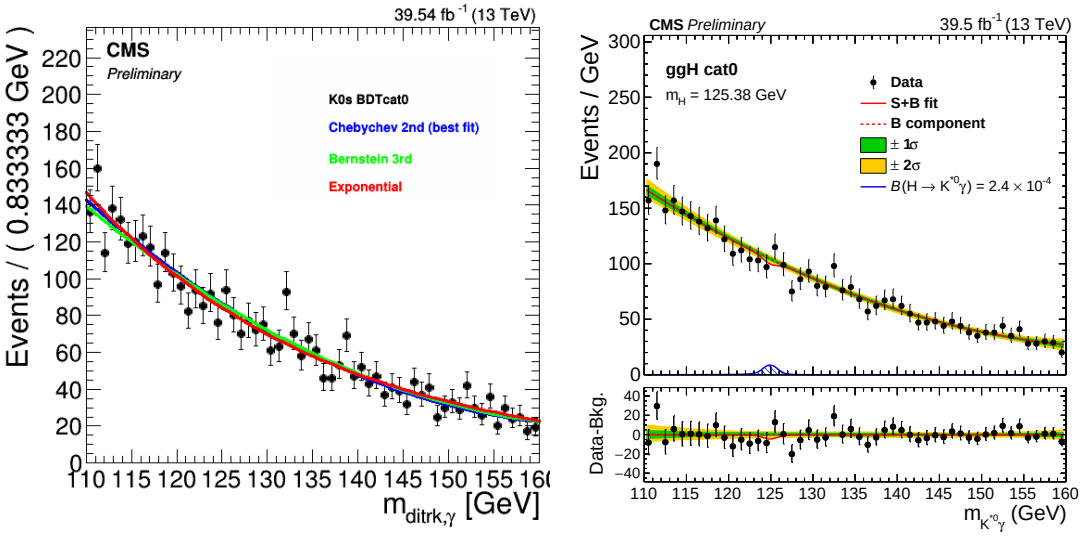

Figure 11.3: Left: $m_{K^{*0}\gamma}$ background-only fits with nominal and alternative pdfs for the ggH BDTcat0 category. Right: $m_{K^{*0}\gamma}$ distribution in data and the background model for the ggH BDTcat0 category with signal and background fit components and 1- and 2-σ fit uncertainty.

sents the *background-only* hypothesis and one represents the *signal + background* hypothesis. The following quantities are useful to give quantitative information about a test:

- α, the significance level: probability to reject H_0, if H_0 is assumed to be true (type I error, or *false negative*).
- the p-value : probability to observe at least n_{obs} events if the null hypothesis H_0 is true.

The profile likelihood approach used in this analysis is based on the test statistic built as the following likelihood ratio for a parameter of interest μ:

$$\lambda(\mu) = \frac{\mathcal{L}(\mu; \hat{\hat{\theta}})}{\mathcal{L}(\hat{\mu}; \hat{\theta})}, \tag{11.1}$$

where at the denominator both μ and θ are fitted simultaneously as $\hat{\mu}$ and $\hat{\theta}$, respectively, and at the numerator $\hat{\hat{\theta}}$ is the best fit of θ for a given value of μ. The motivation for the choice for the likelihood ratio $\lambda(\mu)$ as the test statistic comes from Wilks' theorem that allows to approximate asymptotically the distribution of the q-ratio, defined by

$$q_\mu = -2 \ln \lambda(\mu) \tag{11.2}$$

as a χ^2 distribution. Assuming $\mu = 0$ (null hypothesis), the quantity $q_0 = -2\ln\lambda(0)$ can be approximated with a χ^2 distribution having one degree of freedom. Therefore, the significance can be approximately evaluated as

$$Z \sim \sqrt{q_0}. \tag{11.3}$$

It is possible to compute a p-value equal to the probability that q_0 is greater or equal to than the value $q_{0,\text{obs}}$ observed in data. Such p-value is usually converted into an equivalent probability computed as the area under the rightmost tail of a standard normal distribution (as shown in Fig. 11.7):

$$p = \int_{q_{0,\text{obs}}}^{\infty} f(q_0|0)dq_0 = \int_{Z}^{\infty} \frac{1}{\sqrt{2\pi}} e^{-x^2/2}dx = 1 - \Phi(Z), \tag{11.4}$$

where Φ is the cumulative of a standard normal distribution.

In this section, the Confidence Level signal (CL_s) method for the upper limit calculation is proposed. This statistical method, developed for the combination of the results of searches for the Higgs boson by the four LEP experiments, ALEPH, DELPHI, L3 and OPAL [82], is a particular form of interval estimation, useful for cases in which a small signal can be expected over a large background, and is commonly used in searches at LHC. If the number of signal events of a given model is very small, one can be leaded to an erroneous exclusion of models to which underlying analysis is not sensitive. The CL_s method can avoid this issue. The CL_s estimator can be defined as a likelihood ratio

$$q = \frac{\mathcal{L}(s+b)}{\mathcal{L}(b)},$$

where b represents the background and s the signal and $\mathcal{L}$ is the likelihood function.
CL_s is defined as

$$CL_s = \frac{CL_{s+b}}{CL_b} = \frac{P(q_{s+b} \leqslant q_{\text{obs}})}{P(q_b \leqslant q_{\text{obs}})} = \frac{p_{s+b}}{1-p_b},$$

where

- p_{s+b} is the probability to obtain a result which is less compatible with the signal plus background than the observed result, assuming the signal hypothesis
- p_b is the probability to obtain a result less compatible with the background-only hypothesis than the observed one, assuming a background only scenario.

If the distributions the test statistics for the H_0 and H_1 hypotheses are well separated, the value $(1 - p_b) = \mathrm{CL}_b$ is close to 1, and has a little impact on the exclusion power (Fig. 11.8, left). In this case, the CL_s method approximates the estimation done using CL_{s+b}. If the two distribution largely overlap, CL_s value is close to 1, leading to a non-exclusion of the signal model (Fig. 11.8, right). The CL_s definition as a fraction of CL_{s+b} and CL_b allows to prevents CL_s to become too small and to reject cases where the experiment has little sensitivity.
The upper limit is set requiring

$$\mathrm{CL}_s \leq \alpha,$$

where the value of α used for this analysis is 0.05.

The next section reports the final result of this thesis work, consisting in the determination of the $\mathcal{B}(H \to \mathcal{M}\gamma)$ upper limit, using the CL_s method described above.

11.3 Upper limits

95% CL upper limits on the branching are derived from scans of the profile-likelihood ratio described in this chapter, where it is assumed that $\mathcal{B}(\rho \to \pi^+\pi^-) = \mathcal{B}(K^{*0} \to K^\pm\pi^\mp) = 100\%$, while $\mathcal{B}(\phi \to K^+K^-) = (49.1 \pm 0.5)\%$ [71]. For the $H \to K^{*0}\gamma$ search, the charge conjugate $\overline{K}^{*0}$ is implict in the results, as the analysis is entirely symmetric under charge conjugation.

Figure 11.9 reports the expected and observed 95% CL upper limits in a breakdown by analysis categories, where the two BDT-based sub-categories of ggH and VBF are merged. The ggF channel dominates the search sensitivity for all channels. In combination, the observed upper limits on $\mathcal{B}(H \to \rho\gamma)$, $\mathcal{B}(H \to \phi\gamma)$ and $\mathcal{B}(H \to K^{*0}\gamma)$, denoting the sum of $H \to K^{*0}(892)\gamma$ and $H \to \overline{K}^{*0}(892)\gamma$ decays, are $3.74 \cdot 10^{-4}$, $2.97 \cdot 10^{-4}$ and $1.71 \cdot 10^{-4}$, respectively. These values correspond to 24 times the SM expectation for the $H \to \rho\gamma$ decay and 129 times the SM expectation for the $H \to \phi\gamma$ decay, while no calculation is available for the SM branching ratio of $H \to K^{*0}\gamma$. These limits can be compared with the expected upper limits, which are $5.7 \cdot 10^{-4}$ or 35 times the SM expectation for $\mathcal{B}(H \to \rho\gamma)$, $2.9 \cdot 10^{-4}$ or 129 times the SM expectation for $\mathcal{B}(H \to \phi\gamma)$, and $2.1 \cdot 10^{-4}$ for $\mathcal{B}(H \to K^{*0}\gamma)$. The observed and median expected upper limits (U.L.) for the branching fractions at 95% CL for the Higgs boson decays are listed in Tab. 11.3.

	U.L. $\mathcal{B}(H \to \rho\gamma)$		U.L. $\mathcal{B}(H \to \phi\gamma)$		U.L. $\mathcal{B}(H \to K^{*0}\gamma)$	
category	Exp.(10^{-4})	Obs.(10^{-4})	Exp.(10^{-4})	Obs.(10^{-4})	Exp.(10^{-4})	Obs.(10^{-4})
VH	$62.3^{+25.6}_{-17.9}$	73.7	$37.3^{+16.9}_{-11.3}$	45.0	$25.3^{+11.4}_{-7.3}$	48.5
low-p_T^γ VBF	$49.6^{+22.5}_{-15.0}$	35.6	$33.1^{+18.7}_{-11.5}$	27.9	$18.8^{+8.90}_{-5.7}$	12.3
high-p_T^γ VBF	$22.9^{+10.5}_{-6.9}$	16.0	$16.0^{+9.0}_{-5.5}$	10.7	$9.13^{+4.25}_{-2.75}$	6.66
ggH	$6.01^{+2.53}_{-1.72}$	4.37	$3.08^{+1.33}_{-0.98}$	3.46	$2.20^{+0.94}_{-0.62}$	1.93
combined	$5.71^{+2.37}_{-1.63}$	3.74	$2.88^{+1.33}_{-0.83}$	2.97	$2.10^{+0.90}_{-0.58}$	1.71

Table 11.3: U.L. at 95% CL on the branching fractions of the H boson decays. Observed and median expected limits with the upper and lower bounds in the expected 68% CL intervals are reported.

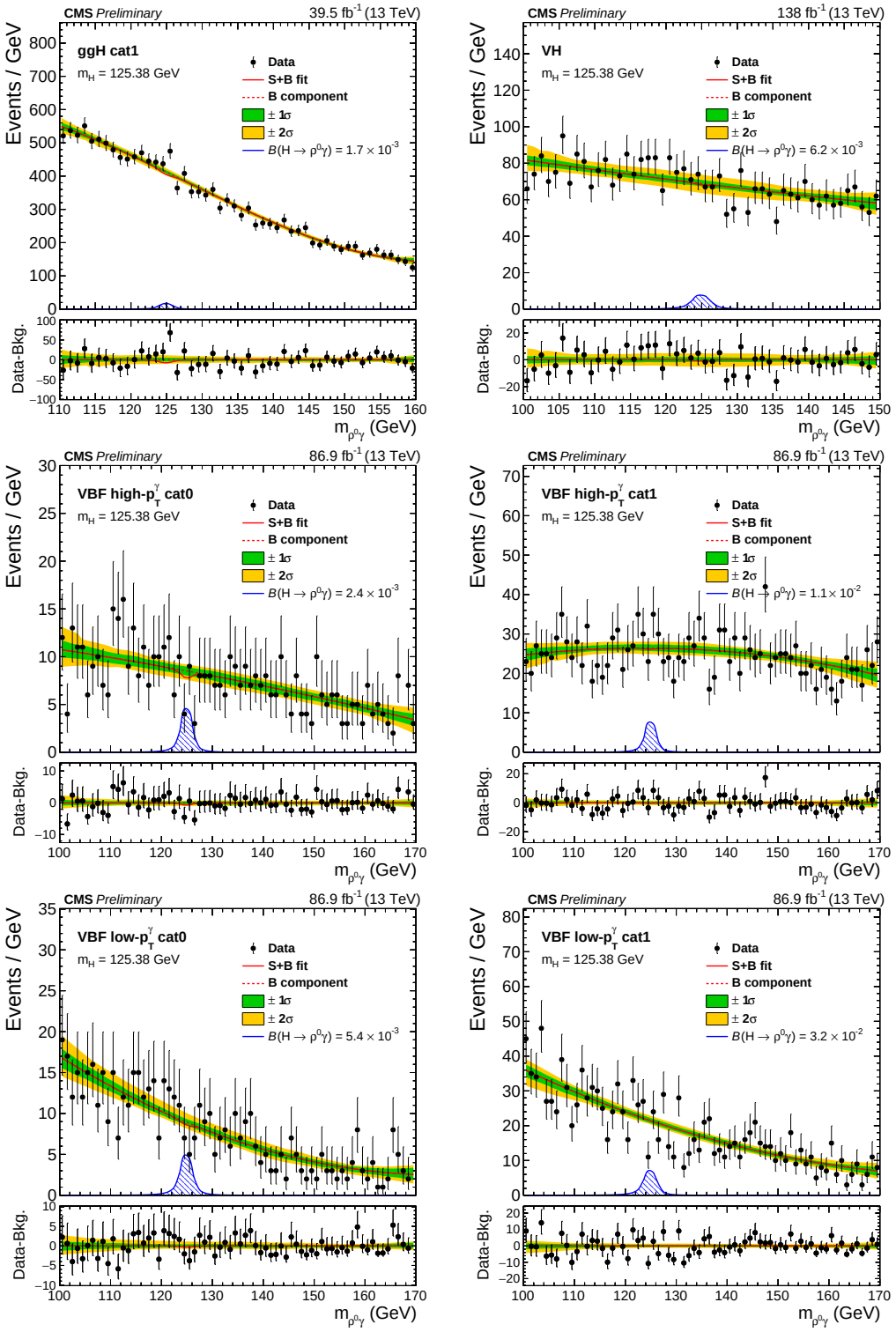

Figure 11.4: $\rho\gamma$ distribution in data and the background model with signal and background fit components and 1- and 2-σ fit uncertainty for the ggH BDTcat1 (top-left), VH (top-right), VBF high-p_T^γ BDTcat0 (middle-left), VBF high-p_T^γ BDTcat1 (middle-right), VBF low-p_T^γ BDTcat0 (bottom-left), VBF low-p_T^γ BDTcat1 (bottom-right) categories.

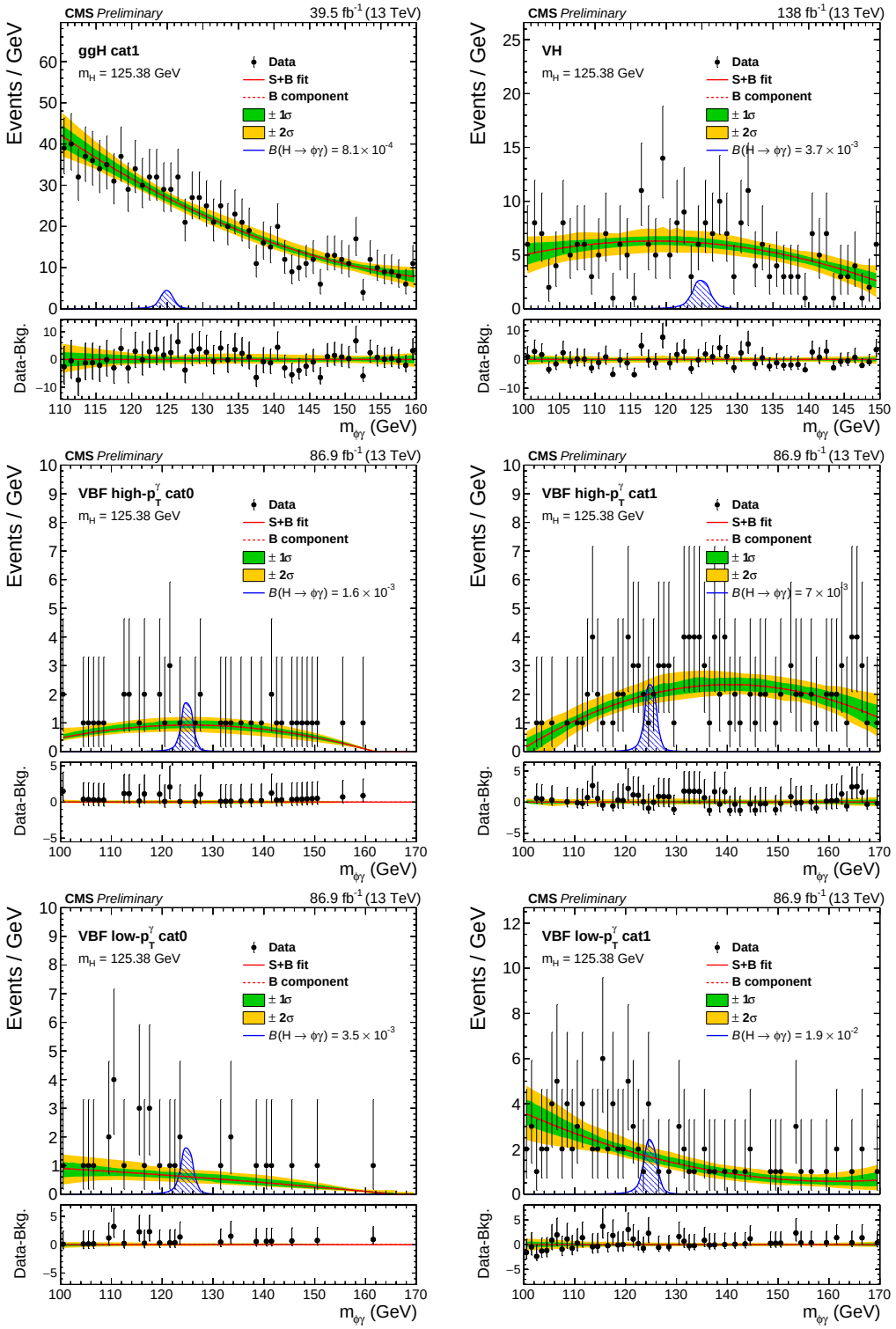

Figure 11.5: $\phi\gamma$ distribution in data and the background model with signal and background fit components and 1- and 2-σ fit uncertainty for the ggH BDTcat1 (top-left), VH (top-right), VBF high-p_T^γ BDTcat0 (middle-left), VBF high-p_T^γ BDTcat1 (middle-right), VBF low-p_T^γ BDTcat0 (bottom-left), VBF low-p_T^γ BDTcat1 (bottom-right) categories.

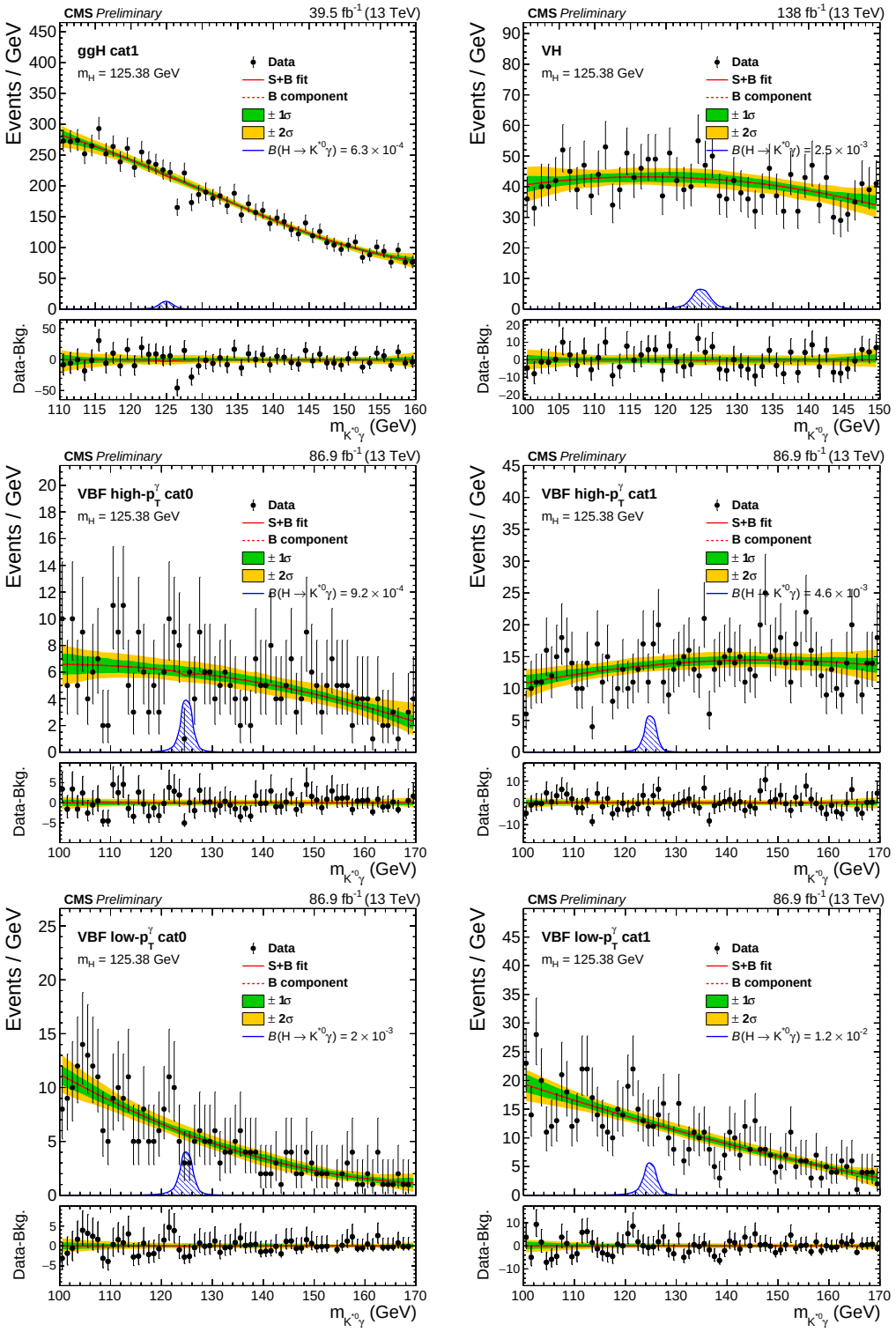

Figure 11.6: $m_{K^{*0}\gamma}$ distribution in data and the background model with signal and background fit components and 1- and 2-σ fit uncertainty for the ggH BDTcat1 (top-left), VH (top-right), VBF high-p_T^γ BDTcat0 (middle-left), VBF high-p_T^γ BDTcat1 (middle-right), VBF low-p_T^γ BDTcat0 (bottom-left), VBF low-p_T^γ BDTcat1 (bottom-right) categories.

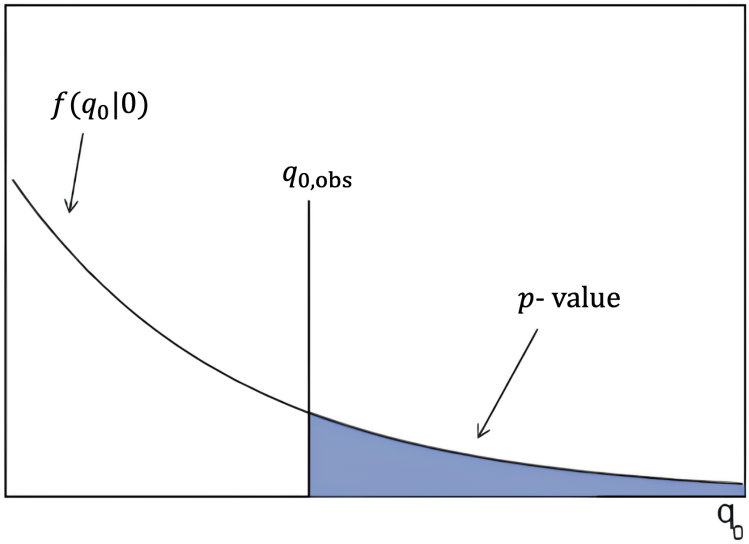

Figure 11.7: Representation of the p-value calculated as the area under the rightmost tail of a standard normal distribution.

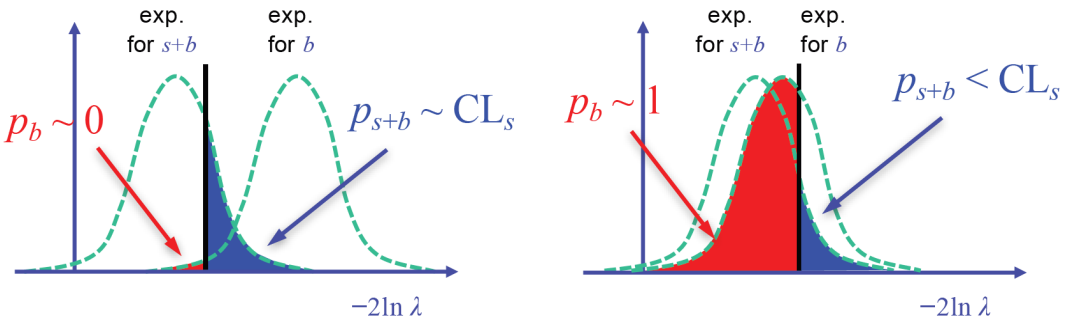

Figure 11.8: Illustration of the application of the CL_s method in cases of well separated distributions of the test statistic -2lnλ for the s + b and b hypotheses (left) and in case of largely overlapping distributions (right).

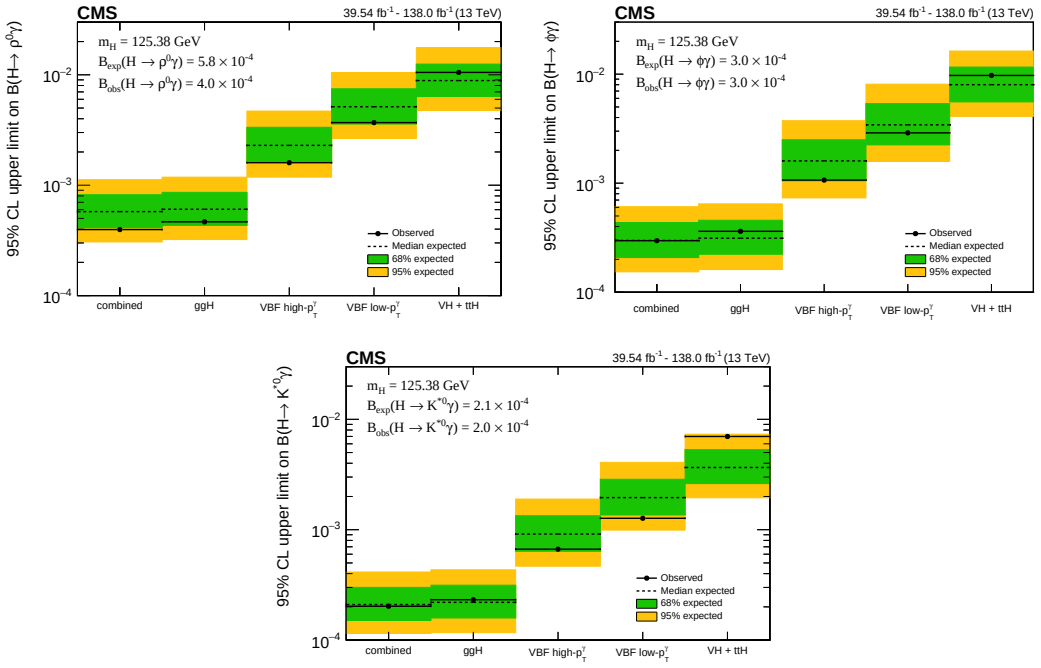

Figure 11.9: Expected and observed upper limits on $\mathcal{B}(H \to \phi\gamma)$ (top left), $\mathcal{B}(H \to \rho\gamma)$ (top right), and $\mathcal{B}(H \to K^{*0}\gamma)$ (bottom) split by analysis categories and combined. Green and yellow bands correspond to 1 and 2σ confidence intervals in the expected upper limits.

Conclusions 12

The Higgs boson discovery in 2012 has established the existence of a new elementary particle, which couples to the other particles of the SM in a non-universal way. The Higgs couplings to γ, Z, and W bosons, as well as fermions down to the second generation, have been experimentally observed and found consistent with the SM expectations. However, the SM does not adequately explain several observed phenomena, motivating the development of theories beyond the SM, many of which propose alterations to the Higgs sector. Consequently, a thorough examination of the Higgs boson becomes a crucial objective for particle physics experiments, including the exploration of rare and theoretically forbidden Higgs decays.

This thesis work focuses on the search for $H \to \rho\gamma$, $H \to \phi\gamma$ and $H \to K^{*0}\gamma$ processes with the aim of studying the Yukawa couplings to light quarks and investigating potential BSM effects that might enhance the branching ratios of these decays. This analysis is performed on a part of LHC Run-II data from proton-proton collisions at $\sqrt{s}$ = 13 TeV, collected by the CMS experiment at the LHC and corresponding to an integrated luminosity varying between 40 and 137 fb^{-1} depending on the detailed final state. Different Higgs boson production modes are targeted: gluon-gluon fusion, vector-boson fusion, and associated production with W and Z bosons. Depending on the production mode, different signal triggering and reconstruction techniques are adopted. The Higgs boson candidates are reconstructed by isolating events with a high-energy photon and a high-energy meson via its decay into charged tracks $\rho \to \pi^+\pi^-$, $\phi \to K^+K^-$ and $K^{*0} \to K^\pm\pi^\mp$. Following a multistep selection process designed to isolate signal-like events and reject the background, the number of signal events is determined by fitting the invariant mass spectrum of the two tracks and the photon. Upper limits at the 95% CL on the Higgs boson branching fractions into

$\rho\gamma$, $\phi\gamma$, and $K^{*0}\gamma$ are determined to be $3.74 \cdot 10^{-4}$, $2.97 \cdot 10^{-4}$, and $1.71 \cdot 10^{-4}$, respectively. These results constitute the most stringent experimental limits to date on the $\rho\gamma$ and $\phi\gamma$ decay channels.

In a related context, the ATLAS collaboration has published upper limits at the 95% CL for the branching fractions of the Higgs boson decays into $\phi\gamma$ and $\rho\gamma$ as $5.0 \cdot 10^{-4}$ and $10.4 \cdot 10^{-4}$, respectively, on an integrated luminosity of nearly 36 fb^{-1} [26]. This dataset size is comparable to the one utilized in this thesis for the gluon fusion category, whose contribution to the combined limit largely dominates with respect to the other categories. The analysis methodology of ATLAS closely mirrors that of this work, searching for high-energy pair of tracks and high-energy photon as a Higgs boson candidate. However, the approach taken in this thesis differs in some aspects: firstly, the targeting of different Higgs boson production mechanisms; secondly, a novel approach of selecting the charged tracks coming from the meson decay is employed, searching for them among the constituents of the most energetic jets of the event rather than looping on the entire combinatorics. Moreover, a multivariate analysis have been performed to enhance the signal and background discrimination and a cut on an isolation from neutral particles of the meson have been applied. The latter two points significantly enhanced the sensitivity of the analysis, yielding more stringent expected limits of factors of 1.7 for the $\rho\gamma$ channel and 1.4 for the $\phi\gamma$ channel with respect to the ATLAS results.

In a recent publication by ATLAS, an upper limit at the 95% CL on the Higgs boson branching fractions into $K^{*0}\gamma$ corresponding to 2.2×10^{-4} was determined [27], by performing a similar analysis to $H \to \rho\gamma$ and $H \to \phi\gamma$ in 2018, but on the full Run-II dataset. The ATLAS analysis having approximately triple the dataset size compared to that of this work, the statistical contribution to the sensitivity to $H \to K^{*0}\gamma$ decay channel is expected to correspond to a factor of about 1.7. However, the ATLAS expected limit closely matches those presented in this thesis, maintaining consistency with the trends observed in the other decay channels.

With the higher amount of data that will be acquired by the upcoming LHC Run-III, an even stricter upper limit could be provided, enhancing the sensitivity to the processes searched for by this thesis. By the end of its life, CMS will have collected around 100 times more statistics with respect to the 40 fb^{-1} used for the ggH analysis, thanks to the high instantaneous luminosity expected in the HL-LHC data taking period. Ignoring systematic uncertainties, this will lead to

an improvement on the expected branching ratio sensitivity of a factor about 10 better, allowing to explore the 10^{-5} region for $\mathcal{B}(H \to \rho/\phi/K^{*0}\gamma)$ and to confirm or exclude BSM theories.

Bibliography

[1] Aron J. Beekman et al. An introduction to spontaneous symmetry breaking. *SciPost Phys. Lect. Notes*, 2019. doi:10.21468/SciPostPhysLectNotes.11.

[2] J. Goldstone. Field Theories with Superconductor Solutions. *Nuovo Cim.*, 19, 1961. doi:10.1007/BF02812722.

[3] ATLAS. Observation of a new particle in the search for the standard model higgs boson with the atlas detector at the lhc. *Phys. Lett. B*, 716, 2012. doi:10.1016/j.physletb.2012.08.020.

[4] CMS. Observation of a new boson at a mass near 125 GeV with the CMS experiment at the LHC. *Phys. Lett. B*, 716, 2012. doi:10.1016/j.physletb.2012.08.021.

[5] ATLAS and CMS. Combined Measurement of the Higgs Boson mass in pp Collisions at $\sqrt{s} = 7$ and 8 TeV with the ATLAS and CMS Experiments. *Phys. Lett. B 114*, 2015. doi:10.1103/PhysRevLett.114.191803.

[6] CMS. A measurement of the Higgs boson mass in the diphoton decay channel. *Phys. Lett. B*, 805, 2020. doi:10.1016/j.physletb.2020.135425.

[7] D. de Florian et al. Handbook of LHC Higgs Cross Sections: 4. Deciphering the Nature of the Higgs Sector. 2016. doi:http://dx.doi.org/10.23731/CYRM-2017-002.

[8] CMS. Measurements of Higgs boson production cross sections and couplings in the diphoton decay channel at $\sqrt{s} = 13$ TeV. *JHEP*, 7, 2021. doi:10.1007/jhep07(2021)027.

[9] CMS. Measurements of production cross sections of the Higgs boson in the four-lepton final state in proton–proton collisions at $\sqrt{s} = 13$ TeV. *Eur. Phys. J. C*, 81, 2021. doi:10.1140/epjc/s10052-021-09200-x.

[10] CMS. Measurements of properties of the Higgs boson decaying to a W boson pair in pp collisions at $\sqrt{s} = 13$ TeV. *Phys. Lett. B*, 791, 2019. doi:10.1016/j.physletb.2018.12.073.

[11] ATLAS. Evidence for the Higgs Boson Decay to a Z Boson and a Photon at the LHC. *Phys. Lett. B*, 132, 2024. doi:10.1103/PhysRevLett.132.021803.

[12] ATLAS. Observation of Higgs boson production in association with a top quark pair at the LHC with the ATLAS detector. *Phys. Lett. B*, 784, 2018. doi:10.1016/j.physletb.2018.07.035.

[13] CMS. Observation of $t\bar{t}H$ production. *Phys. Lett. B*, 120, 2018. doi:10.1103/PhysRevLett.120.231801.

[14] ATLAS. Measurements of Higgs boson production cross-sections in the $H \to \tau^+\tau^-$ decay channel in pp collisions at $\sqrt{s} = 13$ TeV with the ATLAS detector. *JHEP*, 08, 2022. doi:10.1007/JHEP08(2022)175.

[15] CMS. Measurement of the inclusive and differential Higgs boson production cross sections in the decay mode to a pair of τ leptons in pp collisions at $\sqrt{s} =$ 13 TeV. *Phys. Lett. B*, 128, 2022. doi:10.1103/PhysRevLett.128.081805.

[16] ATLAS. Measurements of WH and ZH production in the $H \to b\bar{b}$ decay channel in pp collisions at 13 TeV with the ATLAS detector. *Eur. Phys. J. C*, 81, 2021. doi:10.1140/epjc/s10052-020-08677-2.

[17] CMS. Observation of the Higgs boson decay to bottom quarks. *Phys. Lett. B*, 121, 2018. doi:10.1103/PhysRevLett.121.121801.

[18] ATLAS. Direct constraint on the Higgs-charm coupling from a search for Higgs boson decays into charm quarks with the ATLAS detector. *Eur. Phys. J. C*, 82, 2022. doi:10.1140/epjc/s10052-022-10588-3.

[19] CMS. Search for Higgs boson decay to a charm quark-antiquark pair in proton-proton collisions at $\sqrt{s} = 13$ TeV, *accepted by Phys. Lett. B*. *Phys. Lett. B*, 137, 2022. doi:10.1103/PhysRevLett.131.061801.

[20] CMS. Evidence for Higgs boson decay to a pair of muons. *JHEP*, 01, 2021. doi:10.1007/JHEP01(2021)148.

[21] ATLAS. A search for the dimuon decay of the Standard Model Higgs boson with the ATLAS detector. *Phys. Lett. B*, 812, 2021. doi:10.1016/j.physletb.2020.135980.

[22] ATLAS. Search for the Higgs boson decays $H \to ee$ and $H \to \mu\mu$ in pp collisions at $\sqrt{s}$ = 13 TeV with the ATLAS detector. *Phys. Lett. B*, 801, 2020. doi:10.1016/j.physletb.2019.135148.

[23] CMS. Search for the higgs boson decay to a pair of electrons in proton-proton collisions at $\sqrt{s}$ = 13 tev. *Phys. Lett. B*, 846, 2023. doi:10.1016/j.physletb.2023.137783.

[24] CMS. Observation of WWγ production and search for Hγ production in proton-proton collisions at $\sqrt{s}$ = 13 TeV. Technical report, 2023. Submitted to *Phys. Lett*. URL: https://cds.cern.ch/record/2875047.

[25] CMS. Search for decays of the 125 GeV Higgs boson into a Z boson and a ρ or ϕ meson. *JHEP*, 11, 2020. doi:10.1007/JHEP11(2020)039.

[26] ATLAS. Erratum to: Search for exclusive Higgs and Z boson decays to $\phi\gamma$ and $\rho\gamma$ with the ATLAS detector. *JHEP*, 2023. doi:doi.org/10.1007/JHEP12(2023)158.

[27] ATLAS. Search for exclusive Higgs and Z boson decays to $\omega\gamma$ and Higgs boson decays to $K^*\gamma$ with the ATLAS detector. *Phys. Lett. B*, 847, 2023. doi:10.1016/j.physletb.2023.138292.

[28] CMS. Search for Higgs boson decays into Z and J/Ψ and for Higgs and Z boson decays into J/Ψ or Υ pairs in pp collisions at 13 TeV. *Phys. Lett. B*, 842, 2023. doi:10.1016/j.physletb.2022.137534.

[29] CMS. Search for the rare decays of the Z and Higgs bosons to a J/Ψ or Ψ' meson and a photon in proton-proton collisions at $\sqrt{s}$ = 13 TeV. *Eur. Phys. J. C*, 79, 2019. doi:10.1140/epjc/s10052-019-6562-5.

[30] ATLAS. Searches for exclusive Higgs and Z boson decays into $J/\psi\gamma$, $\psi(2S)\gamma$, and $\Upsilon(nS)\gamma$ at $\sqrt{s}$ = 13 TeV with the ATLAS detector. *Phys. Lett. B*, 786, 2018. doi:10.1016/j.physletb.2018.09.024.

[31] M. König and M. Neubert. Exclusive Radiative Higgs Decays as Probes of Light-Quark Yukawa Couplings. *JHEP*, 08, 2015. doi:10.1007/JHEP08(2015)012.

[32] Alexander L. Kagan et al. Exclusive window onto higgs yukawa couplings. *Phys. Lett. B*, 114(10), 2015. doi:10.1103/physrevlett.114.101802.

[33] Gilad Perez et al. Prospects for measuring the Higgs boson coupling to light quarks. *Phys. Rev. D*, 93, 2016. doi:10.1103/PhysRevD.93.013001.

[34] G. Peter Lepage and Stanley J. Brodsky. Exclusive processes in perturbative quantum chromodynamics. *Phys. Rev. D*, 22, 1980. doi:10.1103/PhysRevD.22.2157.

[35] A. V. Efremov and A. V. Radyushkin. Factorization and Asymptotical Behavior of Pion Form-Factor in QCD. *Phys. Lett. B*, 94, 1980. doi:10.1016/0370-2693(80)90869-2.

[36] V. L. Chernyak and A. R. Zhitnitsky. Asymptotic Behavior of Exclusive Processes in QCD. *Phys. Rept.*, 112, 1984. doi:10.1016/0370-1573(84)90126-1.

[37] J. I. Aranda et al. Revisiting the rare $H \to q_i q_j$ decays in the Standard Model. *Journal of Physics G: Nucl. and Part. Phys.*, 47(12), 2020. doi:10.1088/1361-6471/abb44d.

[38] D. d'Enterria and Van Dung L. Rare and exclusive few-body decays of the Higgs, Z, W bosons, and the top quark, 2023. doi:10.48550/arXiv.2312.11211.

[39] G. F. Giudice and O. Lebedev. Higgs-dependent Yukawa couplings, 2008. doi:10.1016/j.physletb.2008.05.062.

[40] D'Ambrosio et al. Minimal flavour violation: an effective field theory approach. *Nucl. Phys. B*, 645(1–2), 2002. doi:10.1016/s0550-3213(02)00836-2.

[41] Froggatt C. D. and Nielsen H. B. Hierarchy of Quark Masses, Cabibbo Angles and CP Violation. *Nucl. Phys. B*, 147, 1979. doi:10.1016/0550-3213(79)90316-X.

[42] L. Randall and R. Sundrum. Large mass hierarchy from a small extra dimension. *Phys. Lett. B*, 83, 1999. doi:10.1103/physrevlett.83.3370.

[43] Michael J. D. et al. Anatomy of a composite Higgs model. *Nucl. Phys.*, 254, 1985. doi:10.1016/0550-3213(85)90221-4.

[44] G. Acquistapace et al. Cms, the magnet project: Technical design report. 1997. doi:10.17181/CERN.6ZU0.V4T9.

[45] K.A. Olive. Review of particle physics. *Chinese Phys. C*, 38(9), 2014. doi:10.1088/1674-1137/38/9/090001.

[46] Christian W. Fabjan. *Calorimetry in High-Energy Physics*. 1985. doi:10.1007/978-1-4684-5018-7_5.

[47] CMS. The CMS hadron calorimeter project: Technical Design Report. 1997. URL: https://cds.cern.ch/record/357153?ln=it.

[48] CMS. The CMS muon project. 1997. URL: https://cds.cern.ch/record/343814?ln=it.

[49] CMS. Commissioning of the Particle-flow Event Reconstruction with the first LHC collisions recorded in the CMS detector. 2010. URL: https://cds.cern.ch/record/1247373.

[50] P. Azzurri. Track reconstruction performance in cms. *Nucl. Phys. B*, 197(1), 2009. doi:10.1016/j.nuclphysbps.2009.10.084.

[51] P. Billoir and S. Qian. Simultaneous pattern recognition and track fitting by the Kalman filtering method. *Nucl. Instrum. Meth. A*, 294, 1990. doi:10.1016/0168-9002(90)91835-Y.

[52] P. Nason. A new method for combining NLO QCD with shower Monte Carlo algorithms. *JHEP*, 11, 2004. doi:10.1088/1126-6708/2004/11/040.

[53] S. Frixione et al. Matching NLO QCD computations with Parton Shower simulations: the POWHEG method. *JHEP*, 0711, 2007. doi:10.1088/1126-6708/2007/11/070.

[54] S. Alioli et al. NLO Higgs boson production via gluon fusion matched with shower in POWHEG. *JHEP*, 04, 2009. doi:10.1088/1126-6708/2009/04/002.

[55] S. Alioli et al. A general framework for implementing NLO calculations in shower Monte Carlo programs: the POWHEG BOX. *JHEP*, 06, 2010. doi:10.1007/JHEP06(2010)043.

[56] P. Nason and C. Oleari. NLO Higgs boson production via vector-boson fusion matched with shower in POWHEG. *JHEP*, 02, 2010. doi:10.1007/JHEP02(2010)037.

[57] G. Luisoni et al. $HW^{\pm}/HZ + 0$ and 1 jet at NLO with the POWHEG BOX interfaced to GoSam and their merging within MiNLO. *JHEP*, 10, 2013. doi:10.1007/JHEP10(2013)083.

[58] J. Alwall et al. The automated computation of tree-level and next-to-leading order differential cross sections, and their matching to parton shower simulations. *JHEP*, 07, 2014. arXiv:1405.0301, doi:10.1007/JHEP07(2014)079.

[59] R. D. Ball et al. Parton distributions from high-precision collider data. *Eur. Phys. J. C*, 77, 2017. doi:10.1140/epjc/s10052-017-5199-5.

[60] T. Sjöstrand et al. An introduction to PYTHIA 8.2. *Comput. Phys. Commun.*, 191, 2015. doi:10.1016/j.cpc.2015.01.024.

[61] CMS. Extraction and validation of a new set of CMS PYTHIA8 tunes from underlying-event measurements. *Eur. Phys. J. C*, 80, 2020. doi:10.1140/epjc/s10052-019-7499-4.

[62] S. Agostinelli et al. GEANT4–a simulation toolkit. *Nucl. Instrum. Meth. A*, 506, 2003. doi:10.1016/S0168-9002(03)01368-8.

[63] CMS. Technical proposal for the Phase-II upgrade of the Compact Muon Solenoid. CMS Technical Proposal CERN-LHCC-2015-010, CMS-TDR-15-02, 2015. URL: http://cds.cern.ch/record/2020886.

[64] Vardan Khachatryan et al. Performance of electron reconstruction and selection with the CMS detector in proton-proton collisions at $\sqrt{s} = 8$ TeV. *JINST*, 10:P06005, 2015. arXiv:1502.02701, doi:10.1088/1748-0221/10/06/P06005.

[65] CMS. Electron and photon reconstruction and identification with the CMS experiment at the CERN LHC. *JINST*, 16, 2021. doi:10.1088/1748-0221/16/05/P05014.

[66] CMS. Description and performance of track and primary-vertex reconstruction with the CMS tracker. *JINST*, 9, 2014. doi:10.1088/1748-0221/9/10/P10009.

[67] Yann Coadou. *Boosted Decision Trees*, page 9–58. WORLD SCIENTIFIC, February 2022. URL: http://dx.doi.org/10.1142/9789811234033_0002, doi:10.1142/9789811234033_0002.

[68] A. Hoecker et al. TMVA - Toolkit for Multivariate Data Analysis, 2007. doi:10.48550/ARXIV.PHYSICS/0703039.

[69] T. Chen and C. Guestrin. Xgboost: A scalable tree boosting system. 2016. doi:10.1145/2939672.2939785.

[70] F. James. MINUIT Function Minimization and Error Analysis: Reference Manual Version 94.1. 1994. URL: https://cds.cern.ch/record/2296388/.

[71] R. L. Workman et al. Review of Particle Physics. *Prog. Theor. Exp. Phys.*, 2022. doi:10.1093/ptep/ptac097.

[72] J. Butterworth et al. PDF4LHC recommendations for LHC Run II. *Journal of Physics G: Nucl. and Part. Phys.*, 43(2), 2016. doi:10.1088/0954-3899/43/2/023001.

[73] CMS. Precision luminosity measurement in proton-proton collisions at $\sqrt{s}$ = 13 TeV in 2015 and 2016 at CMS. *Eur. Phys. J. C*, 81, 2021. doi:10.1140/epjc/s10052-021-09538-2.

[74] CMS. CMS luminosity measurement for the 2016 data-taking period at $\sqrt{s}$ = 13 TeV. *Technical report*, 2017. URL: https://cds.cern.ch/record/2257069?ln=it.

[75] CMS luminosity measurement for the 2017 data-taking period at $\sqrt{s}$ = 13 TeV. *Technical report*, 2018. URL: https://cds.cern.ch/record/2621960?ln=it.

[76] CMS. CMS luminosity measurement for the 2018 data-taking period at $\sqrt{s}$ = 13 TeV. *Technical report*, 2019. URL: https://cds.cern.ch/record/2676164?ln=it.

[77] CMS. Jet algorithms performance in 13 TeV data. 2017. doi:https://cds.cern.ch/record/2256875?ln=it.

[78] A M Sirunyan et al. Performance of the CMS muon detector and muon reconstruction with proton-proton collisions at $\sqrt{s}$ = 13 TeV. *JINST*, 13:P06015, 2018. arXiv:1804.04528, doi:10.1088/1748-0221/13/06/P06015.

[79] CMS. Measurement of Tracking Efficiency. 2010. URL: https://cds.cern.ch/record/1279139/.

[80] T. Rahlf. *Statistical Inference*. Springer Berlin Heidelberg, 2021. doi:10.1007/978-3-642-40458-0_16-2.

[81] R. D. Cousins. *Generalization of chisquare goodness-of fit test for binned data using saturated models , with application to histograms.* 2013. URL: https://www.physics.ucla.edu/~cousins/stats/cousins_saturated.pdf.

[82] A L Read. Modified frequentist analysis of search results (the CL_s method). (CERN-OPEN-2000-205), 2000. doi:10.5170/CERN-2000-005.81.